Theoretical Modeling of Polymeric and Biological Nanostructured Materials

Hadi Rahmaninejad

Dissertation submitted to the Faculty of the

Virginia Polytechnic Institute and State University

in partial fulfillment of the requirements for the degree of

Doctor of Philosophy

in

Physics

Rana Ashkar, Chair

Shengfeng Cheng

Jean Heremans

Sanket Deshmukh

December 7, 2022

Blacksburg, Virginia

Keywords: Neutron and X-ray scattering, dynamical theory, periodic nanostructures, nano-fluidics, polymer brushes, polymer coatings, supported lipid membranes

Theoretical Modeling of Polymeric and Biological Nanostructured Materials

Hadi Rahmaninejad

(ABSTRACT)

Polymer coatings on periodic nanostructures have facilitated advanced applications in various fields. The performance of these structures is intimately linked to their nanoscale characteristics. Smart polymer coatings responsive to environmental stimuli such as temperature, pH level, and ionic strength have found important uses in these applications. Therefore, to optimize their performance and improve their design, precise characterization techniques are essential for understanding the nanoscale properties of polymer coating, especially in response to stimuli and interactions with the surrounding medium. Due to their layered compositions, applying non-destructive measurement methods by X-ray/neutron scattering is optimal. These approaches offer unique insights into the structure, dynamics, and kinetics of polymeric coatings and interfaces. The caveat is that scattering methods require non-trivial data modeling, particularly in the case of periodic structures, which result in strong correlations between scattered beams. The dynamical theory (DT) model offers an exact model for interpreting off-specular signals from periodically structured surfaces and has been validated on substrates measured by neutron scattering. In this dissertation, we improved the model using a computational optimization approach that simultaneously fits specular and off-specular scattering signals and efficiently retrieves the three-dimensional sample profile with high precision. In addition, we extended this to the case of X-ray scattering. We applied this approach to characterize polymer brushes for nanofluidic applications and protein binding to modulated lipid membranes. This approach opens new possibilities in developing soft matter nanostructured substrates with desired properties for various applications.

Theoretical Modeling of Polymeric and Biological Nanostructured Materials

Hadi Rahmaninejad

(GENERAL AUDIENCE ABSTRACT)

Polymer coatings on nanopatterned surfaces have recently facilitated advanced applications in various fields, particularly biotechnology. For example, multichannel surfaces coated with polymer can serve as nanofluidic devices for precise control of fluid flow in drug screening and detection of specific biomolecules. Moreover, polymer-coated nanopatterned surfaces, which possess similar properties to the extracellular matrix, provide excellent substrates for biological studies. The performance of these systems is closely tied to their nanoscale features, such as the thickness and conformation of the polymer layers. Therefore, high-resolution non-invasive nanoscale characterization techniques are essential for investigating these coatings to optimize their performance and enhance their design. X-ray/neutron scattering offers a non-destructive measurement method with unique capabilities in the nanoscale characterization of polymer coatings. However, scattering methods require non-trivial data modeling, particularly in the case of layered coatings on patterned surfaces. To tackle this challenge, we improved a dynamical theory (DT) model that allows for precise modeling of neutron and X-ray scattering signals from such systems. Using a computational optimization approach, the model enables efficient retrieval of the three-dimensional sample profile with high accuracy. We applied this approach to characterize polymer brushes for nanofluidic applications and protein binding to modulated lipid membranes. This methodology opens up new avenues for developing customizable, nanostructured substrates made from soft materials that possess tailored properties for a wide range of uses.

Dedication

To my beloved wife, Ayda

and my dear family

Contents

1 Introduction and overview **1**

2 Scattering techniques **7**

2.1 Elastic scattering techniques 7

2.2 Inelastic and quasi-elastic scattering 17

2.3 Coherent and incoherent neutron scattering 19

3 Dynamical Theory analysis of reflection from periodic structures **21**

3.1 Neutron interaction with matter 22

3.1.1 X-ray interaction with matter 23

3.1.2 Reflection at an interface 26

3.1.3 Reflection from a uniform thin film 27

3.1.4 Interfacial roughness 29

3.1.5 Reflection from laterally structured thin films, Dynamical Theory . . 31

4 Characterization of periodic nanostructures with X-ray scattering **36**

4.1 Method 37

4.1.1 Experiment 40

4.1.2 Data Analysis 41

4.2 Results 43

4.3 Conclusion 44

5 Polymer brush conformations in nanofluidic channels 46

5.1 Overview 46

5.2 Materials and Methods 49

5.2.1 Sample preparation 49

5.2.2 Neutron reflectometry measurements. 49

5.2.3 Data Analysis 51

5.2.4 Off-specular data analysis. 53

5.2.5 Data reduction for Off-specular signals 53

5.2.6 Optimization protocol. 54

5.3 Results and discussion 55

5.3.1 In-depth channel geometry. 55

5.3.2 Brush Conformation. 58

5.3.3 Effect of pH on gate opening. 60

5.3.4 Effect of ionic strength on gate opening. 64

6 Effect of membrane curvature on protein binding 69

6.1 Overview 69

6.2 Methods 71

6.2.1 Sample preparation 71

6.2.2 Neutron reflectometry experiment 72

6.2.3 Data analysis 73

6.3 Results 76

6.3.1 In-depth characterization 76

6.3.2 Off-specular analysis improvement 77

6.3.3 Lateral structure 79

7 Conclusions and outlook **81**

Bibliography **84**

Chapter 1

Introduction and overview

Self-assembly, responsiveness, and tailorability are attractive features of soft materials that open new possibilities for designing smart devices with diverse applications [1, 2, 3, 4, 5]. Constructed from polymers, foams, gels, colloids, or biological entities with energies usually in the thermal range (1 kT-36 kT), soft materials are very deformable with thermal fluctuations, and external forces [6]. This feature allows novel control of the components' size, ordering, and orientation and offers the formation of systems with desired properties. The key idea is to program individual blocks and their interactions to design more complex structures with functional properties, usually inspired by similar systems in nature. For instance, smart soft-matter nanotubes made of organic molecular building blocks offer a controlled and tunable channel size and diameter, which can accommodate substrates ranging from molecules to viruses for nanobiotechnological uses [7]. Another example is in DNA nanotechnology, where self-assembly-based approaches allow the design of complex geometries incorporating inorganic materials such as metals and semiconductors to fabricate nanoelectronic and nanooptic devices [8]. Furthermore, inspired by nature, novel preparation routes (biomimetic approaches) can be developed for designing complicated materials with applications such as biocompatible batteries, tissue engineering scaffolds, and controllable nanofluidic channels. In addition, many types of soft materials, such as hydrogels, are highly responsive to external stimuli, which offers potential applications in growing fields of soft robotics, tissue engineering, nanofluidic, biosensing, biomimetic machines, soft bioelectron-

ics, and on-demand drug delivery.

Among various soft-matter-based nanostructured materials, polymer coatings onto surfaces have essential applications in numerous fields, ranging from biological and biomedical purposes for antifouling, bio-separation, and tissue engineering, to novel interfaces in optics, electronics, and fuel cells with exceptional mechanical, optical, or thermal properties [9, 10, 11, 12, 13]. The properties of the polymer coating are critical factors in these applications, particularly its interactions with the surrounding medium and in response to stimuli. Polymer coatings can be obtained by simple adsorption of polymer chains onto surfaces and interfaces or by controlled chemical functionalization. The latter approach has attracted significant attention over the past few decades, leading to novel methods for grafting polymer chains to or from surfaces and interfaces [14]. Recently, polymer coating on nano-patterned surfaces such as gratings has had significant academic and industrial implications in various fields such as optics [15], electronics[16], and biotechnology[17]. In addition, they have also been playing a central role in biological studies by providing frameworks and environments analogous to the cellular milieus.

Despite recent progress in soft matter technology, we are still in the infant stages of designing complex soft nanostructures with specific properties found in natural structures. With the constantly increasing demand for such materials' performance and complex functionalities, understanding their properties and interactions with the dispersing medium is requisite for material design and function. In particular, understanding the underlying self-assembly process during their fabrication and ensuring their desired performance is vital in the further development of soft nanoscale structures. Precise and effective characterization of critical feature dimensions in a wide range of the length scale is indispensable for unraveling the complex physical and chemical phenomena in these processes. This inevitably necessitates using characterization methods to adequately detect soft matter nanostructures and resolve

their structural, dynamic, and kinetic properties over the relevant length and time scales.

On the nanoscopic scale, the so-called direct detection techniques, comprising mainly microscopic methods, such as scanning electron microscopy (SEM) and atomic force microscopy (AFM), have played a central role in material characterization [18, 19, 20, 21, 22]. They usually provide adequate top and cross-sectional views of nanopatterns on substrates. However, providing in-depth information such as layered structures requires a cross-sectional view of the sample, which can be obtained by cutting through the sample's surface. In addition, owing to the localized nature of the microscopy techniques, they mostly provide limited sample statistics. Moreover, for soft-matter-based nanostructures, which are usually sensitive to external stimuli, there usually is the risk of altering the structure of soft nano-objects and damaging the sample.

On the other hand, indirect measurements by scattering techniques, mainly with neutron/X-ray, such as crystallography, small-angle scattering, diffraction, and reflectometry, offer non-destructive tools for the metrology of soft nanoscale structures with high statistical sampling. The relatively high penetration depth and submicron wavelength range (0.1 Å to 100 Å for X-rays and 1 Å-10 Å for neutrons) provide unique insights that complement conventional characterization methods for high-resolution studies of layered soft-matter-based nanostructures with novel molecular architectures. This is aided by the inherent capacity of neutrons and X-rays to detect structures and dynamics on length and time scales that are relevant to the performance of polymeric materials. Neutron scattering has a desirable property for the detection of soft materials, mainly polymeric and biological structures, and that has to do with its isotope sensitivity. In particular, the sensitivity to hydrogen (H), the most abundant element in these systems, is considerably large, enabling studies of different components of the studied structure. Neutrons are charge neutral; thus, they do not interact with the electronic clouds of atoms and only interact with atomic nuclei. Thus, neutron scattering

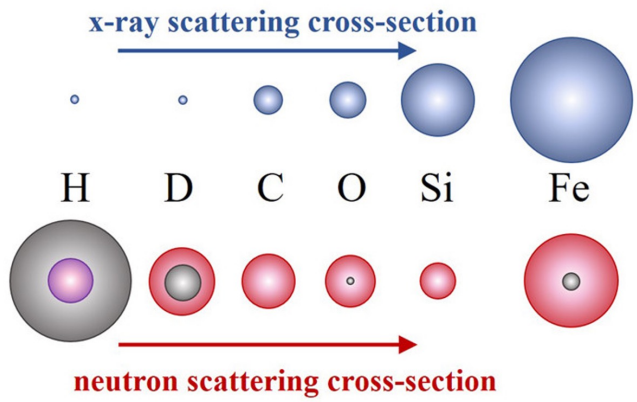

Figure 1.1: X-ray vs. neutron scattering cross-sections for some of the most abundant elements. While X-ray scattering cross-section follows a monotonic increase with charge number, neutron scattering cross-section is not proportional to the charge number but depends on neutron interactions with atomic nuclei. Red and gray spheres represent select atoms' coherent and incoherent scattering cross-sections. For hydrogen, the coherent cross-section is represented by purple to indicate its negative scattering length. The figure is reproduced with permission from Ashkar, J. Appl. Phys., 2020, 127, 151101 [23]

cross-section is not proportional to the atomic number but depends on the nuclear structure (see Figure 1.1.) This phenomenon results in applicable properties for material characterization. An immediate consequence is that neutrons have an even higher penetration length than X-rays. Moreover, they have considerably lower degrading effects on soft materials such as polymer and biological membranes due to their low energy. A more important consequence is the large neutron scattering cross-section for lighter elements, mainly hydrogen ($\sigma_H = 80.27$ barns [24]) and carbon, while for X-rays, the scattering signal is more dominated by heavier elements and leaves light atoms almost invisible. This property of neutron scattering makes it well-suited for studies of the hydrogen-rich constituents, e.g., biological structures and polymers, within samples with compositional complexity [25]. Another consequence of neutron interactions with atomic nuclei is its isotope sensitivity, meaning that neutron scattering cross-sections from different elemental isotopes can be noticeably different [26]. A well-known example is a difference in neutron scattering cross-sections between

protium (H) and deuterium (D). The neutron scattering lengths, b, for H and D, are respectively given by $b_H = -3.74\,\text{fm}$ and $b_D = 3.99\,\text{fm}$. Given the abundance of H in biological and polymeric materials and the relatively convenient procedure of substituting H for D, neutron isotope sensitivity offers a unique method for probing molecular arrangements and submolecular structures [27, 28, 29]. Using an approach referred to as contrast variation, isotope substitution schemes can be designed to modify specific moieties' scattering potential, thereby tuning how strongly or weakly "visible" they are to neutrons. Notably, due to the sensitivity of X-rays and neutrons to different elements, they are frequently used as complementary techniques for adequately characterizing polymer samples, significantly improving our understanding of soft-matter-based nanostructures.

Scattering methods are grounded in tracking the change in the energy and momentum of the beam shining through the sample and predicting various features of its structure and dynamics. In physical terminology, scattering techniques provide information in the reciprocal space. They require decoding the scattered pattern to reconstruct the sample profile in real space, which is challenging. Due to the intrinsic interaction between the beam and the matter, quantum mechanical modeling is usually needed. Furthermore, scattering data modeling is more difficult when applied to regularly patterned profiles in periodic nanostructures, such as gratings, due to the high correlation between reflected and transmitted beams. Among different theoretical models, the dynamical theory (DT) exhibits high potential for predicting scattering phenomena from periodic patterns by considering the correlation between scattered beams and providing an exact solution [30]. This model has been validated on neutron scattering measurements of periodic structures for studies with applications such as tissue engineering for cell alignment and release [31].

In this dissertation, we will develop a computational framework based on DT model. We will advance it by including an optimization protocol using the covariance matrix adaptation

evolution strategy (CMA-es)[32]. We will show how this approach yields high efficiency and precision in predicting complicated profiles by adopting a Parratt thin-slicing formalism. Mainly, we will apply it to study soft-matter-based nanofluidic channels with controllable gating properties and membrane curvature effect on protein binding. We will also extend the theoretical bases of DT for the case of X-ray scattering by applying it to grazing incident small angle X-ray scattering data to characterize polymer coated grating structures.

The layout of the thesis is as follows. Chapter 1 presents an overview of the dissertation, its importance, and its application. In chapter 2 we will review various scattering techniques and their applications, with an emphasis on neutron scattering. We will highlight the impact of neutron scattering and spectroscopy methods in the characterization of polymer-based coatings, including thin films, polymer interfaces, polymer brushes, and particle coatings. In chapter 3 we will focus on the theoretical basis of reflectometry, particularly from periodic structures. We will discuss the dynamical theory model in detail and how it can be extended for the case of X-rays. We will elaborate on the modeling framework that we developed based on DT model for layered soft-matter coatings on periodic scaffolds. Chapter 4 applies the DT model and our computational framework to characterizing periodic nanostructures with X-ray. In chapter 5, we will focus on the characterization of polymer brush conformation in nanofluidic channels with similar methods. Finally, in chapter 6, our developed model is used for studying the effect of membrane curvature on protein binding using a topographically tunable scaffold.

Chapter 2

Scattering techniques

This chapter briefly reviews various scattering techniques and critical applications in characterizing soft-matter-based nanostructures, particularly for polymeric coatings. While the chapter primarily focuses on neutron scattering, most techniques have been equivalently applied to X-ray scattering. This is followed by select examples emphasizing their effective utilization in revealing the structure, dynamics, and kinetics of polymer coatings and polymeric interfaces. Mainly, some key examples of the synergic use of X-rays and neutron scattering will be pointed out. While the studies presented in this dissertation mainly focus on elastic scattering techniques, a brief discussion of inelastic and quasi-elastic scattering techniques is meant to provide a full picture of scattering capabilities in the characterization of soft materials. This chapter closely follows content from Chapter 19, "Neutron scattering studies of nanoscale polymer-based coatings", Hadi Rahmaninejad and Rana Ashkar, accepted for publication in the book titled "Polymer Based Nanoscale Materials For Surface Coating", edited by Sabu Thomas and Susan George (Elsevier).

2.1 Elastic scattering techniques

When X-ray or neutron beams scatter from materials, their wavevector generally changes in direction and magnitude. However, in the special case of elastic scattering, the beam's energy is conserved, i.e., the beam's energy before and after scattering remains unchanged.

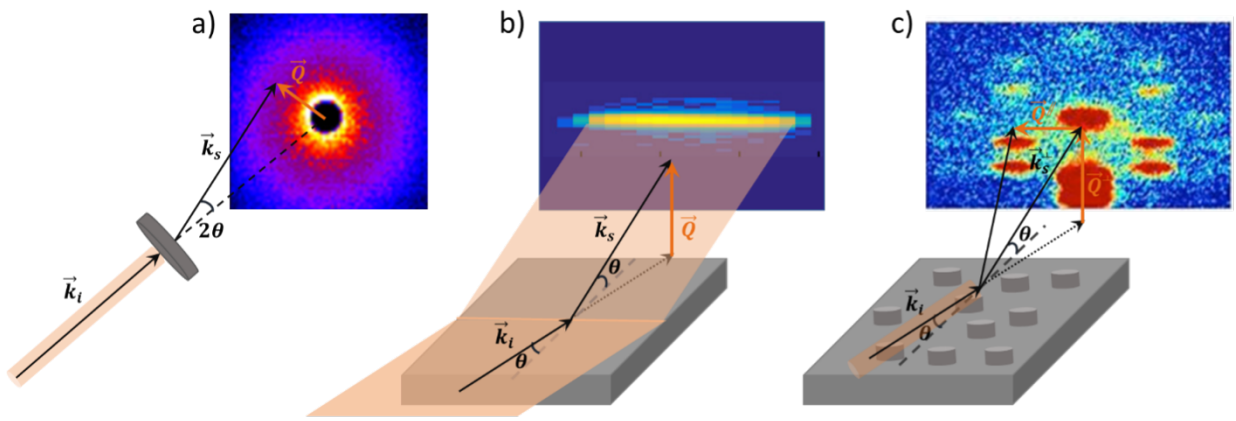

Figure 2.1: Schematic illustration of the scattering geometry for a) Small-angle neutron scattering (SANS), b) reflectometry and c) grazing-incidence SANS (GISANS). The figure shows the incident and scattered wavevectors $\vec{k_i}$ and $\vec{k_s}$, respectively, along with the wavevector transfer $\vec{Q} = \vec{k_s} - \vec{k_i}$ in each scenario. This figure is reproduced with permission from Rahmaninejad and Ashkar, chapter 19, "Neutron scattering studies of nanoscale polymer-based coatings", accepted for publication (Elsevier). Panel c is adapted with permission from Wolff et al., Euro. Phys. J. E, 2005, 16, 141-145 [38].

Given the energy dependence on the momentum, this implies that in elastic scattering, the magnitude of the momentum remains constant; i.e., $|\vec{k_s}| = |\vec{k_i}| = |\vec{k_0}|$ where $\vec{k_s}$ and $\vec{k_i}$ are the scattered and incident beam wavevectors and $k_0 = \frac{2\pi}{\lambda}$ with λ being the wavelength. Under these conditions, the momentum transfer, $\vec{Q} = \vec{k_s} - \vec{k_i}$, has a well-defined magnitude given by $Q = 2k_0 \sin\theta$ where 2θ is the angle between the incident and scattered beam, as shown in Figure 2.1 . On the other hand, when the beam exchanges energy with the sample during scattering events, the energy of the scattered beam is inevitably different from that of the incident beam – a phenomenon referred to as inelastic scattering. Elastic scattering is utilized for obtaining structural properties of materials, whereas inelastic scattering reveals information about sample dynamics. In this chapter, we will discuss two primary elastic scattering methods utilized in structural studies, such as for polymer coatings and thin films, namely small-angle X-ray/neutron scattering (SAXS/SANS) and reflectometry [33, 34, 35, 36, 37].

Small-angle Neutron/X-ray scattering (SANS/SAXS).

Small-angle scattering is a widely applied technique for structural studies of soft-matter systems, including biological structures and polymer coatings. Small-angle scattering techniques are based on a pin-hole geometry where the beam incident on a sample scatters forward on a 2D position sensitive detector (Figure 2.1a). To resolve the small scattering angles typical of these measurements, instruments are built with very long sample-to-detector distances (on the order of several meters). For instance, a typical Q-range accessed by SANS is $\sim (0.02 - 0.5)$ nm^{-1} corresponding to spatial distances of $\sim$ (1–300) nm. Accessing this extended Q range often requires variations in the two key parameters defining Q, i.e., the accessible range of scattering angles and the neutron wavelength. The former can be done by changing the sample-to-detector distance (i.e., by changing the angular acceptance or the solid angle intercepted by the detector). On the other hand, variations in the neutron wavelength can be inherent to the neutron spectrum (e.g., pulsed sources) or can be obtained by using neutron velocity selectors. Scattering signals in SANS experiments are detected as 2D intensity maps. For isotropic scattering, i.e., scattering from isotropic samples, the detected intensity maps are characterized by circular symmetry (around the beam stop). In this case, the 2D signals are usually circularly averaged and plotted as 1-dimensional I vs. Q plots, allowing subsequent analysis of the data using adequate models. However, in the case of structural directionality, e.g., structural alignment along a given direction, the detected signals become asymmetric and analysis of the angular dependence of I(Q) becomes necessary to assess the degree of alignment. In either case, structural SANS models can be used to fit the data. These models are developed using form factor, F(Q), calculations based on the structure's shape and size [39]. Form factor models are adequately applicable to dilute samples where structural correlations are absent or undetectable. However, for samples characterized by structural correlations, form factor models should be convoluted with the

structure factor, S(Q), for appropriate data fitting. In other words, $I(Q) = F(Q) \times S(Q)$, where S(Q)=1 in the absence of correlations.

In SANS experiments, selective deuteration is commonly utilized to highlight a specific sample feature or to suppress scattering from other structures within the sample. An exciting example is studying polymer-coated nanoparticle suspensions in which contrast matching the solvent and particle core results in selective scattering from the polymer coating, enabling reliable characterization of the coating structure. Indeed, this approach was effectively used to investigate the influence of pH and ionic strength on coatings of polythymidylic acid (dT_{35}) adsorbed and grafted to latex nanoparticles [40]. In this study, the layer thickness was determined by varying the solvent SLD using mixtures of D_2O and H_2O with different D_2O: H_2O ratios. The SANS measurements showed that the thickness of the adsorbed layers did not depend on the pH and ionic strength of the solvent, contrary to the highly grafted dT_{35} chains, which exhibited a more extended structure in a basic pH and moderate ionic strength. However, even when contrast matching is not possible, innate SLD differences between the coating, particle core, and suspending medium can be sufficient for determining the coating structure using adequate models. An example of this approach was used in early SANS studies investigating the conformations of gelatin in solution and its adsorption onto the surfaces of colloidal latex particles [41]. Modeling the obtained SANS signals with spherical core-shell structures provided estimates of the radius of particle cores and subsequent calculations of the gelatin corona thickness. A similar method was utilized in other studies [42, 43, 44]. Notably, in an interesting study by Li et al. [45], they employed neutron isotope sensitivity to observe "stealth" polymeric coatings in the form of an ultrathin poly(acrylic acid) shell on iron-oxide superparamagnetic nanoparticles. They demonstrated that dynamic light scattering measurements overestimated the hydrodynamic radius of the particles, resulting in exaggerated estimates of the shell thickness. On the other hand, SAXS

and SANS were applied in a complementary way to characterize heavy iron-oxide cores of the nanoparticles and lighter polymer coating, respectively. Besides structural information of polymer coatings in the form of coating thickness and composition, neutron scattering can be effectively used in the studies of polymer chain conformations. In an early study, Ho et al. [46] used SANS to investigate chain conformations in polymer thin films composed of protiated and deuterated polystyrene on a flat silicon substrate. The measurements were done on film thicknesses that are 10-fold the unperturbed radius of gyration. Their results showed no dependence of the scattering signals on the film thickness. However, their experiment demonstrated the possibility of quantitative SANS studies on single thin films. In a later SANS experiment, the same group investigated chain structure in ultra-thin polystyrene films [47]. They stacked several wafers of identically prepared samples to improve the signal-to-noise ratio. Their measurements revealed Gaussian conformation in the direction parallel to the substrate. However, thinner films showed systematic trends indicative of chain swelling. The combination of SAXS and SANS is also a powerful approach to studying polymer-grafted nanoparticles, enabling complementary characterization of the particle and polymer properties. For example, combined SANS and SAXS measurements have been utilized in studies of nanocomposites with polymer grafted nanoparticles [48]. These studies often take advantage of the unique isotope sensitivity of neutrons by selective deuteration of the brush or polymer matrix. For instance, selective deuteration of the polymer brush amplifies the brush scattering signal used in determining the brush structure, e.g., brush thickness and chain conformations[49]. In comparison, SAXS measurements are generally more sensitive to the particle cores (typically made of heavier elements), resulting in signals that describe the core shape and dispersion. The synergistic combination of SANS and SAXS thus provides a practical approach for elucidating the dependence of particle dispersion on brush structure and wetting state.

Reflectometry and Grazing Incidence Scattering. Despite the high penetration power of neutrons, they can be made to reflect off surfaces through grazing incidence. At such low incident angles, the energy carried by the normal component of the neutron scattering wavevector (Fig. 2.1 b,c) becomes comparable to, or smaller than, the scattering potential of the substrate, resulting in scattering back into the incident medium. Thus, grazing incidence scattering techniques are convenient for measuring variations in the scattering potential (or SLD) normal or lateral to the probed surface. This is more effective for characterizing the structure and thickness of flat surfaces or substrates coated with polymer [50]. Two scattering techniques that are commonly applied in probing surface structures, in-depth structural features, and near-surface effects are reflectometry and grazing-incidence SAXS/SANS (GISAXS and GISANS) [51]. Variations of these techniques have been utilized in studies of polymer films, coatings, and surface patterns, including spin-echo resolved grazing incidence scattering (SERGIS) [52, 53], and off-specular reflection [31, 54, 55], but the most common approaches are standard reflectometry and GISAS techniques. In "specular" reflectometry experiments, neutrons impinging on a substrate get reflected with the same incident angle onto a detector (Fig. 2.1b) where variations of the reflected intensity are measured as a function of the momentum transfer Q. This technique utilizes a sheet geometry of the incident beam with tight collimation along the scattering direction (i.e., incident angle) and relaxed collimation in the perpendicular direction (i.e., parallel to the substrate surface) (Fig.2.1b). Models to analyze reflection data are based on analytical solutions of reflection and transmission coefficients of the neutron wavefunction in the vicinity of the probed surface. The calculations are based on solutions of the neutron wavefunction in the different potential regions and applying boundary conditions, in the form of continuity of the wavefunction and its derivative, at the interfaces. In the simple case of a single homogenous film on top of a substrate, the width of these fringes determines the film thickness (inversely proportional), and their depth is correlated with the SLD difference between the substrate and the film.

For samples with in-depth structural variations, the scattering potential is modeled as a thin layer parallel to the surface, each with a scattering length density representing the average SLD of that layer. This thin-slicing approach is referred to as the Parratt formalism [56], and is frequently used in reflectometry models. In such cases, the calculation of the reflection coefficients requires the application of the boundary conditions at all interfaces between the assumed layers, taking into account the Fresnel reflection and transmission coefficients in each layer [36]. The signal often shows a superposition of multiple fringes with different widths and features for multiple coatings on a substrate. In such a case, a Parratt recursion algorithm [56] is typically used to provide information on layer thicknesses and in-depth variables. The high resolution of NR enables structural studies of interfaces and layers to within a few Å, enabling detailed measurements of the layer structure, composition, and interfacial roughness [36]. NR signals are typically characterized by a series of fringes called Kiessig fringes. Fitting of NR signals with sliced models is available in several dedicated data-fitting software packages, such as MOTOFIT [57].

On the other hand, GISANS, much like grazing incidence X-ray scattering (GISAXS), is used for studying lateral structures in thin films and near the free surface of substrates. This concept was elegantly illustrated by Levine et al. [58], who demonstrated the effective use of grazing incidence scattering in detecting nanoscale "islands" or clusters of gold formed at the initial stages of thin film growth. The technique is based on a grazing-incidence geometry in which the momentum transfer, Q , is not constrained to the direction normal to the substrate surface but is also resolvable in the lateral direction, i.e., parallel to the substrate surface (Fig.2.1c). In other words, GISANS is a hybrid of reflectometry and SANS techniques. This enables measurements of the thickness, lateral size, and spatial correlations of structures' patterning films and surfaces. Notably, time-of-flight GISANS (TOF-GISANS) enables the use of the entire wavelength spectrum generated by pulsed neutron sources to

access a wider Q range, allowing measurements of structures over extended length scales in a single exposure [59]. A detailed description of the fundamental principles and experimental details of GISANS applications to polymer films can be found in a recent review by Müller-Buschbaum [51].

GISANS can be effectively used in investigating layered structures of copolymer films. For example, GISANS has been implemented in studies of bulk and near-surface assemblies in triblock copolymers films [60] of the ABA-type, made of polyparamethylstyrene (A) and polystyrene (B). The experiment was performed such that the beam was incident from the substrate. Increasing the incident angle enabled measurements of lateral polymer structures at various depths, i.e., close to the interface and away from the interface (bulk-like properties). Analysis of the scattering intensity component parallel to the surface showed an increase in the lamellar spacing of the copolymer close to the substrate interface compared to the bulk spacing. The measurements also revealed that the copolymer spacing near the substrate is affected by surface treatment and converges to the bulk value away from the interface.

NR measurements have been successfully utilized in numerous studies on polymer coatings [61, 62, 63, 64, 65]. For instance, early studies by Siqueira et al. [61] showed the importance of NR in understanding the interactions between immiscible polymer layers. Access to the width of the interface between polystyrene and poly (n-butyl methacrylate) (PnBMA) layers enabled calculations of the Flory-Huggins interaction parameter, an important thermodynamic descriptor of polymer blends and mixtures. Similarly, Torikai et al. [66] used NR to report early observations of molecular ordering in block copolymers of polystyrene (PS) and poly(2-vinylpyridine) (P2VP). These experiments utilized full and partial deuteration of the PS block. The results indicated preferential segregation of the P2VP blockchains to the silicon surface and PS blockchains to the air surface. The data also suggested that an error

function well described the segment distribution PS-P2VP interfaces and that the blocks were intensely segregated. Another advantage of NR is the accuracy in measuring the mass density of polymer thin films. This capability was utilized by Wallace et al. [67] in calculating the mass density of polystyrene thin films coated on a silicon substrate. Using an approach named twin reflectometry, i.e., reflectometry from both sides of the film (free surface and substrate side), they showed that the mass density of thin films is close to its bulk value and is not a function of the film thickness. However, these conclusions were contradicted by X-ray reflectivity measurements reporting variations in the electron density across the depth of PS thin films [68]. More recent observations support the concept of density variations in polymer thin films away from interfaces [69], pointing to the importance of synergistic integration of complementary characterization methods. Indeed, complementary techniques are common in studies of polymer coatings and their applications. For example, Kirschner et al. used a suite of characterization methods, including neutron/X-ray reflectivity and AFM, to study the electronic properties of polymer blends of phenyl-C61-butyric acid methyl ester (PCBM) and poly(bromo)styrene and bilayers with poly(3-hexylthiophene) (P3HT) [70]. They found that the addition of small concentrations of styrene polymers facilitated the processing of the films while maintaining the required electron mobility. Their reflectivity results show that PCBM is partially mixed with P3HT in films prepared by spin-coating PCBM from a solution with poly(bromostyrene) to form an overlying film. Interestingly, introducing the bromo moiety in PS increased the X-ray scattering length density of the upper layer and showed increased film smoothness.

Another attractive application of polymer coatings is their use as scaffolds for cell growth and as cushions for studies of cell membranes. For example, in an experiment to model cellular cytoskeleton interactions, El-Khoury et al. deposited lipid bilayers, with ion channels, on pH-responsive poly(acrylic acid) cushions [71]. Neutron and X-ray reflectivity studies showed

that the activation of the ion channels resulted in swelling of the polymer cushion due to ion transfer through the lipid membrane.

In another study, Jablin and co-workers employed specular NR to understand the effect of deposited lipid membranes on the swelling of thermoresponsive poly(n-isopropylacrylamide) (PNIPAM) cushions [54]. Their studies showed that the fluidity state of the supported lipid bilayers significantly impacted the hydration profile and thickness of the PNIPAM cushion, with gel lipid membranes effectively restricting water permeation and cushion swelling. These studies also utilized off-specular neutron scattering to probe interfacial fluctuations and in-plane height-height correlations in the studied lipid bilayer. A later study by Zhernenkov, Ashkar, et al. [31] utilized PNIPAM coating on lithographically patterned silicon substrates to demonstrate the effective use of tunable, structured polymeric surfaces as scaffolds for cell alignment and release in tissue growth applications. To characterize the PNIPAM coating, they conducted their NR measurements on the scaffolds in D_2O instead of H_2O to amplify the neutron scattering contrast between the solution and the polymer coating. Given the periodic nature of the substrates, the neutron scattering experiments resulted in strong off-specular scattering signals in the form of Bragg rods, which were interpreted using a dynamical theory model developed earlier by Ashkar et al. [30]. Analysis of the intensity variations along the Bragg rods above and below the lower critical transition temperature (LCST) of PNIPAM, i.e., in the collapsed and swollen states of the polymer coating, enabled calculations of the polymer thickness and hydration levels in each state. They found that the polymer coating conformed to the underlying substrate lithography in the collapsed state, providing the necessary directionality for cell alignment. However, in the swollen state, the coating expanded significantly – filling the underlying substrate features and resulting in a pseudo-flat surface. This characterization was key to understanding the alignment of fibroblast cells grown onto the scaffolds above LCST and the effective cell release with

decreasing temperature.

Neutron reflectometry (NR) has also been utilized in other studies for probing lateral structures of polymer thin films while simultaneously measuring in-depth variables. For instance, Aoki et al. [65] applied a novel neutron reflectometry tomography technique to generate real-space images of in-plane structures of polymer thin films. They used a sheet-shaped neutron beam using a pair of slits and a two-dimensional position-sensitive neutron detector. Their method enabled direct measurements of the structure of inhomogeneous interfaces in polymeric films formed of protiated and deuterated poly(methyl methacrylate) (PMMA). The SLD depth profiles of the films and their lateral features were measured by rotating the sample and performing time-of-flight NR measurements. Analysis of the NR data from the local area that was probed enabled a 3D reconstruction of the chemical components of thin films characterized by in-plane inhomogeneity.

2.2 Inelastic and quasi-elastic scattering

Contrary to structural characterization methods, studying sample dynamics requires knowledge of the energy exchange during scattering events. This can be done using inelastic or quasi-elastic scattering techniques which are designed to resolve small changes in the neutron energy incurred during scattering [72, 73]. A distinguishing feature between inelastic and quasi-elastic scattering is the relation of detected neutron energy differences to excitation energies within the sample. If the neutron energy exchange is comparable to excitation energies, the scattering is referred to as inelastic and is characterized by significant energy shifts that manifest as distinct signals in the scattered energy spectrum. In contrast, quasi-elastic scattering is characterized by small changes in the neutron energy and manifests as broadening around elastic lines or as a change in dynamic relaxations. Among neutron spectroscopy

techniques commonly used in probing polymer dynamics are neutron spin-echo spectroscopy (NSE), neutron backscattering spectroscopy (BSS), and neutron time-of-flight spectroscopy [23, 74]. These techniques enable studies of nanoscale processes (∼0.1-100 nm) on very fast timescales (∼ ps to ns). Considering the analogous timescale of motions in polymeric materials [75], neutron spectroscopy methods serve as a unique probe for molecular and collective polymer dynamics. Interestingly, comparable length and time scales are typically probed by molecular dynamics simulations, positioning neutron spectroscopy methods as cutting-edge tools in the advanced characterization of polymeric materials [76, 77]– especially when combined with complementary approaches for a fuller dynamic characterization of polymeric systems [78]. Accordingly, neutron spectroscopy techniques have been utilized in numerous studies to probe molecular mobility, dynamics, and glass transitions in polymeric thin films [79, 80, 81, 82]. In some cases, combinations of these techniques such as time-of-flight and backscattering is effectively used to investigate other dynamical properties, such as the vibrational density of states and mean square displacement of molecules in nanoconfined polymer systems[83].

For instance, neutron spin-echo (NSE) studies on polymer nanocomposites have provided unique and quantitative measurements of polymer dynamics in various nanocomposites. For example, Poling-Skutvik et al. [84] used NSE to investigate the dynamics of high molecular weight polystyrene chains grafted onto silica nanoparticles under osmotic compression in a solution of chemically similar linear polymer with partial deuterium labeling of the linear chains. They analyzed the structure and dispersion of these nanocomposites using SANS and SAXS. They observed a dispersed state in the relatively low polymer concentration and aggregated structures at high concentrations. Furthermore, the aggregation of the polymer-grafted nanoparticles was correlated with the impenetrability of the brush, leading to the compression of the chains. Their NSE results revealed Zimm-like dynamics at

short timescales, indicating that the solvent viscosity and hydrodynamic interactions control the polymer relaxations, like free polymer chains. However, observations at long timescales showed emergent confinement effects, suggesting that grafted polymers relax more slowly than free chains. They explained this behavior by comparing the confinement length in the presence of free linear polymer and the confinement length scale in the case of grafted chains. They concluded that the confinement length decreases with the increase in the local effective grafting density.

2.3 Coherent and incoherent neutron scattering

Another unique feature of neutron scattering is that it has two components: a coherent and an incoherent scattering component [85, 86, 87]. The coherent component results from the interaction of the neutron wave with all nuclei with well-defined relative phases. In other words, coherent scattering depends on the relative distances of the nuclei or atomic ensembles. If these scattering events do not involve energy exchange, i.e., elastic coherent scattering, then the scattering signal yields information about the equilibrium structures and enables structural characterization of the sample. However, in the case of energy exchange, i.e., inelastic coherent scattering, the obtained signal encodes information about relative motions of atoms or atomic ensembles and are thus suited to studies of collective dynamics. In contrast, incoherent scattering resembles the case where the neutron wave interacts independently with nuclei, resulting in random relative phases of the scattered waves. For example, the interaction of a neutron wave with the same nucleus at different positions or times results in incoherent scattering signals that can inform about self-diffusive motions within the sample. As seen in Fig. 1.1, different chemical elements and elemental isotopes can result in dramatically different contributions to the coherent and incoherent neutron

scattering signals. For example, hydrogen (H) – an abundant element in polymer materials – exhibits an incoherent scattering cross-section that is 40 times larger than its coherent cross-section. In structural measurements, this often results in a rather undesirable incoherent background signal that obscures weaker coherent scattering signals. However, this large incoherent scattering cross-section is an advantage in studies of self-dynamics of H-rich moieties.

Chapter 3

Dynamical Theory analysis of reflection from periodic structures

Overview

This chapter elaborates on the theoretical bases for the modeling framework we developed for optimizing the fits of scattering measurements to the theoretical predictions based on the dynamical theory. The model will be used in the following chapters of this dissertation for application in nanofluidics, polymer-coated patterned substrates, and membrane-protein interactions. First, we will review the bases of the specular reflectivity from flat unstructured substrates and thin films. Then we will discuss the dynamical theory, which was previously developed and validated for neutron scattering characterization of periodic nanostructures [30]. We will discuss how it can be expanded for the case of electromagnetic waves with the X-ray wavelength range. Lastly, we will discuss how this method can be applied to more complicated cases, such as in-depth varying profiles and layered surfaces, including soft material coatings on patterned substrates.

3.1 Neutron interaction with matter

Consider a monoenergetic neutron beam with a wave function of

$$\Psi(\mathbf{r}) = e^{i\mathbf{k}.\mathbf{r}} \tag{3.1}$$

with k as the free space wave number,

$$k = \sqrt{\frac{2mE}{\hbar^2}} \tag{3.2}$$

where $\hbar$ is Planck's constant, and m is the mass of the neutron. When interacting with matter, it experiences an interaction potential V(r),

$$V(\mathbf{r}) = \frac{2\pi\hbar^2}{m}\rho(\mathbf{r}) \tag{3.3}$$

in which $\rho(r)$ is the coherent scattering length density of the medium and is determined by the composition of the matter

$$\rho(\mathbf{r}) = \sum_n b_n N_n(\mathbf{r}) \tag{3.4}$$

Here b_n and N_n represent the number density and scattering length of nth isotope [36]. Considering that the Schrodinger equation describes the wavefunction of the neutron beam,

$$[-\frac{\hbar^2}{2m}\nabla^2 + V(\mathbf{r})]\Psi(\mathbf{r}) = E\Psi(\mathbf{r}) \tag{3.5}$$

As a result:

$$\nabla^2\Psi(\mathbf{r}) + [k^2 - 4\pi\rho(\mathbf{r})]\Psi(\mathbf{r}) = 0 \tag{3.6}$$

Interestingly, this equation can be expressed in the form of a standard Helmholtz equation;

$$\nabla^2\Psi(\mathbf{r}) + \xi^2(\mathbf{r}) = 0 \tag{3.7}$$

where

$$\xi = \sqrt{\frac{2m[E - V(\mathbf{r})]}{\hbar^2}} = \sqrt{k^2 - 4\pi\rho(\mathbf{r})} \tag{3.8}$$

and is equivalent to the wave number inside matter. Due to the similarity of equation 3.7 with that of light, a refractive index for neutron in the matter can be defined as:

$$n = \frac{\xi}{k} = \sqrt{1 - \frac{\lambda^2}{\pi}\rho(\mathbf{r})} \tag{3.9}$$

where $\lambda = \frac{2\pi}{q}$. For thermal neutrons with energy of about 25 meV and wavelength of few Å, the neutron refractive index can be approximated to

$$n \approx 1 - \frac{\lambda^2\rho}{2\pi} \tag{3.10}$$

Notably, at an interface between various media (represented by indices of a and b) with different SLDs, the boundary conditions necessitate the continuity of the wavefunction and its first derivative:

$$\begin{aligned} \psi^a &= \psi^b \\ \frac{\partial\psi^a}{\partial n} &= \frac{\partial\psi^b}{\partial n} \end{aligned} \tag{3.11}$$

where $\vec{n}$ is the normal to the interface.

3.1.1 X-ray interaction with matter

The equations governing the behavior of electromagnetic waves in the wavelength range of X-rays can be obtained from Maxwell's equations. In media with bound electrons, these

equations are:

$$\begin{aligned} \nabla \times \mathbf{E} &= -\frac{\partial \mathbf{B}}{\partial t} \\ \nabla \times \mathbf{H} &= \frac{\partial \mathbf{D}}{\partial t} \\ \nabla \cdot \mathbf{D} &= 0 \\ \nabla \cdot \mathbf{B} &= 0 \end{aligned} \tag{3.12}$$

where $\mathbf{E}$ is the electric intensity, $\mathbf{B}$ is the magnetic flux density, $\mathbf{H}$ is the magnetic intensity, and $\mathbf{D}$ is the electric flux density. In a linear medium,

$$\begin{aligned} \mathbf{D} &= \epsilon \mathbf{E} \\ \mathbf{B} &= \mu \mathbf{H} \end{aligned} \tag{3.13}$$

Here, ϵ and μ are dielectric permittivity and magnetic permeability, respectively. After taking the curl of the first two terms of equation 3.12, and using the following terms, for harmonic waves ($\frac{\partial}{\partial t} \rightarrow -\omega^2$) in homogeneous and isotropic media, we can obtain

$$\begin{aligned} \nabla^2 \mathbf{E} + \xi^2 \mathbf{E} &= 0 \\ \nabla^2 \mathbf{H} + \xi^2 \mathbf{H} &= 0 \end{aligned} \tag{3.14}$$

with $\xi = \omega^2 \mu \epsilon$. Equations 3.14 are also approximately valid for inhomogeneous media where ϵ and μ change along one direction (assumed to be the z-axis) in the wavelength range of X-rays [36]. In this case, the wave can be considered as the combination of an s-wave where the electric field points to an axis normal to the z-axis (here considered to be the x-axis) and a p-wave where the magnetic field is directed into the x-axis.

The boundary condition for a wave propagating into an interface at $z = Z$ between two different mediums (a and b) can be obtained by taking the flux integrals of Maxwell's equations

(equations 3.12) over an element of a surface, and it can be shown that:

$$\begin{aligned} U(Z_a) &= U(Z_b) \\ \frac{\partial U(Z_a)}{\partial z} &= \frac{\partial U(Z_b)}{\partial z} \end{aligned} \tag{3.15}$$

where U represents the electric field in s-waves and the magnetic field in p-waves. Furthermore, it can be shown that

$$\epsilon = \epsilon_0(1 - \frac{\lambda^2 \rho(\mathbf{r})}{\pi}) \tag{3.16}$$

where ρ is the scattering length density of the medium for electromagnetic waves and is a function of electron density, $N_e(\mathbf{r})$ and the classical radius of the electron, r_0,

$$\rho(\mathbf{r}) = r_0 N_e(\mathbf{r}) \tag{3.17}$$

Therefore, the refractive index is derived as

$$n = \frac{\xi}{k} = \frac{\omega}{k}\sqrt{\epsilon\mu} = \sqrt{1 - \frac{\lambda^2 \rho(\mathbf{r})}{\pi}} \tag{3.18}$$

For X-rays, it can be approximated as

$$n \approx 1 - \lambda^2 \frac{\rho(\mathbf{r})}{2\pi} \tag{3.19}$$

Interestingly, equations 3.14 are in the format of the Helmholtz equation obtained for neutrons (equation 3.7), with similar boundary conditions, equations 3.15, resembling those for neutrons (3.11). This motivates the application of scattering theories derived from neutrons to the case of X-rays scattering. As a result, the theoretical models in the following sections

of this chapter are equivalently applicable to X-rays and neutrons.

3.1.2 Reflection at an interface

In the simplest case of specular reflection, a beam incident from the air incident reflects from a substrate. Figure 3.1 depicts the case in which a plane wave with a wavenumber k_0 interacts with a scattering potential at $z = 0$, which is proportional to the scattering length density of the substrate, ρ_s.

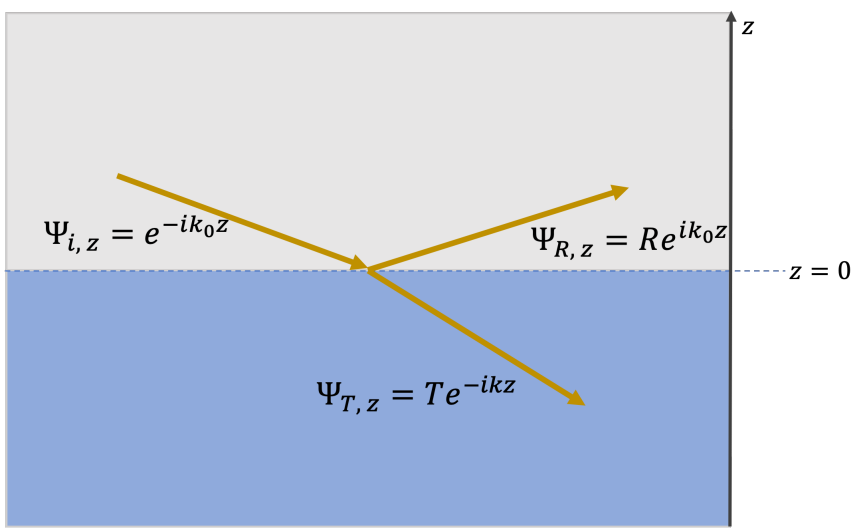

Figure 3.1: Incidence of a plane wave with wave number of k_0 from air to the surface of a substrate at $z = 0$, resulting in reflected and transmitted waves, with amplitudes of R and T, respectively. The wave number in the substrate is k.

As the potential depends only on the z-direction, the wavefunction can be considered the product of eigenstates in each direction. We can simply solve the Schrodinger equation in the z-direction,

$$\begin{aligned} \frac{\partial^2 \psi_z(z)}{\partial z^2} + k_{0,z}^2 \psi_z(z) = 0, z \geq 0 \\ \frac{\partial^2 \psi_z(z)}{\partial z^2} + k_{s,z}^2 \psi_z(z) = 0, z \leq 0 \end{aligned} \tag{3.20}$$

where $k_{0,z}$ is the wavevector along z in the air, $k_{0,z} = \frac{2\pi}{\lambda} \sin\theta$ with θ as the incident angle,

and $k_{s,z}$ is the z-component of the wavevector the substrate, k_s:

$$k_s = \sqrt{\frac{2m(E-V)}{\hbar^2}} = \sqrt{k_0^2 - 4\pi\rho_s} \tag{3.21}$$

The solutions to these equations are simply

$$\begin{aligned} \psi_z(z) &= e^{-ik_{0,z}z} + Re^{ik_{0,z}z}, z \geq 0 \\ \psi_z(z) &= Te^{-ik_{s,z}z}, z \leq 0 \end{aligned} \tag{3.22}$$

As a result, the beam is partially reflected with a reflection coefficient of R and partly transmitted with a transmission coefficient of T. The reflection and transmission coefficient in these equations can be obtained by applying boundary conditions (equations 3.11), which gives

$$\begin{aligned} R &= \frac{k_{0,z} - k_{s,z}}{k_{0,z} + k_{s,z}} \\ T &= \frac{2k_{0,z}}{k_{0,z} + k_{s,z}} \end{aligned} \tag{3.23}$$

3.1.3 Reflection from a uniform thin film

For the more complex case of a uniform film with a thickness of t and SLD of ρ_f on top of the substrate, reflection, and transmission in the film also should be accounted for. In this case, the Schrodinger equations in three different regions in the z direction are

$$\begin{aligned} \frac{\partial^2\psi_z(z)}{\partial z^2} + k_{0,z}^2\psi_z(z) &= 0, z \geq t \\ \frac{\partial^2\psi_z(z)}{\partial z^2} + k_{f,z}^2\psi_z(z) &= 0, 0 \leq z \leq t \\ \frac{\partial^2\psi_z(z)}{\partial z^2} + k_{s,z}^2\psi_z(z) &= 0, z \leq 0 \end{aligned} \tag{3.24}$$

Where $k_{f,z}$ is the z-component of the wavenumber in the film with $k_f = \sqrt{k_0^2 - 4\pi\rho_f}$. Similarly, the solution to these equations are

$$\begin{aligned} \psi_z(z) &= e^{-ik_{0,z}z} + Re^{ik_{0,z}z}, z \geq 0 \\ \psi_z(z) &= Ae^{-ik_{f,z}z} + Be^{ik_{f,z}z}, 0 \leq z \leq t \\ \psi_z(z) &= Te^{-ik_{s,z}z}, z \leq 0 \end{aligned} \tag{3.25}$$

The continuity relations at the film's two interfaces with air and substrate result in the reflection and transmission coefficient calculations.

$$\begin{aligned} R &= \frac{-(k_f - k_0)(k_f + k_s) + (k_f - k_s)(k_f + k_0)e^{2ik_f t}}{(k_f + k_s)(k_f + k_0) - (k_f - k_0)(k_f - k_s)e^{2ik_f t}} e^{-2ik_0 t} \\ T &= \frac{4k_0 k_f e^{i(k_f - k_0)t}}{(k_f + k_s)(k_f + k_0) - (k_f - k_0)(k_f - k_s)e^{2ik_f t}} \end{aligned} \tag{3.26}$$

The film's thickness and SLD can be obtained by fitting the experimental reflection intensity

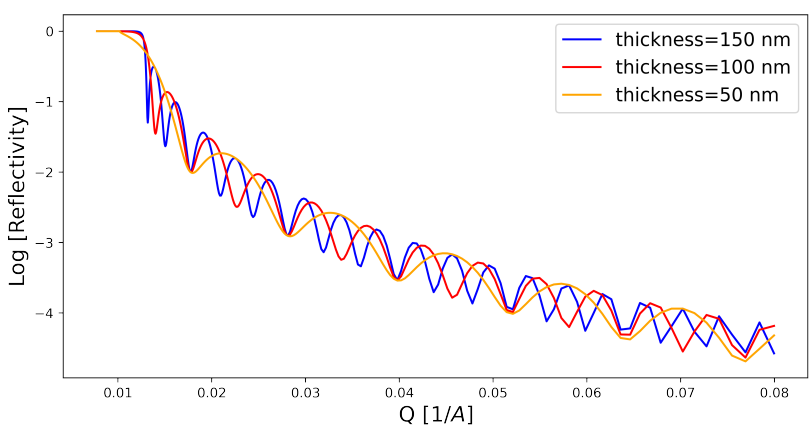

Figure 3.2: Reflected intensity as a function of the momentum transfer, Q, for a uniform thin film on top of a substrate for various thicknesses of 50 nm, 100 nm, and 150 nm.

to this theoretical prediction. Notably, it can be shown that the Kiessig fringes distance at relatively high wavenumbers in the reflected intensity plot is inversely proportional to the

thickness of the film. Figure 3.2 illustrates the reflected intensity for different thicknesses of the uniform film coated on flat substrates, showing that the distances between successive fringes increase by decreasing the thickness of the film.

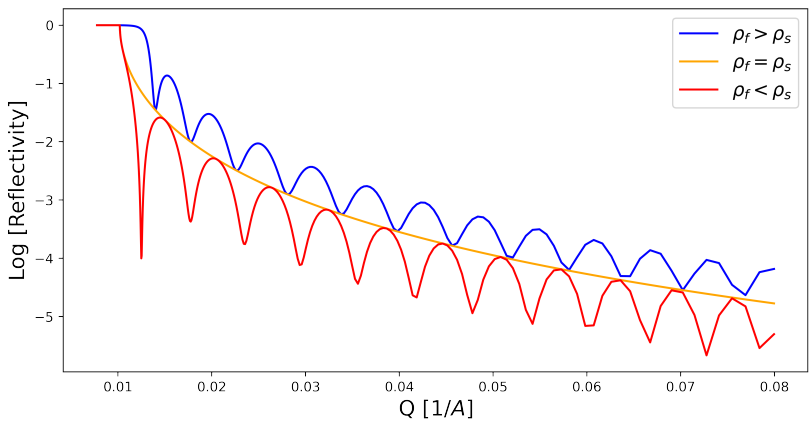

Figure 3.3: Reflected intensity as a function of the momentum transfer, Q, for a uniform thin film on top of a substrate for various scattering length densities of the film (ρ_f) in comparison with the substrate (ρ_s).

The reflected intensity also depends on the SLD of the film in comparison with the SLD of the substrate itself. If the SLD of the film is higher than that of the substrate, the fringes in the reflected intensity graph are on the top of the substrate reflectivity, as in this case, the beam experiences the higher potential of the film. On the other hand, the opposite trend occurs when the SLD of the film is lower than that of the substrate (see figure 3.2.). Moreover, as the SLD approaches its substrate value, the fringes fade, and the reflected intensity approaches that of the substrate case.

3.1.4 Interfacial roughness

The interface between different media usually has a roughness, resulting in the reflection in many directions and, more importantly, a statistically averaged effect on the specular

reflection of the beam impinging on the interface. The effect of the surface roughness on the reflected intensity depends on the beam's wavelength and incident angle [88]. Theoretically, it is shown that roughness causes an exponential decay in reflected intensity for a single interface as [89, 90]:

$$R_r = Re^{-q_z q_{z,t} \sigma^2/2} \tag{3.27}$$

where R_r and R are the reflection coefficient of the rough and smooth surface, q_z and $q_{z,t}$ are

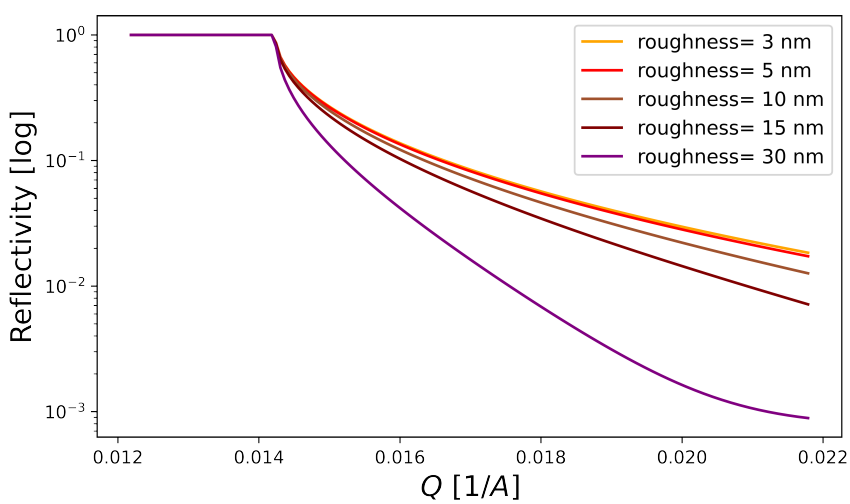

Figure 3.4: Reflected intensity as a function of the momentum transfer, Q, for an interface with various degrees of interfacial roughness.

the wave vector transfer in different media, and σ represents the roughness which is defined as the root square of the variance of height distribution of the surface. Interfacial roughness can be computationally modeled by considering several sub-layers at adjacent interfaces and gradually changing SLD between layers. A larger number of sublayers results in a function of the interfacial roughness function. However, increasing the number of sub-layers comes at the expense of computational time.

3.1.5 Reflection from laterally structured thin films, Dynamical Theory

So far, we observed how specular reflection could be adequately used to determine in-depth variables or average parameters along the direction normal to the surface. However, for the lateral structure of the substrate or thin films, the off-specular scattering patterns should be decoded to retrieve the profile of the sample. In such a case, the scattering potential also varies in the lateral direction, which should be simultaneously solved to fit with the experimental signal and reconstruct the substrate profile. Among various patterned thin films, periodic nanostructures have significant implications in various fields, particularly biotechnology. In the following section of this chapter, we briefly explain dynamical theory (DT), which was previously proposed by Ashkar et al.[30] to interpret the scattering pattern of periodic thin films. Dynamical theory (DT) is an exact theoretical model to interpret reciprocal patterns of strong off-specular scattering from periodic structures and to retrieve the profile of the sample with high precision[30, 31, 91].

DT is based on a description of the Bloch waves due to a periodic potential. Similar to previous sections, the Hamiltonian is separable, and we can solve the Schrodinger equation independently. The neutron wavefunctions are 3-dimensional plane waves in the air and the substrate, similar to the previous cases. However, in this case, the intermediate layer has a laterally periodic SLD (here we consider it in the y-direction), resulting in a periodic potential that can be expressed as a Fourier expansion:

$$\rho(z) = \begin{cases} 0; & z > 0 \\ \sum_l \rho_l \, e^{i\frac{2\pi l y}{d}}; & 0 > z > -t \\ \rho_s; & z < -t \end{cases} \tag{3.28}$$

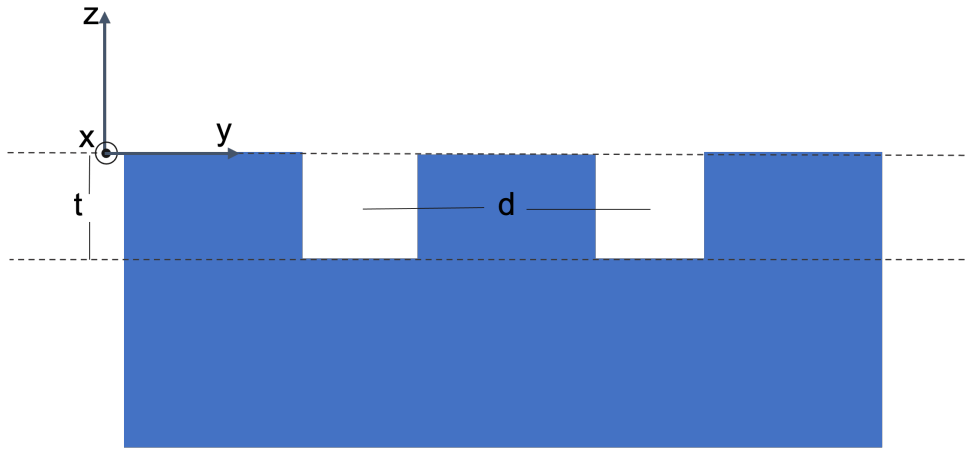

Figure 3.5: A rectangular pattern that is periodic along the y direction, with a thickness of t and a period of d. These structures are typically divided into three layers: air, the modulated layer, and a substrate.

where d and t are the period and depth of the periodic layer. The coefficient ρ_l can be determined based on the filling factors and the period of the layer [30]. According to the Bloch theorem, the solution to the Schrodinger equation of the eigenstates along y direction in the modulated layer, in general, are given by one-dimensional Bloch waves:

$$\psi_{y,n} = e^{ik_{0,y}y} \sum_m b_{n,m} e^{i\frac{m2\pi y}{d}} \tag{3.29}$$

in which $b_{n,m}$ are the Bloch coefficient required to be determined. Hence, due to the periodic potential along y, the wave number in that direction is quantized, with quantization inversely proportional to the period:

$$k_{y,m} = k_{0,y} + \frac{2\pi m}{d} \tag{3.30}$$

This quantization of the momentum along y can be graphically expressed in truncation rods or Bragg rods separated by spacings of $2\pi/d$. Putting the general Bloch eigenstates of equation 3.29 and scattering length density expansion from equation 3.28 into the Schrodinger

equation along y direction, a set of equations are obtained:

$$[(k_{0,y} + \frac{2\pi m}{d})^2 + 4\pi\rho_0 - \frac{2m}{\hbar^2}E_{n,y}]b_{n,m} + 4\pi\sum_{p\neq m}\rho_{m-p}b_{n,m} = 0 \tag{3.31}$$

where $E_{n,y}$ are the associated eigenvalues. As a result, the general wavefunctions in the y-z plane in different regions are:

$$\begin{cases} \psi_{air} = e^{i(k_{0,y}y - k_{0,z}z)} + \sum_m R_m e^{ip_{0,m}z} e^{i(k_{0,y}+\frac{2\pi m}{d})y} \\ \psi_{layer} = \sum_{n,m}[R_{1,n}e^{ip_{1,n}(z+t)} + T_{1,n}e^{-ip_{1,n}z}]b_{n,m}e^{i(k_{0,y}+\frac{2\pi m}{d})y} \\ \psi_{substrate} = \sum_m T_m e^{-ip_{2,m}(z+t)} e^{i(k_{0,y}+\frac{2\pi m}{d})y} \end{cases} \tag{3.32}$$

The conservation of energy determines the wave numbers $p_{0,m}$, $p_{1,m}$, and $p_{2,m}$. The conservation of energy condition is graphically expressed by an Ewald sphere, where the initial energy of the beam determines the radius of the Ewald sphere. Notably, the coefficients R_m, T_m are determined by applying boundary conditions at the interfaces between the modulated layer with air and with the substrate, which leads to the calculation of reflectivities and transmissivities [92]

$$\begin{aligned} |R^2| &= \sum_m \frac{p_{0,m}}{k_{0,z}}|R_m|^2 \\ |T^2| &= \sum_m \frac{p_{2,m}}{k_{0,z}}|T_m|^2 \end{aligned} \tag{3.33}$$

The calculated reflected intensity can then be compared to the experimentally obtained scattering intensities, from which profile parameters of the sample are predicted. This approach can be extended to more complicated profiles, such as non-rectangular gratings and layered profiles. A thin-slicing approach known as Parratt formalism is required to account for in-depth variation [56] (See Figure 3.6.) In this case, the scattering length density is expanded

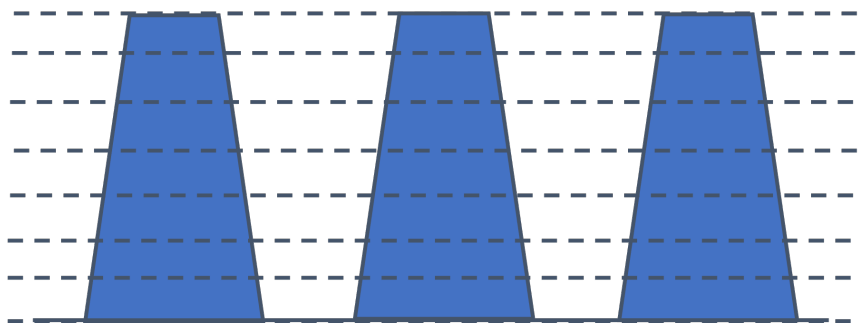

Figure 3.6: A trapezoidal periodic pattern. Thin slicing strategy can be used for non-rectangular and layered profiles for dynamical theory analysis.

with Fourier components:

$$\rho(z) = \begin{cases} 0; \quad z > 0 \\ \sum_l \rho_{1,l}\, e^{i\frac{2\pi l y}{d}}; \quad 0 > z > -t/n \\ \sum_l \rho_{2,l}\, e^{i\frac{2\pi l y}{d}}; \quad -t/n > z > -2t/n \\ \sum_l \rho_{3,l}\, e^{i\frac{2\pi l y}{d}}; \quad -2t/n > z > -3t/n \\ . \\ . \\ . \\ \rho_s; \quad -t > z \end{cases} \tag{3.34}$$

where n is the number of the sub-layers. These periodic scattering length densities result in a periodic potential in each sub-layer, so the subsequent Schrodinger equation should be solved based on them, leading to the subsequent eigenfunctions. The general wavefunction

of these equations in each sub-layer are:

$$\begin{cases} \psi_{air} = e^{i(k_{0,y}y - k_{0,z}z)} + \sum_m R_m e^{ip_{0,m}z} e^{i(k_{0,y} + \frac{2\pi m}{d})y} \\ \psi_{1,layer} = \sum_{n,m} [R_{1,n} e^{ip_{1,n}(z+t/n)} + T_{1,n} e^{-ip_{1,n}z}] b_{n,m} e^{i(k_{0,y} + \frac{2\pi m}{d})y} \\ \psi_{2,layer} = \sum_{n,m} [R_{2,n} e^{ip_{2,n}(z+2t/n)} + T_{2,n} e^{-ip_{2,n}(z+t/n)}] b_{n,m} e^{i(k_{0,y} + \frac{2\pi m}{d})y} \\ \psi_{3,layer} = \sum_{n,m} [R_{3,n} e^{ip_{3,n}(z+3t/n)} + T_{3,n} e^{-ip_{3,n}(z+2t/n)}] b_{n,m} e^{i(k_{0,y} + \frac{2\pi m}{d})y} \\ . \\ . \\ . \\ \psi_{substrate} = \sum_m T_m e^{-ip_{s,m}(z+t)} e^{i(k_{0,y} + \frac{2\pi m}{d})y} \end{cases} \tag{3.35}$$

The boundary conditions must be applied at every interface between sub-layers, resulting in the calculation of the total reflected intensity necessary for retrieving the profile of the measured sample.

This theoretical model has been validated in previous studies of neutron reflectometry measurement. For example, in a recent study, the dynamical theory was used to retrieve the lateral profile of an in-depth varying periodic diffraction grating for both bare cases and when it is buried beneath a deuterated polymer [55]. In another study, thermoresponsive polymer film was coated on a rectangular grating to allow cell release by changing the temperature [31]. In the latter, the deuterated solution was used to enhance the neutron scattering contrast between silica with polymer film and subphase. These studies show the precision and high potential of the Dynamical Theory model and motivate its application in more complicated cases.

Chapter 4

Characterization of periodic nanostructures with X-ray scattering

Overview

Periodic structures such as grating surfaces are broadly applicable across different fields such as in optics [15, 93, 94], electronics [16, 95], and in biotechnology[96, 97]. For instance, in solar energy applications, they are applied to trap light and increase efficiency by increasing optical absorption and decreasing integrated reflection loss [98, 99]. In the field of plasmonics, triangular-shaped channels are used as optical waveguides for the realization of compact photonic components [100]. In astronomical applications, they are applied to increase the precision of spectroscopy in space telescopes [101]. In chemistry, gratings on silica surfaces are utilized as optical sensors to monitor chemical and biological species [17]. In biotechnology, optical grating coupler biosensors are used to improve the design of novel biomaterials, which is a critical step in developing new drugs [102]. They are also used as scaffolds in tissue engineering to control cell growth and release [31, 103]. The performance of such applications highly depends on profile precision which necessitates accurate characterization. Among different scattering characterization techniques, grazing-incidence small-angle x-ray scattering GISAXS has been widely used to characterize grating structures [104, 105, 106, 107]. GISAXS was initially proposed by Cohen et al. [58] as a "method of studying discontinuous

thin films.". In this technique, the sample is aligned near the substrate's critical angle to probe a large surface area with high-resolution sensitivity to in-depth and lateral structures. This geometry circumvents the high energy typically incurred in transmission mode techniques. This property of GISAXS is very applicable for characterizing soft matter coatings on substrates, such as polymer line grating, which otherwise is challenging with transmission modes [108]. Here in this chapter, we applied our developed modeling approach based on Dynamical Theory to a GISAXS experiment by simultaneously optimizing the fits of the reflected intensity along different Bragg's rods to retrieve the sample profiles. Our model includes thin-slicing the structure into sub-layers and using the Parratt formalism to obtain a more detailed profile of the sample by solving for the reflected and transmitted intensities in each slice.

4.1 Method

Grazing-incidence small-angle X-ray scattering (GISAXS) experiments were conducted by Prof. Ashkar at the soft matter interfaces beamline at Brookhaven National Lab. These experiments were conducted in a GISAXS mode and the scattering data were collected in the form of 2D detector images that were reduced and analyzed as described later in this chapter. In general, the energy is conserved when a beam is an incident on a sample in an elastic collision. As the energy is proportional to the wavenumber squared, any scattered beam has the same magnitude as the initial wave number, which constructs the Ewald sphere. As a result, the wavelength of the incident beam can be determined by calculating the radius of the detected Ewald sphere (see Figure 4.1.) For a grating surface, in chapter 3 we showed that the periodic potential leads to the quantization of the wave number along the grating direction, which is inversely proportional to the period (equation 3.30.) This

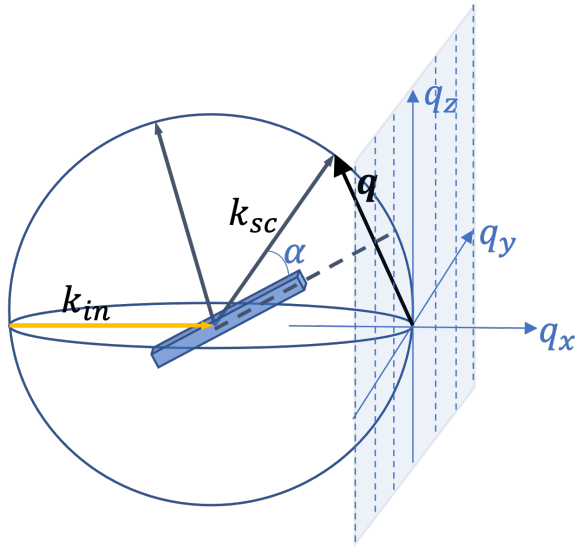

Figure 4.1: Ewald sphere provides a graphic representation of elastic scattering, where the energy is conserved, and the magnitude of the momentum of the scattered beam, k_{sc}, is equal to that of the incident beam, k_{in}. The dashed lines represent Bragg rods, resulting from the periodicity of the sample profile along the y-direction.

quantization of momentum can be graphically expressed in terms of Bragg rods (truncation rods) that are separated by spacings of $\frac{2\pi}{d}$, with d as the period of the surface patterns. On the other hand, the conservation of energy condition is graphically expressed by an Ewald sphere. Since both conditions have to be simultaneously satisfied, scattering is only possible for scattered wavevectors determined by the intersection of the Ewald sphere and the Bragg rods. The higher energy of the beam leads to a larger Ewald radius, so cross-sections with higher rod orders are possible. Moreover, if the initial momentum along y changes with changing azimuthal angle (e.g., by rotating the sample), the Ewald circle shifts across the truncation rods.

This phenomenon is beautifully illustrated in grazing incident small-angle neutron scattering measurements that are shown in figure 4.2. In these experiments, the sample is aligned such that the beam is incident at shallow angles along the lines of the grating. If the beam is along the grating lines, scattering spots are obtained at equal spacings along the Ewald sphere (See

Figure 4.2a). However, if one rotates the grating in the horizontal plane, this changes the angle between the incident beam and the grating lines, and it causes the Ewald circle to move across the rods (See Figure 4.2b,c). In a sweeping measurement, scattering data are collected as the sample is rotated between -10 and +10 degrees by accumulating spots along the Bragg rods, resulting in an intensity variation along each Bragg rod (See Figure 4.2d). The intensity variation can be modeled by dynamical theory which allows retrieving the profile of the measured sample.

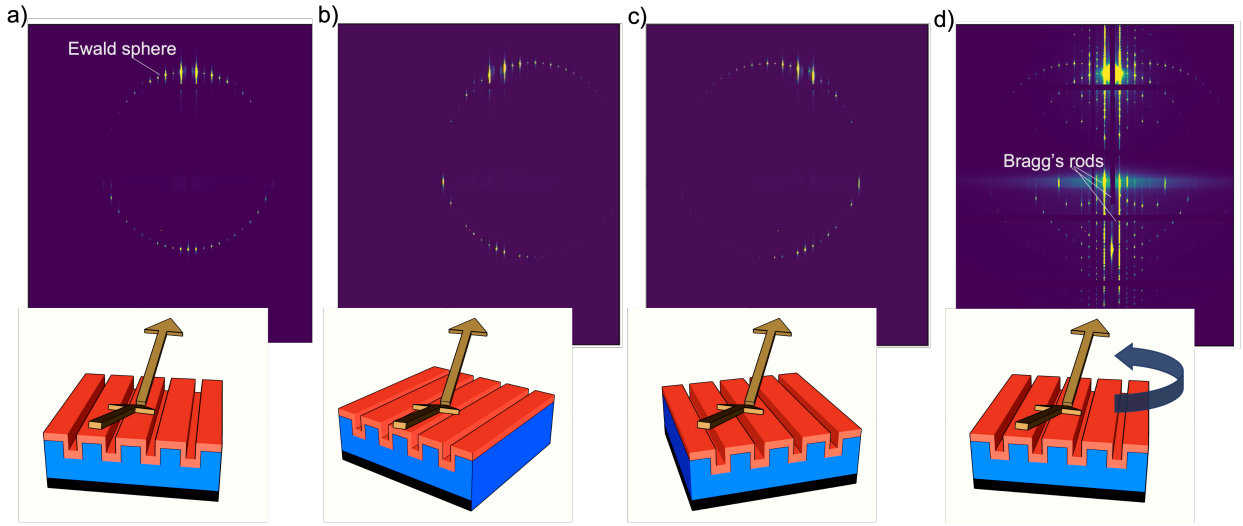

Figure 4.2: Different patterns obtained by azimuthal rotation of the sample. a) When the beam is along the grating lines, scattering spots are obtained on the edge of a symmetric Ewald circle. b) and c) When the grating is rotated in the horizontal plane, this changes the angle between the incident beam and the grating lines, and it causes the Ewald circle to move across the rods full stop d) In a sweeping measurement, data is collected as the sample is rotated between -10 and +10 degrees by accumulating spots along the Bragg rods, resulting in an intensity variation along each of the Bragg rods. This intensity variation can be modeled by DT and allows us to extract the profile of the measured sample. Upper panels are detector images collected at Beamline 12-ID, Soft Matter Interfaces (SMI) at the National Synchrotron Light Source II (NSLSII) at Brookhaven National Lab (unpublished data, courtesy of R. Ashkar and M. Zhernenkov).

4.1.1 Experiment

Linear silicon nanostamp with a size of $25 \times 25\,\mathrm{mm}^2$ with a grating periodicity of $d = 140\,\mathrm{nm}$, and thickness of $t = 50\,\mathrm{nm}$ were purchased from "LightSmyth technology" (See Figure 4.3 for the scanning electron microscopy (SEM) image). Full stop scattering measurements were

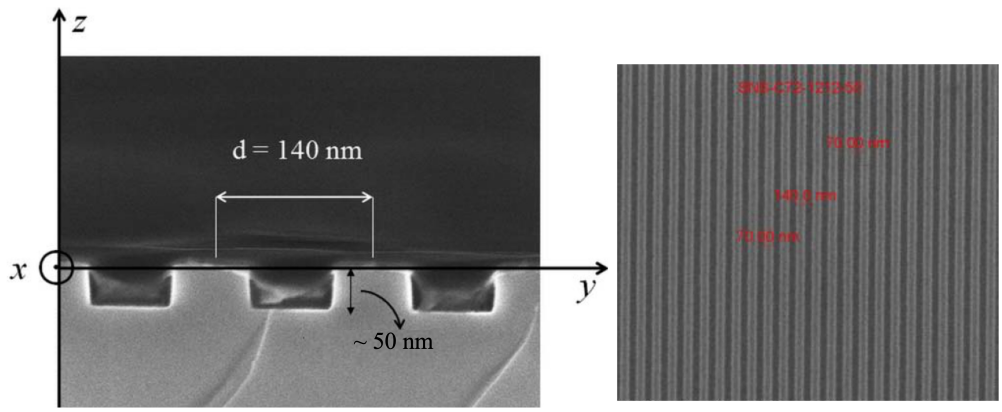

Figure 4.3: Scanning electron microscopy (SEM) images of the top and cross-sectional view of the silicon grating sample studied in this chapter. Images are provided by LightSmyth Technologies.

performed at Beamline 12-ID, Soft Matter Interfaces (SMI) at the National Synchrotron Light Source II (NSLSII) at Brookhaven National Lab. In these experiments, an X-ray wavelength of $\lambda = 0.77012$ nm were used. The distance of the detector from grating surface to the detector was set to $D = 8.3$ m, with a pixel size of (ps)= $172\,\mu\mathrm{m}$. Single snap shots were taken at an exposure of 1s each with the grating aligned along the beam direction. Sweep measurements were done between +10 and -10 degrees around the alignment angle. The total exposure time was set to 5.6s, which is roughly the time that it takes the stage to rotate by 20 degrees. Measurements were performed in air. Measurements were taken at 3 incident angles (0.35, 0.25, and 0.2) for modeling purposes both single shots and sweeps.

4.1.2 Data Analysis

Detector images in ".tif" format were provided by the CCD camera and can be visualized by "Albula" package; a package designed for the X-ray scattering measurements [109]. Library of "dectris.albula" in python were used to convert .tif images to .dat format which is readable and can be processed in python modulus. This processes digital images as matrices with elements representing the intensity. Analytical fits require intensity variation along Bragg's

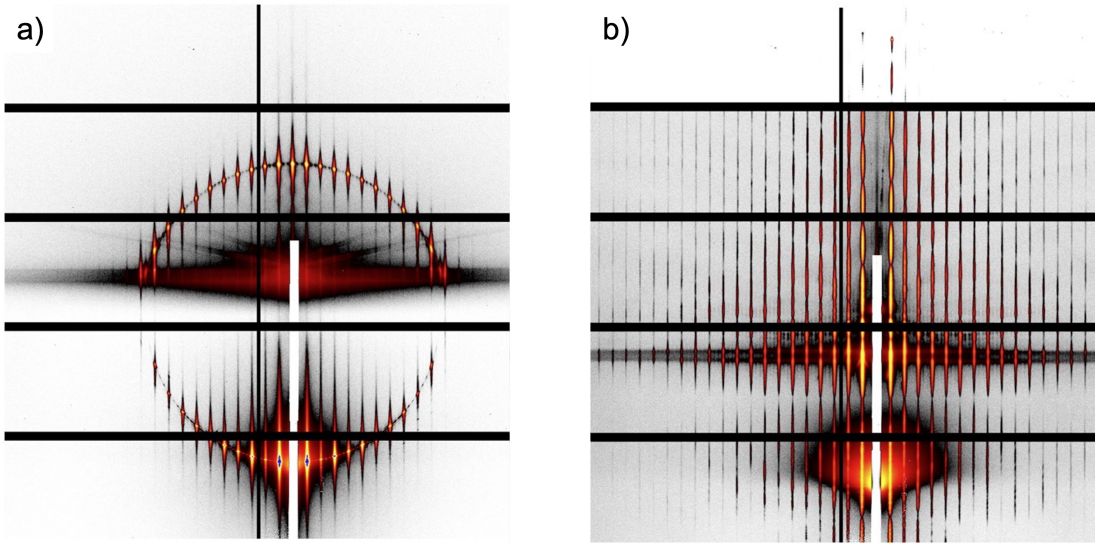

Figure 4.4: a) Ewald circle. b) A sample of image from a GISAXS experiment in an sweeping mode. The depicted detector images were collected at Beamline 12-ID, Soft Matter Interfaces (SMI) at the National Synchrotron Light Source II (NSLSII) at Brookhaven National Lab (unpublished data, courtesy of R. Ashkar and M. Zhernenkov).

rods, which were obtained by determining peaks of intensity along horizontal axis, using Python function "find-peaks" from "scipy.signal". As there was multiple images, an average were used for the analysis, to minimize the uncertainty.

For the theoretical analysis, we performed the fits to the intensity variation along multiple Bragg rods, simultaneously. Computational analysis was performed using an optimization protocol to improve the fitting process based on dynamical theory. The optimization protocol

applies the covariance matrix adaptation evolution strategy (CMA-ES) package in python [32]. CMA-ES is a stochastic numerical optimization algorithm for non-linear optimization problems in Python. We used a Python-based execution script to extract DT calculations programmed in Mathematica and employed the CMA-ES package for the fitting process. The computational protocol requires approximate initial inputs for those variables, along with their range as the upper and lower bounds. These inputs can be approximated based on the manufacture values. However, in the absence of initial parameters, we required a wider range of variable bounds. In our study, the fitting time was not substantially affected, and the computational algorithm was able to predict the structural parameters efficiently. Other measurements such as specular fits can be used to approximate the initial value of the parameter and its range as the upper and a lower bound on the fit values. The CMA-ES package generates a set of n random parameters within the specified range as training sets of variables. Based on the fit residuals (value of the fitness function) of each parameter set, the CMA-ES algorithm predicts a new set of parameters to be calculated for a new value of f. This procedure is repeated until f reaches a preset threshold. In comparing the DT calculations and the scattering data, we defined a fitness function to describe the degree of convergence:

$$f = \frac{\int_{q_i}^{q_f} [P_{theory}(q) - P_{experiment}(q)]^2 dq}{\int_{q_i}^{q_f} [P_{experiment}(q)]^2 dq} \tag{4.1}$$

where P_{theory} and $P_{experiment}$ are the theoretical and experimental quantities, which in this case, represent the reflected intensities. Also, q is the wavevector transfer. We then defined a weighted total χ^2 from fitness values to the Bragg rods (f) to determine its total convergence to the theoretical prediction. Further, for simulating the intensity variation along Bragg rods, we performed the DT calculations with 10 Bragg orders to ensure convergence. While a higher number of Bragg orders results a higher resolution of the SLD profile, it extensively increases the computational cost.

4.2 Results

We predicted structural variables with high precision by fitting the theoretical prediction to the experimental data based on dynamical theory model. We applied simultaneous fits to the intensity variation of the first three Bragg rods to reconstruct the periodic surface. The dynamical theory applies boundary conditions on the wave function and its first derivative obtained by solving Schrodinger equations for the incident and scattered waves in different regions [30] (see chapter 3.) The measured sample is a grating layer on a silicon substrate with constant SLD. We considered a thin-slicing approach with three sub-layers, with various thicknesses and filling factor to account for in-depth variation in the grating profile. The filling factor is defined as a parameter representing the fraction of silicon width to the channel width in each period. This scenario leads to a total number of six variables. These variables

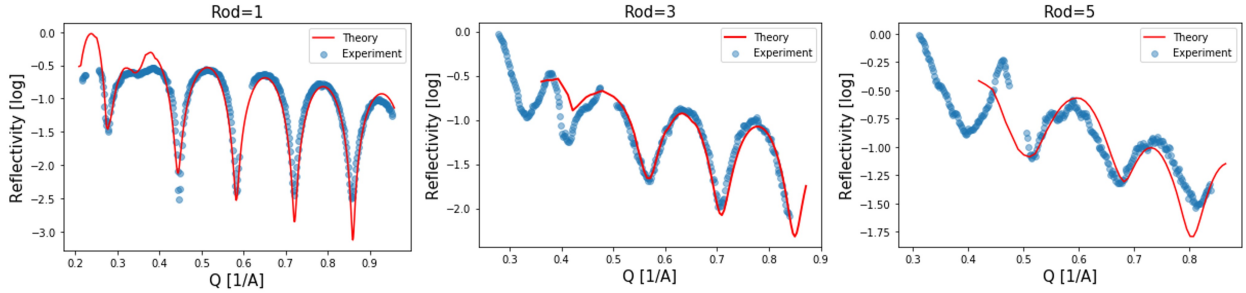

Figure 4.5: Fits to the normalized intensity variation along the first three Bragg rods, corresponding to m=1,3,5. Blue circles are experimental data obtained from processing detector images, and the red lines represent fits to them, analogous to the scattering intensity computed based on the DT model. Data are shifted vertically for easier visualization.

are updated by the covariance matrix adaptation evolution strategy (CMA-ES) during each iteration of the fitting analysis. Although a higher number of thinner sub-layers represent a more accurate grating profile model, it comes at the expense of higher computational time to converge to a preset parameter with increasing the number of variables. The fixed parameters in the calculation were the X-ray SLDs of the grating material is set to $\rho_{Si} = 19.3\times10^{-4}\,\mathrm{nm}^{-2}$,

and $\rho_{air} = 0.0 \times 10^{-4}\,\mathrm{nm}^{-2}$. The normalized fits to the intensity variations along the three odd rods are shown in Fig. 4.5 for the three-slicing scenario. The fits indicate precise prediction, particularly for the first Bragg rod, where the data incorporates wider range of q_z, with high-resolution features. For the third and fifth Brag rods, the data contains fringes in higher values of q_z, the domain equivalent to the smaller structural details. The reconstructed profile is shown in Fig. 4.6, illustrating the thicknesses and filling factors for each sub-layer. As can be seen, the profile shows wider filling factors at the bottom of the layer, leading to a trapezoidal profile. Also, our results indicates a total thickness of $\approx 45\,\mathrm{nm}$, which is close to the value presented by the SEM image in Figure 4.3.

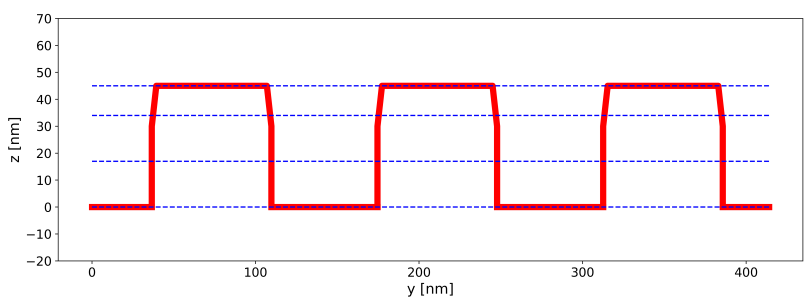

Figure 4.6: Profile of the measured sample obtained from the DT fits using the CMA-ES optimization approach, indicating the total thickness, period, and the structure's shape.

4.3 Conclusion

In summary, this chapter presents a modeling approach for reconstructing the profile of a silicon grating layer using grazing incident small-angle X-ray scattering (GISAXS) and a dynamical theory (DT) model. In this model, we applied a thin-slicing strategy for the fitting process by dividing the periodic layer into three slices. This model can be improved by dividing the profile into more layers or slices will further increase the accuracy of the fitted profiles. Using the the proposed optimization algorithm based on CMA-ES, which

automatically adjusting the structural parameters of the modeled profiles, we achieved the fit between the experimental results and DT calculations, allowing the profile reconstruction of a layered nanostructured grating. The proposed approach designated in this study can be utilized to other periodic structures such as layered surfaces, by considering an adequate thin slicing approach to describe the details of the measured profile. For instance, it can also be used for the characterization of soft matter-based structures within the confinement of the grating channels or for the study of membrane-protein interaction where a periodic patterned surface is used as a scaffold for lipid deposition (See following chapters).

Chapter 5

Polymer brush conformations in nanofluidic channels

This chapter contains material from a manuscript in preparation. Title: "Characterization of Stimuli-Responsive Polymer Brushes in Nanofluidic Channels". Authors: Hadi Rahmaninejad, Andrew J. Parnell, Thomas Sexton, Gary Dunderdale, Wei-Liang Chen, John F. Ankner, Wim Bras, Christopher K. Ober, Anthony J. Ryan, and Rana Ashkar.

5.1 Overview

Nanofluidics with controllable gating properties have promising and exciting uses in many research areas requiring regulated fluid flow and particle selectivity, such as fluidic diodes [110], drug delivery [111], cell identification [112], DNA analysis [113, 114, 115, 116], water purification [117], and molecular sorting [118]. Various designs have been proposed and examined for the controlled gating behavior in nanochannels, such as the use of surface charge or using a field-effect to enable direct ionic manipulation in nanochannels that are dimensionally comparable to the Debye length [119, 120, 121]. However, physical manipulation of nanochannels poses a difficult challenge for easy control over nanofluidic devices with tunable or responsive properties. Fortunately, advances in nanochannel functionalization with stimuli-responsive polymers adequately address these challenges and enable new opportun-

ities for advanced applications requiring flow regulation on the nanocale[122, 123, 124].

Due to their conformational response to thermal, chemical, or optical variations in their immediate environment, stimuli responsive polymers have emerged as a versatile means for designing smart, functional surfaces. The ability to tune surface properties such as adhesion, roughness, wettability[125], reactivity, and selectivity has facilitated novel designs of mass transport-controlled devices[126, 127, 128] as well as sensing and actuation [129, 130]. Recently, they have also attracted significant attention due to their potential in biotechnology and biomedical applications. Although the most well-studied and easily triggered stimulus is temperature[131], polymers respond to other stimuli. This is particularly true for polyelectrolyte polymers where pH and ionic strength, are used for different applications such as; drug delivery [132, 133, 134, 135], separation processes[136], tissue engineering [137], and biosensors or actuators [125]. Poly (dimethyl aminoethyl methacrylate) (PDMAEMA) is a pH-responsive polymer whose conformation changes with the degree of protonation. Its amine pendant groups (basic groups)[138] are protonated in acidic environments, resulting in a swelling of the polymer due to the osmotic effect of counterions. They are highly protonated in an acidic medium such as endosomal environments, which make them widely applicable in gene delivery [139, 140, 141]. More importantly, PDMAEMA brushes show sharp and reversible switching behavior between the swollen and collapsed state [142], which is pertinent for nanofluidic purposes [143]. To examine this possibility, we employed selective functionalization on the sidewalls of sub-micron silicon channels with PDMAEMA brushes and tested the resultant channel geometry under different solution conditions.

Synthesis of the samples was performed in Prof. Chris Ober's Lab at Cornell University and in Prof. Anthony Ryan's Lab at the University of Sheffield. Specifically, we explored the degree of brush swelling and collapse in response to variations in the solution pH and salt concentration. The effect of brush conformation change on the effective width of the

channels has significant implications in controlled gating behavior and nanoparticle sorting applications. A full 3D characterization of the brush-decorated channels was obtained using specular and off-specular neutron reflectometry (NR). The measurements were performed on a series of periodic linear channels. This multi-channel geometry is necessary for signal amplification and subsequent data analysis. All measurements were performed in a fluid cell that was custom-designed for neutron reflectometry studies [144]. Taking advantage of neutron isotope sensitivity and corresponding differences in the scattering potential between hydrogen-rich and deuterium rich moieties, all measurements were performed in D_2O solutions with the desired pH level or salt content. This solvent deuteration scheme yielded the highest achievable contrast between the polymer brushes and their aqueous environment. Notably, the scattering geometry and collected data in our NR measurements significantly differ from specular reflectometry studies on polymer brushes grafted onto flat surfaces [142, 145, 146].

In this chapter, we will use the developed DT model proposed in previous chapters to extract information on the response of the brushes to changes in solution pH and charge. Here, we performed simultaneous fitting of specular and off-specular signals, yielding unique fits of the 3D structure of the polymer brushes within the channels. The data fits, performed using similar computational optimization protocol in chapter 4, indicate that the polymer chains assume a collapsed state under basic pH conditions, resulting in an open gate structure. However, upon decreasing the solution pH, the brushes swell and decrease the gate width to 100 nm. With increasing salt concentration, the brushes swell further and yield a gate width of sub-100 nm. Interestingly, in the swollen brush state, our model indicates a dense polymer brush region near the channel walls and a less dense region toward the middle of the channels, in agreement with studies of polymer brushes on flat substrates [138, 142, 147, 148].

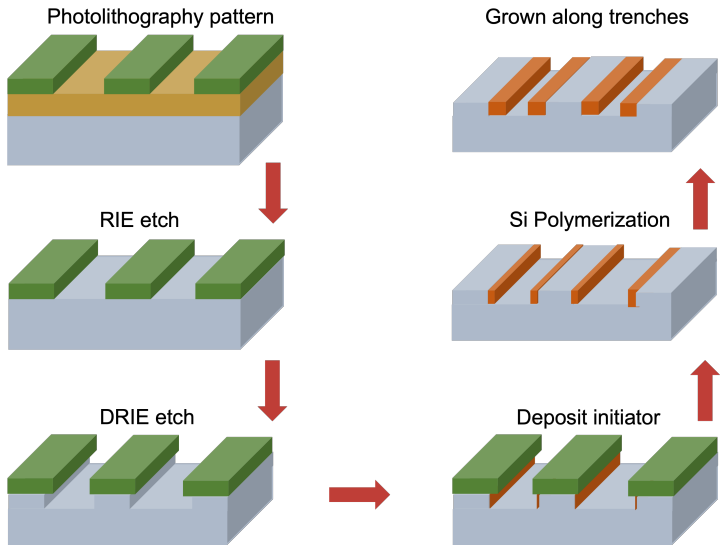

Figure 5.1: Various steps in preparation procedure, including photolithography patterns, reactive-ion etching (RIE), deep reactive-ion etching (DRIE), initiator depositing, Si polymerization, and grown along trenches.

5.2 Materials and Methods

5.2.1 Sample preparation

The samples were prepared at Prof. Christopher Ober's lab at Cornell University using grafting-from methods, in which polymerization is initiated using initiator on the sidewalls of sub-micron channels etched into a silicon wafer. By depositing a thin chromium layer on the top and bottom of the channels, the brush growth was constrained to the sidewalls of the channels (see Figure 5.1.)

5.2.2 Neutron reflectometry measurements.

Neutron reflectometry experiments were carried out at the liquid reflectometer (BL-4B) at the Spallation Neutron Source (SNS) at Oak Ridge National Laboratory by Prof. Ashkar,

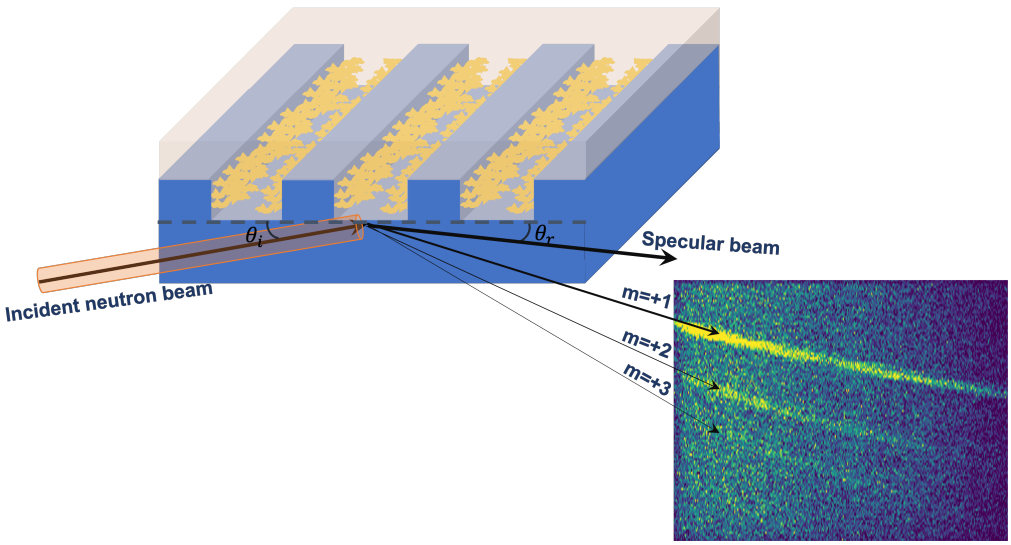

Figure 5.2: Neutron reflectometry experimental setup, showing the specular and off-specular reflection, with the first Bragg rod having the strongest intensity variation. Neutron beam is incident from silicon, with an angle of θ_i, equal to the reflected angle of specular signal, θ_r. Right panel visualizes real experimental data. The detector image was obtained at the Liquid Reflectometer beamline (BL-4B) at the Spallation Neutron Source at Oak Ridge National Laboratory (unpublished data, courtesy of A. Ryan, J. Ankner, and R. Ashkar).

Prof. Anthony Ryan, and two other members of his group. The measurements were done in two scattering geometries: specular reflection and off-specular reflection. Specular data were collected using standard beam apertures and slit sizes to cover a specular reflectometry signal over a Q-range of $2\times10^{-3}\,\mathrm{nm}^{-1}$ to $2\times10^{-3}\,\mathrm{nm}^{-1}$. In off-specular measurements, the detector was offset by 4 degrees and the specular beam was masked to enable long acquisition times of the Bragg rods which are typically several orders of magnitude weaker than the specularly reflected beam. All measurements were performed in a silicon fluid cell with a quartz window that was specifically designed for neutron reflectometry measurements. Details of the cell design can be found in previous literature [144]. All studies were performed in a D_2O buffer with the target pH and salt content.

5.2.3 Data Analysis

Specular data analysis.

Specular neutron reflectivity data were initially analyzed using Motofit package [57] to determine the thickness, roughness, and average SLD of the different layers within the sample. The obtained parameters were later used as inputs for the dynamical theory (DT) model calculations in simultaneous fitting of the specular and off-sepcular signals. Since the measurements were done such that the neutron beam was incident from the silicon substrate, the data were modeled with a front layer representing the silicon substrate (SLD = 2.07×10^{-4} nm^{-2}) and a back layer representing the solvent. To model the channel structure, three or four additional layers were considered as shown in Figure 5.3.

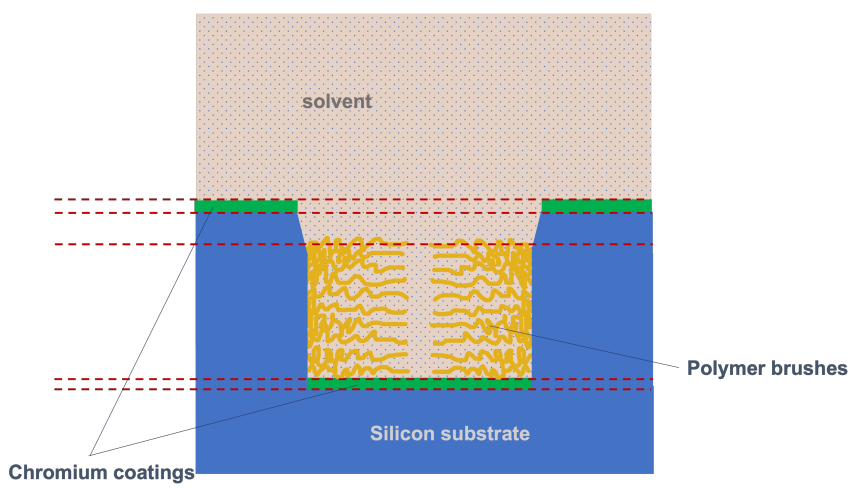

Figure 5.3: Schematic of the sample with different elements, including periodic channels etched into a silicon substrate, chromium coatings, solvent, and polymer brushes. Dashed lines represent layers considered for the specular analysis.

The model comprised of a layer containing silica and chromium at the bottom of the channel, a layer corresponding to silicon and a mixture of brush and the solvent, and another layer of trapezoidal silicon with different filling factor and solvent on the top. In the case of four layers, the additional layer represents a thin layer of solvent and chromium film deposited

on the sample surface to prevent brush growth from the top surface (see Figure 5.3 for more details). The data fits showed a better quality fit with the four-layer model, as evident from the fit residuals ($\chi^2 = 0.0197771$ for the 3-layer model vs $\chi^2 = 0.018743$ for the 4-layer model). A comparison of the fits to specular signal between three-layer model and four-layer model is demonstrated in Figure 5.4 (a) and (b), respectively. This figure also shows the SLD profile normal to the surface in panel (c). Also, the AFM image of the relevant sample can be seen in panel (d), approximately showing similar thickness of the sample.

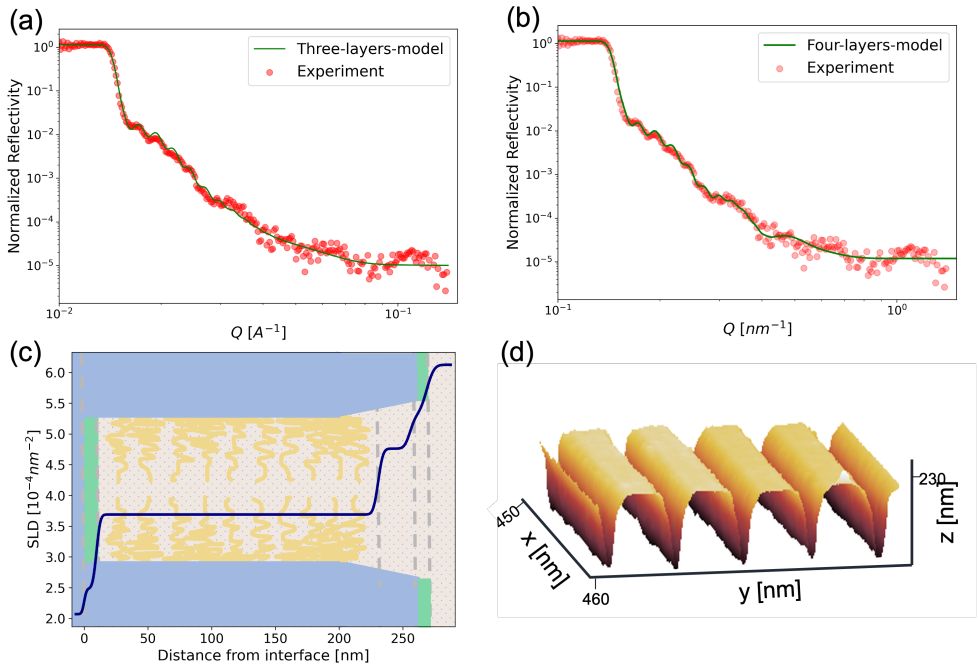

Figure 5.4: Specular reflection fits for pH 10 sample, based on (a) three- and (b) four-layer model using the Motofit fitting package. c) Averaged neutron SLD profile normal to the surface based on the fits to the specular data using a 4-layer model. d) AFM image of the wet sample, showing the total thickness and periodicity of the submicron multi-channel structure.

5.2.4 Off-specular data analysis.

The lateral characteristics of the channels and the polymer brush, e.g. channel width and brush thickness, cannot be resolved from laterally averaged specular reflectometry data but can be obtained from the off-specular signals. Based on earlier work [31], the intensity variation of the offspecular signals as a function of neutron wavelength embeds unique information of the lateral structures and SLD profile of the sample. These signals are analyzed using the dynamical theory (DT) model that has been effectively utilized in previous studies [30, 149, 150] of periodic channel structures. The details of the data reduction are described in the following section and are demonstrated graphically in figure 5.5. The data fitting was also performed using an optimization protocol described in the previous chapter.

5.2.5 Data reduction for Off-specular signals

The top left panel in Figure 5.5 is an example of a detector image obtained from off-specular NR measurements. Data reduction of such signals requires background subtractions which cannot be performed using specular NR protocols available at neutron reflectometers. Instead, we performed data reduction of the off-specular signals using image processing of detector images. This entailed choosing a band around the Bragg rod of interest (in this case the 1st Bragg rod) and finding the background intensity as a function of neutron wavelength or time-of-flight. This was done by binning the data in neutron wavelength and modeling the neutron intensity along each bin. Fits of the intensity to a normal distribution (panel c), enabled calculations of the average background intensity along each wavelength bin. The off-specular signal was then obtained by subtracting the background intensity from the total intensity for each wavelength.

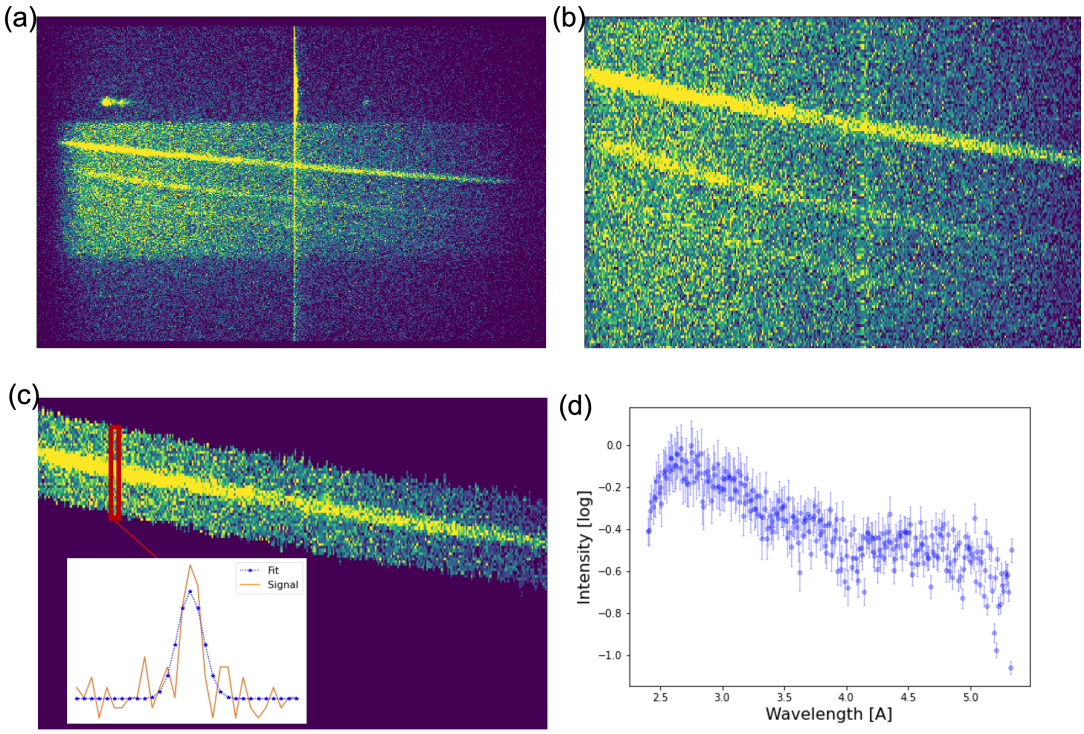

Figure 5.5: Data processing for off-specular signals. (a) A typical image showing the first few Bragg rods in a time-of-flight experiment. (b) A zoomed-in version of the detector image shown in panel a. c) Depiction of the band chosen around the first Bragg rod. The inset shows a fit of the intensity along the highlighted wavelength bin to a normal distribution function, enabling calculations of the background intensity and subsequent background subtraction. d) 1D representation of the background-subtracted off-specular signal, depicted as intensity vs. wavelength.

5.2.6 Optimization protocol.

Simultaneous fits of the DT model to the specular and off-specular neutron data were performed using an optimization protocol that fits key variables of the sample profile, including brush thicknesses and SLDs. The starting values of certain parameters (e.g. channel depth and width) and their range were set to their experimentally observed values by other methods including AFM measurements. Other parameters, such as the interfacial roughness, were input from analysis of the specular signals by Motofit. In addition, we considered two regions of the polymer brushes away from the channel sidewalls. This was inspired by earlier studies

showing different conformational states of polymer brushes away from interfaces [145]. In such cases, one would expect that two regions would have different brush density and would subsequently exhibit differences in the SLD of the respective brush brush region. The fit optimization was done using the the same protocol explained in previous chpater based on the CMA-ES package in python[32]. We defined a weighted total χ^2 from specular and off-specular data fits as fitness function (f) to show the goodness of the fit to the theoretical prediction.

5.3 Results and discussion

5.3.1 In-depth channel geometry.

A series of NR measurements were conducted under various solution conditions, including different pH 4 (swollen) and pH 10 (collapsed) and salt concentrations (10, 100 and 1000 mM). In neutron reflectometry measurements, the scattering power of materials is determined by their Scattering Length Density (SLD), which is analogous to the optical refractive index for electromagnetic waves. Fits to the specular NR data enabled sub-nm characterization of the channel geometry normal to the free surface such as the total channel thickness and the fraction of polymer brush decorating the channel walls. In these fits, the sample is divided into contrasting layers and the thickness and neutron contrast or SLD of each layer are used as fitting parameters. The layer composition is then indirectly inferred from the SLD of the layer, using the previously known SLD of the individual components. Yet, the exact analysis of in-depth variables by specular reflectometry requires complementary measurement as the specular analysis requires phase information, and with the lack of phase information, various SLD profiles may lead to the same specular reflection pattern [151]. Moreover, to solve for

the brush structure inside the channel, we require access to the sample's lateral structure, which is not provided by specular analysis. In fact, that the laterally averaged SLD is independent of the brush thickness and depends on the total volume fraction of the monomers inside the channel.

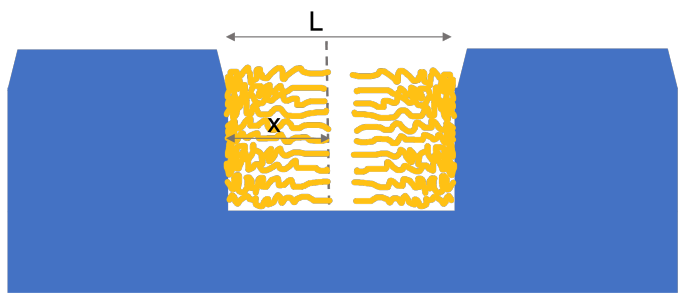

Figure 5.6: A schematic profile of polymer brushes grafted onto the sidewalls of a nanochannel, with a brush thickness x and an overall channel width L.

This can be shown by calculating the average SLD for a brush region within the channels as:

$$\begin{aligned}\rho_{av} &= f * \rho_{Si} + (1-f) * (x(\phi * \rho_{pol} + (1-\phi)\rho_D) + (L-x)\rho_s) \\ &= f * \rho_{Si} + (1-f)(x\phi\rho_p + \rho_s(x(1-\phi) + (L-x))) \\ &= f * \rho_{Si} + (1-f)(c\rho_p + \rho_D(x-c) + (L-x)\rho_D) \\ &= f * \rho_{Si} + (1-f)(c\rho_p + \rho_D(L-c))\end{aligned} \tag{5.1}$$

where f is the filling factor of the gratings, ρ_{Si} is the scattering length density of silicon, x, and ρ_{pol} are the average lengths and SLD of brush polymers, respectively (also see figure 5.6.) This relation shows that the average scattering length density is independent of the length of the polymer brushes.

Hence, off-specular measurements were performed along with specular reflectometry on the sample to provide precise in-depth measurements in a physically consistent environment. In Table 5.1, the channel thickness obtained from the fits is $\approx$ 268 nm, which is in agreement

Sample	Total thickness[nm]	$\rho_b[10^{-4}\,\mathrm{nm}^{-2}]$	Tk_b[nm]	f_m [%]	$\rho_{sol}[10^{-4}\,\mathrm{nm}^{-2}]$
PH 10	259.79	3.240	219.19	28.6	6.10
PH 4	265.8	3.241	218.83	29.1	6.00
PH 4, 10mM	266.67	3.297	220.50	28.6	5.93
PH 4, 100mM	266.78	3.222	219.72	32.1	5.97
PH 4, 1M	264.71	3.172	218.04	31.95	5.843

Table 5.1: In-depth variables obtained from the specular reflectivity data analysis. Here, ρ_b and Tk_b respectively indicate the SLD and thickness of the layer describing the brush-decorated part of the channel. f_m is the volume fraction of polymer inside the channel and ρ_{sol} indicates the SLD of the deuterated solvent.

with atomic force microscopy (AFM) measurements (See Figure 5.4.) Furthermore, the thickness of the layer containing polymer brushes is also obtained, showing a close range of 218-221 nm, indicating the length of grafted area. Another important feature of the specular signals is the critical edge, indicating a sharp drop of specular intensity (from unity). The wavevector transfer, Q, of the critical edge is given by the SLD difference between the incident medium (silicon) and the reflecting medium (deuterated solvent) such that $|Q| = 2\sqrt{4\pi\Delta\rho}$. Knowing the SLD of silicon ($\rho_{si} = 2.07 \times 10^{-4}\,\mathrm{nm}^{-2}$), the critical edge in individual data sets was used to calculate the exact SLD of the solution under each of the conditions studied here. By having the SLD of the bulk solution and the average SLD of the layer containing brushes, the total volume fraction of the polymer inside the channel is calculated (see the table 5.1 for the obtained parameters), which confirms a close range, especially for pH10, pH4, and low salt concentration ($\approx 29\%$). However, the range by adding salt increases to $\approx 31.95\%$ for 1000 mM, which we speculate to be due to the gradient of salt concentration present inside the brush domain and the bulk due to the absorption of ions by basic groups, which we did not consider in our calculations. This is also crucial later for the determination of the brush SLD and subsequent calculation of the brush volume fraction as a function of distance from the channel walls.

5.3.2 Brush Conformation.

Simultaneous fits to specular and off-specular signals yielded the 3-dimensional conformation of brushes inside the channel (See figure 5.7.) These analysis provided a detailed description of the channel's lateral scattering length density, or in other words, the Fourier coefficients of the SLD shown in Figure 5.7(d). The channel's lateral SLD represents the composition of each considered layer. In particular, it determines DMAEMA volume fraction in various brush compartments.

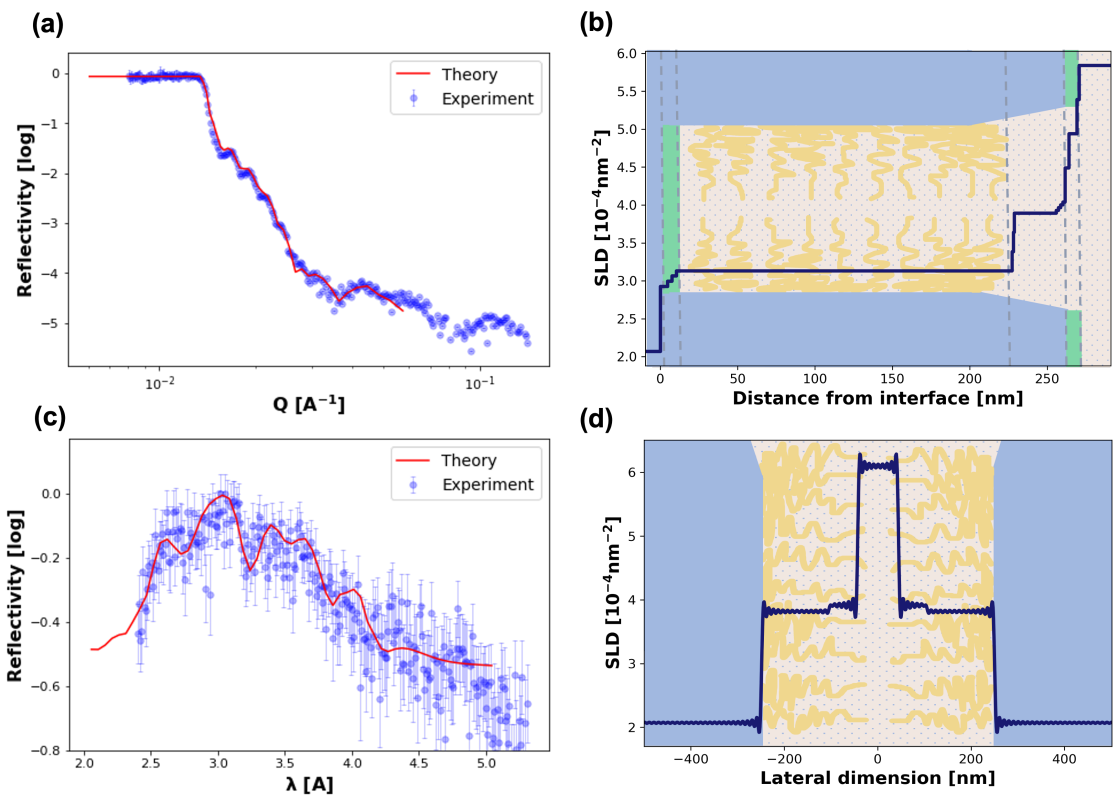

Figure 5.7: Simultaneus fits of the specular and off-specular signals for pH 4, 1M salt concentration (a) Specular, fits (b) Average neutron SLD profile obtained as a function of channel depth. (c) Off-specular fits, (d) Lateral SLD profile of the channel layer containing the polymer brushes. The middle SLD with the highest value at the center of the channel represents the gate between the polymer brushes on the opposite sidewalls of the channel. The two adjacent plateaus represent regions with different volume fractions of the polymer brush, indicating a dense region near the sidewalls and a dilute region away from that.

Theoretical studies predicted a Gaussian density profile for the "electrolyte" regime and a parabolic density profile for the "quasineutral" regime for many monomers in chains grafted into a solid surface. The former density profile is contributed by a term responsible for the counterion entropy, while in the latter case, the swelling is contributed by the repulsive volume interchain interactions [152]. Such behavior of the brushes has been observed in previous empirical studies [138, 142, 145], indicating nearly constant polymer volume fraction for thin films but variable distribution for thicker brushes, with a higher density close to the surface and lower density away from the surface. While such behavior is partially due to polydispersity, this happens mainly because brush polymers have different conformations in the outer region of the brush layer. Moreover, the construction of the hydrophobic domain potentially due to globule formation can result in averagely denser regions close to the surface [147]. Although for free chains, such formations can be situated anywhere on the backbone, for grafted brushes, they form favorably close to the solid surface to allow a gain in the interfacial energy [153]. A thin layer with the thickness of T_s can also be constructed close to the channels' side wall surfaces, where the brushes are initiated with a high volume fraction of the monomers due to the attractive interaction between initiators and DMAEMA segments [145, 148]. Consequently, we considered the brush as having regions of different scattering length density, directly relating to the brush polymer volume fraction, to account for the dense layer and the Gaussian part, which changes from the surface into the liquid phase. We found the thickness of the dense layer $T_s \approx 9 - 12$ nm for all measurements, suggesting that variation in the solution condition mostly influences the Gaussian part of the brush. This implies that the attractive interaction between the monomers and the surface is overwhelming in comparison with the swelling effect due to the osmotic pressure of the counterions. We approximated the Gaussian part with a lower sld for the region closer to the surface and a higher sld far from the surface. Considering $\rho_{Sol} \approx 6.10 \times 10^{-4}\,\mathrm{nm}^{-2}$ and $\rho_{DMAEMA} = 0.80 \times 10^{-4}\,\mathrm{nm}^{-2}$ [145], these measurement shows the higher

volume fraction of DMAEMA near the sidewalls and a dilute domain for brushes far from the surface, particularly for less stretched chains. Notably, the computed SLD profile determines the gate opening width of the channel. This opening width is obtained by determining a region at the middle of the channel between brush ends from the opposite sides, which has the highest SLD($\approx 6.10 \times 10^{-4}\,\mathrm{nm}^{-2}$) representing the solvent region. This indicates that our analysis provides a non-invasive method to characterize the gate opening in this model nanodfluidic channel, which can be measured under various solution conditions to explore its response to surrounding solvent changes (pH, ionic strength, solvent etc.).

5.3.3 Effect of pH on gate opening.

For pH-variation experiments, measurement were run at basic (pH 10) and acidic (pH 4) solvents, above and below pk_a, respectively, to explore the channel gate response to the solution condition, as a result of conformational change of PDMAEMA brushes. In general, depending on the grafting densities, the polymer brush chains undergo excluded volume repulsion and have a strongly stretched conformation in comparison with isolated polymer chains [154]. The scaling law of neutral brush as a function of their grafting density was described by Alexander [155] and de Gennes [156] as $L \propto N\sigma^{1/3}$. When polymer chains contain charged monomers, i.e., polyelectrolytes, the scaling law is fundamentally different; as in this case electrostatic interactions and their subsequent impact on counterion absorption should be considered, leading to osmotic pressure of confined counterion within the brush. As a result, their scaling behavior is determined by the contribution of repulsive interchain interaction and also the counterion osmotic stretching force. The ”strong” polyelectrolyte brushes are “quenched,” the charging degree of the grafted chains is fixed, and the solution condition does not change the number of charges on the chain. On the other hand, for “weak” polyelectrolytes, the degree of ionization can be adjusted by the variation of the

solution condition, mainly pH level and ionic strength [157]. The excluded volume contribution increases by grafting density, while the osmotic stretching force due to counterions is independent of that. As a result, the response of the polyelectrolyte brush to the solution condition is more prominent in low-density brushes [145].

The swollen thickness of PDMAEMA when they act as polyelectrolyte brush in aqueous solutions is more significant than the case for when they act as neutral polymer brush in organic solvents, owing to a higher osmotic pressure of the counterions within the polyelectrolyte brush in comparison with the osmotic pressure of monomers [142]. The PDMAEMA brush contains dimethylamino groups which determine the charge of the grafted chains by the level of association or dissociation of protons at various pH values [158, 159, 160]. At pH levels below their pk_a (≈ 6), they have a swollen conformation, where the amino groups are protonated, leading to the high osmotic pressure of the counterions entrapped in the brush domain [138]. However, at a pH amount above their pk_a, the amino groups are deprotonated, collapsing the brush. Figure 5.8 shows the simultaneous fits for the system in the solution with pH 10 and pH 4, along with lateral SLD obtained for the channel layer. Figure 5.9 shows the result of our measurements by presenting the brush height in the dense and dilute regions and the resultant gate opening. In these measurements, the total brush thickness at pH 10 was found to be ≈ 151 nm, where the dense brush region was obtained ≈ 111.63 nm and the low-density region is ≈ 40 nm. In comparison, at pH 4, the total brush thickness was found to be ≈ 174 nm, as in this case, the amino groups are protonated, and the brush is swollen because of the osmotic effect of counterions. The dense and dilute brush region in this case was ≈ 105 nm and ≈ 69 nm, respectively, showing an increase for both regions. Similar swelling behavior of PDMAEMA brushes on flat substrates was reported by other studies using neutron reflectivity [142, 145, 147].

Considering this change in their thickness from the opposite sidewalls, this results in ≈ 46 nm

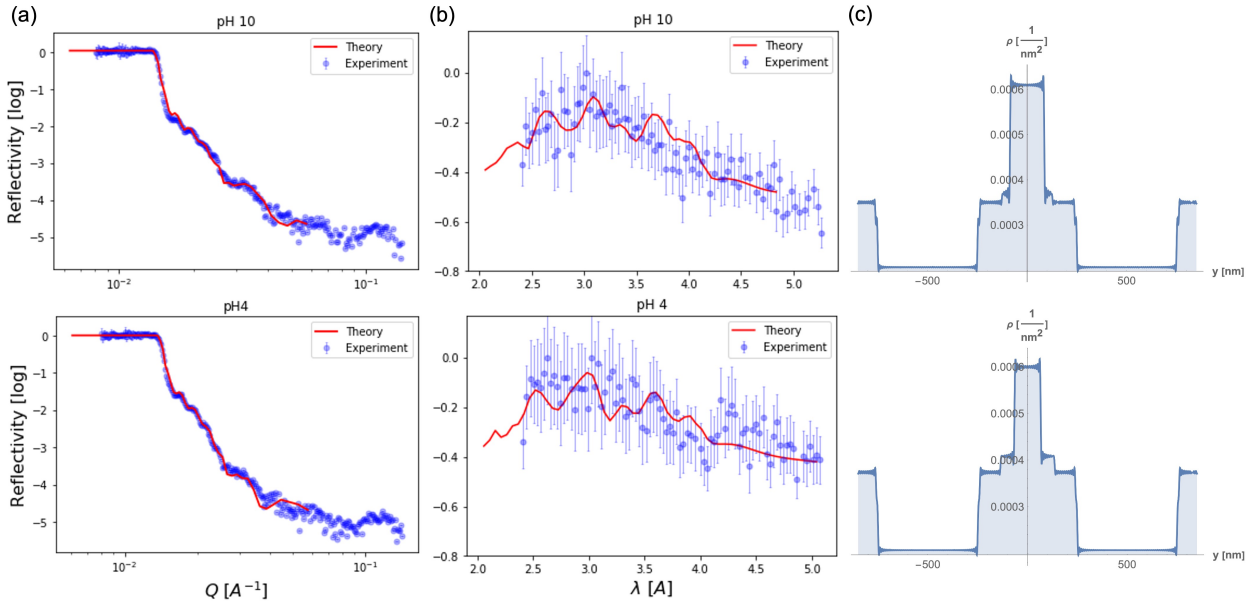

Figure 5.8: Simultaneous fits of specular and off-specular signals for pH 4 and pH 10, a) Specular fits, b) Off-specular fits, and c) SLD profile of the channel layer containing the polymer brushes. The plot shows a single channel (or unit cell) where $y = 0$ is set in the middle of the channel. The middle SLD with the highest value at the center of the channel represents the solvent region (SLD $\approx 6\times10^{-4}\,\mathrm{nm}^{-2}$) or the gate between the polymer brushes on the opposite sidewalls of the channel. The two adjacent plateaus represent regions with different volume fractions of the polymer brush, indicating a dense region near the sidewalls and a less dense region away from the sidewall.

reduction of the opening width in the channel, which changes it from $\approx 196\,\mathrm{nm}$ to $\approx 150\,\mathrm{nm}$; switching from an open gate to a partially closed state. The dependence of opening width on the pH level can be modified by controlling grafting density, as the swelling rate highly depends on the grafting density. Mainly, at high grafting density, the osmotic pressure of the segments overcomes that of the counterions, and consequently, the swelling rate is less dependent on the pH variation. The sharp and reversible switching behavior of PDMAEMA brushes between initial, swollen, and collapsed states are reported by *in situ* measurements [138]. Moreover, experiments on the kinetic behavior of a similar weakly polybase polymer brushes, poly(2-(diethylamino)ethyl methacrylate)(PDEA), indicate highly reproducible changes between swelling and collapse states over several pH cycles along with equilibrium

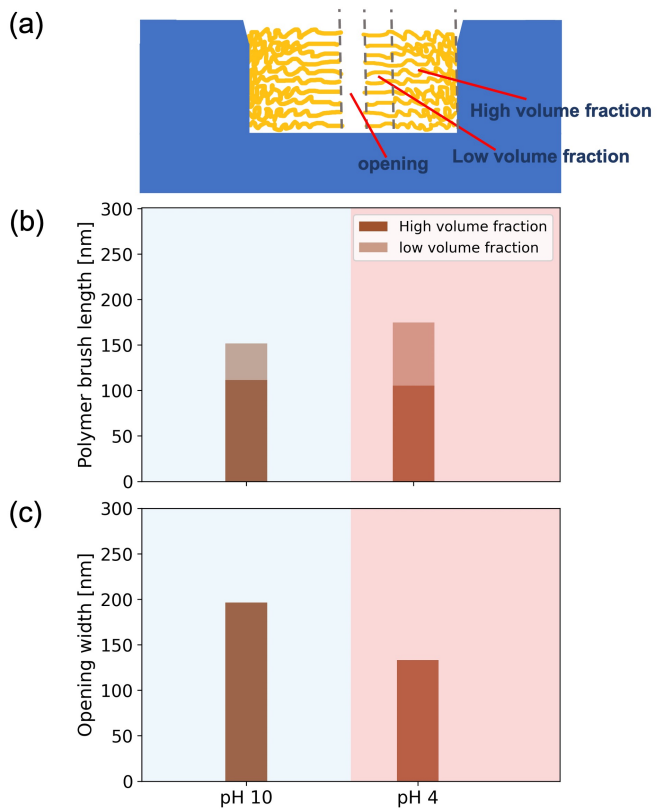

Figure 5.9: Brush response to variation in solution pH. a) Schematic of a nanofluidic channel showing the high and low volume fraction regions of the polymer brush, and the total layer thickness. b) Influence of pH level on high and low volume fraction lengths. c) The effect of pH level on the nanofluidic channel opening.

brush behavior, although with an asymmetric rate between swelling and collapse process with a faster pace in the former route [161]. Such robust dynamic switching behavior of weak polybasic brushes implements the active control of the gate opening by regulating the solution's pH condition with the precision of a few tens of nanometers (the size of supra-molecular structures), which motivates the nanofluidic controllable gating applications.

5.3.4 Effect of ionic strength on gate opening.

Along with pH, ionic strength variation is adopted to be another strategy to modify the properties of the surfaces functionalized with weak polyelectrolyte brushes by controlling the electrostatic interactions. Previous studies show that the wet thickness is mainly influenced by salt concentration at lower pH amounts, as at low pH the grafted PDMAEMA brushes are highly charged, and the electrostatic interactions can be modified by the salt concentration variations leading to the regulation of osmotic pressure of counterion within the brushes [158, 162, 163, 164]. Consequently, we assessed the effect of ionic strength on the brush structure at pH 4 (below the pK_a), i.e., a fully extended brush, for 10, 100, and 1000 mM salt concentrations. The ionic strength strongly influences the electrostatic interactions in the brush region by regulating the electrostatic screening length and adjusting the number of charged monomer groups in the brush layer [165]. The response of the brush thickness to the ionic strength highly depends on the grafting density, and charge fraction of the chain [166]. Theoretical studies by Zhulina et al., based on mean field theory predict that in a polyelectrolyte regime where electrostatic interaction is more dominant compared to volume interchain interaction, the scaling behavior is nonmonotonic [167]. Mainly, in the "osmotic" regime, when the salt concentration in bulk solution is smaller than that of the counterion inside the brush, layer thickness follow $L \propto c_s^{1/3}$. On the opposite limit, in "salted" brush regime, salt ion charge dominate immobilized charges inside the brush, and brush thickness follow $L \propto c_s^{-1/3}$. Similar behavior of the chain is reported by Fleer based on numerical self-consistent field model (SCF) [168]. Such chain behavior is obtained when the excluded volume effect is weak, more specifically, when $w^{1/2}\sigma a^2 m \ll 1$ where w is the third virial coefficient, σ is the grafting density, a is the size of polymer segments, and m represents the elementary charges of each chain [152]. Witte et al. used a continuum numerical SCF theory to demonstrate that such classic scaling profile applies in a very low chain density, when the

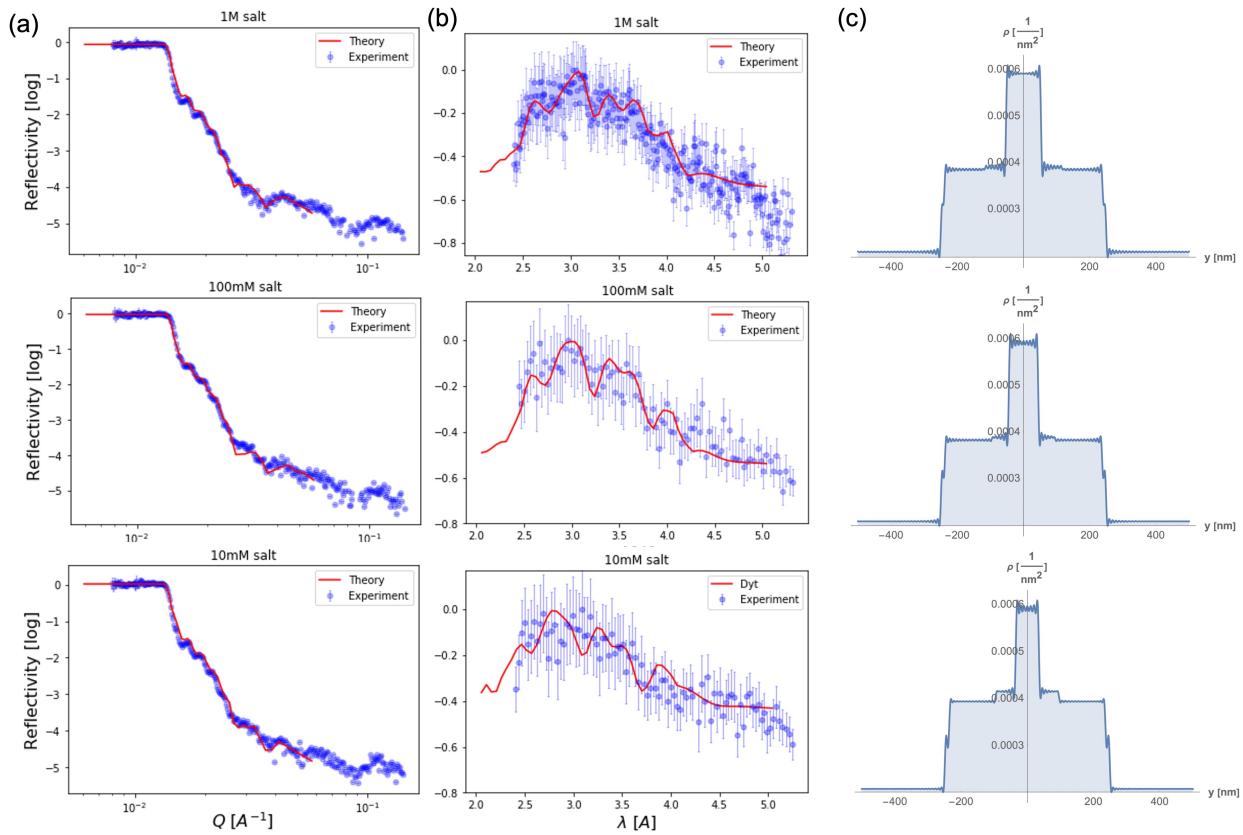

Figure 5.10: Simultaneous fits to the specular and off-specular signals for pH4 with various salt concentrations of 10, 100, and 1000 mM. a) Specular fits, b) off-specular fits, and c) SLD profile of the channel layer containing the polymer brushes.

effective segment volume is not considered [162]. Despite considering excluded volume effect, especially for dense brushes, most of the theoretical [163, 166, 167] and experimental works [157, 161, 169] qualitatively reported a similar trend; increasing the height of polyelectrolyte brushes in the low salt osmotic regime and decreasing the size in highly salted brush regime. The results are summarized in Figure 5.11a by showing the response of different regions of polymer brushes to the variation of salt concentration. An increase in the total thickness of the brushes was observed by adding salt in comparison with hypothetical zero ionic strength solution, as by adding salt, the anions take the place of hydroxide counterions within the brush and, as a result, increases the degree of dissociation which increases the os-

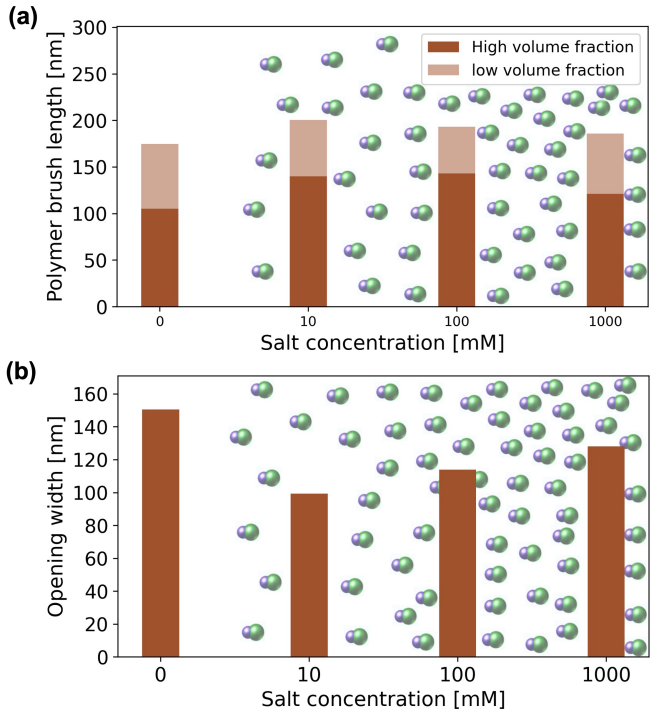

Figure 5.11: Polymer brush height changes with salt concentration. (a) Schematic of nanofluidic channel showing the high and low volume fraction region of polymer brushes. (b) Influence of salt concentration on high and low volume fraction lengths.(c) The effect of salt concentration on the nanofluidic channel opening.

motic pressure inside the brush. At high salt concentrations (100-1000mM), brush response to additional ionic strength changed, and a decrease was observed in the total thickness, but with a more moderate change compared to the low salt concentration (0-10 mM). For relatively high ionic strength, where the bulk electrolyte concentration surpasses the concentration of counterions inside the brush, any addition of salt results in the screening of the electrostatic interaction between monomer groups, which decreases the brush thickness. Further, we observe a higher thickness of the brush in the highly salted case (1000 mM) compared to the low salted case, which mimics the results reported in previous experimental works [161, 169, 170]. While our results qualitatively agreed with previous theoretical and experimental works, it doesn't precisely obey the classic scaling law showing a sharp increase

in the low salt limit (power of 1/3) and a sharp decrease in the high salt limit (power scale of -1/3). To a great extent, such behavior can be rationalized by the high grafting density ($\sigma > 0.5\,\mathrm{nm}^{-2}$) in our experiment, leading to a considerable interchain interaction effects and deviation from the "electrolyte" regime predicted by Zhulina et al. [167] Such quantitative discrepancy is also observed in previous empirical studies on weak polyelectrolytes [161], which can be also due to nontrivial three-body interactions at high grafting density, the polydispersity of the chains, and notably the polymer backbone hydrophobicity, which were not considered in the theoretical computations [171].

These results show that regulating ionic strength can control the gate width (See figure 5.11b). The increase in salt concentration from the hypothetical zero salt concentration to 100 mM leads to a $\approx 38\,\mathrm{nm}$ reduction in the channel opening. However, in the high salt concentration, the change in the opening width from 100 mM to 1000 mM was $\approx 6\,\mathrm{nm}$ due to the weaker dependency of the brush thickness at high salt concentrations. Importantly, adding a high amount of salt keeps the gate semi-closed compared to the non-salted situation. Interestingly, previous studies show that polyelectrolyte brush response to the ionic strength at pH level below pK_a is more symmetric between the swollen and the collapse, with a considerably faster collapse conversion compared to pH-induced [161]. Moreover, they showed that the ionic strength controls the pH response of weak polyelectrolytes by regulating the screening of electrostatic repulsion. Mainly, as the salt concentration increases, a higher pH level is required to trigger brush collapse. The time taken for the brush to collapse also increases in the presence of the excess electrolyte, due to a slower diffusion rate of ions from within the brush to the bulk. Overall, the ionic strength adaptation can directly and indirectly (by manipulating pH response) affect chain conformations which will motivate new mechanisms for gate control by a combination of pH and ionic strength variations to regulate the thickness and rate of the change in the brush.

In summary, this chapter described a model for nanofluidic channels with controllable gating property by grafting PDMAEMA chains to the channel sidewalls. Specular and off-specular neutron reflectivity measurements were performed to study the brush conformation and obtain a side view of the channel under different solution pH and ionic strength conditions. The results indicate that the conformational changes of the brush result in controllable channel gating, with an open gate structure in the case of collapsed brushes and a semi-closed gate structure when the brushes are in the swollen state. Currently, establishing switchable valves to actively regulate nanofluidic flow is critically challenging [172]. The switching between various gate states can be tuned by solution condition variation, particularly the pH level and the ionic strength. However, the change is highly dependent on other parameters, including the grafting density and the average charge of the chains. While reaching a high grafting density for nanofluidic applications is pertinent depending on the fluid particle sizes, this leads to a weaker response of the valve to pH and salt concentration, mainly due to the excluded volume effect. In any regard, these parameters can be potentially engineered contingent on the nano-valve applications.

Chapter 6

Effect of membrane curvature on protein binding

6.1 Overview

Cytoplasmic protein recruitment by cellular membranes plays an essential role in facilitating a diverse set of cellular functions, mainly cell signaling and membrane trafficking [173]. Proteins can associate with the membrane integrally, where they embed in the hydrophobic region of the lipid bilayer, or peripherally, where they bind with the hydrophilic surface [174]. Integral proteins that bind to the membrane include ion channels, transporters, and receptors, while peripheral proteins are enzymes, cytoskeletal proteins, and some signaling molecules. An example of an integral membrane protein is CD39 which works in conjunction with CD73 to regulate extracellular nucleotide and adenosine signaling [175]. Peripheral proteins play an essential role in the critical functions of the cells, and any disruption to their activity leads to severe disorders, such as tumor growth [176], which is why they have been recently considered therapeutic targets [177]. Hence, to discover potential therapeutic treatments, of paramount importance is to understand the mechanisms the membrane uses for protein recruitment. Various scenarios have been observed for the molecular mechanism in which peripheral membrane proteins can associate on the surface of the plasma membrane: some of them via a covalent linkage such as membrane-associated enzymes [178], another

category with attaching to the cytosolic face of the membrane by hydrocarbon moieties [174], and those which link to the membrane with their fatty acyl groups [179].

Previous studies have indicated curvature and lipid composition as the main factors driving the adhesion of many peripheral proteins by cellular organelles [180]. Membrane lipids adopt non-random distribution with substantially various compositions, even between different leaflets of organelle membranes [181], which influence peripheral protein binding either by implementing membrane defects or by inducing regions of negatively charged lipids [182]. Moreover, many processes contribute to changes in protein reconcentration which induce variation in the membrane curvature, e.g., lipid-packing defects or the exposure of hydrophobic cavities [180]. A lipid membrane is a flexible sheet of amphiphilic molecules that undergoes various shape and curvature changes [183], either by the membrane components, such as lipids or proteins, or the cytoskeleton itself [184]. In fact, it is observed that through various mechanisms, the cell membrane can achieve complex architectures required for its vital biological functions, mainly necessary protein recruitment [185, 186].

To investigate the correlation between the strength of protein binding with membrane curvature, engineered scaffolds with similar cytoskeleton mechanical properties are required, with reasonable control over local membrane curvature. An appropriate system comprises lithographically patterned silicon substrates coated with a layer of thermoresponsive polymer, such as poly(N-isopropylacrylamide) (pNIPAM) [31]. PNIPAM has a lower critical solution temperature (LCST) near the body temperature and is broadly used for biomedical applications, such as soft robotics, drug delivery, and cancer therapy [187, 188, 189]. Interestingly, the mechanical and physiochemical properties of pNIPAM are analogous to those of the cell cytoskeleton, providing a similar environment as the cellular milieus [190]. It has been previously shown that such pNIPAM coated on periodic nanostructures exhibit very different topographies below and above the transition temperature of pNIPAM, making

them an ideal scaffold for cell growth and release in tissue engineering [31]. In this study, such structures are used as topographically tunable scaffolds for lipid membrane deposition and studies of curvature-induced membrane protein interactions. At low temperatures of around 300 K, the films are in expanded states, and as a result, a low curvature is induced, while at high temperatures in 315 K, they are collapsed, and the scaffold becomes highly curved. Neutron reflectometry measurements were then employed for high and low curvature cases to investigate the structure profile with and without protein distribution and study binding strength between the membrane and proteins. In this study, crescent-shaped Bin/amphiphysin/Rvs (BAR) domain proteins are used, which are well-known to regulate cell membrane curvature [191]. Mainly, a category of them, N-BAR proteins, are characterized by an additional N-terminal amphipathic helix which is used as a tool to promote membrane curvature and dimerization. Through qualitative analysis of specular and off-specular reflectivity, we classify between various profiles to correlate the protein binding strength and membrane local curvature. We demonstrate that dynamical theory analysis can be readily applied to the study of such a complicated soft-matter-based system, particularly by utilizing the optimization protocol that we developed for structures with many number of variables.

6.2 Methods

6.2.1 Sample preparation

Polymer coating of substrates was performed in the lab of Prof. Ryan Toomey at University of South Florida. A periodic silicon substrate with a period of around 833 nm and depth of around 250 nm was coated with pNIPAM using dip coating. Atomic force microscopy

were performed in various temperatures between 300 K and 315 K by a former graduate student. These measurements show topological change of the coated layer below and above the polymer LCST [192].

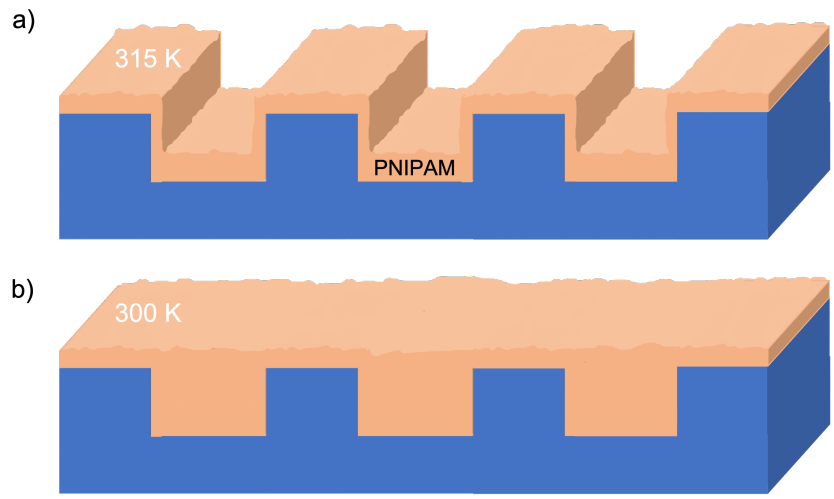

Figure 6.1: Different states of pNIPAM coated on a silicon periodically nanostructured substrate at various temperatures, a) above and b) below its transition temperature. The system is used to implement a tunable scaffold for lipid deposition.

6.2.2 Neutron reflectometry experiment

Neutron reflectometry measurements were performed by Prof. Ashkar and Dr. John Ankner at the liquid reflectometer beam line at neutron source at Oak Ridge National Laboratory. The measurements were done in specular and offspecular reflectometry modes. Specular data were collected with various incident angles to cover a Q-range of $7 \times 10^{-4}\,\mathrm{nm}^{-1}$ to $2 \times 10^{-2}\,\mathrm{nm}^{-1}$, with a precision of $\frac{dQ}{Q} = 0.023$. Similar to the measurements described in chapter 5, in off-specular mode, the specular beam was masked to enable long acquisition times of the Bragg rods, which are typically several orders of magnitude weaker than the specularly reflected beam. All measurements were performed in a silicon fluid cell with a quartz window specifically designed for neutron reflectometry measurements. Details of the

cell design can be found in the doctoral dissertation of Prof. Ashkar [144]. All studies were performed in a D_2O buffer to enhance the contrast between system and solvent.

6.2.3 Data analysis

Specular Analysis

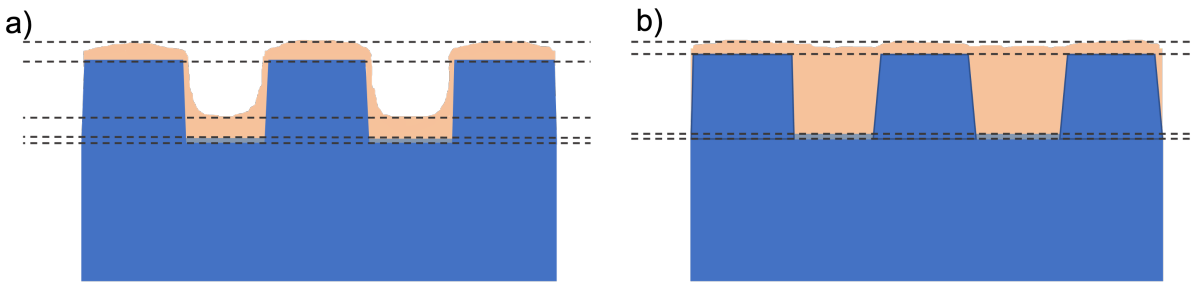

Figure 6.2: A cross-sectional view of the pNIPAM coatings on a silicon grating layer for a) collapsed state and b) expanded state. Dashed lines represent the layered model for the specular neutron reflectometry analysis. Four layers are considered for the collapsed state and three for the expanded state.

Specular neutron reflectivity data were initially analyzed using a standard package called Motofit. The data were modeled using four layers for the collapsed case, and three layers for the expanded case, representing the silicon periodic structure, a thin silica layer, and the pNIPAM coating in addition to a silicon and solvent layer (figure 6.2.) For samples with a deposited lipid membrane, as well as N-BAR proteins, additional thin layers were accounted for. The analysis provides the average SLD profile along the surface normal, yielding the thickness, roughness, and laterally averaged SLD of different layers.

Off-specular Analysis

Detector images were provided in pixel number, wavelength, intensity, and uncertainty format. Then, they were visualized by reshaping to matrices to manifest reflected intensity

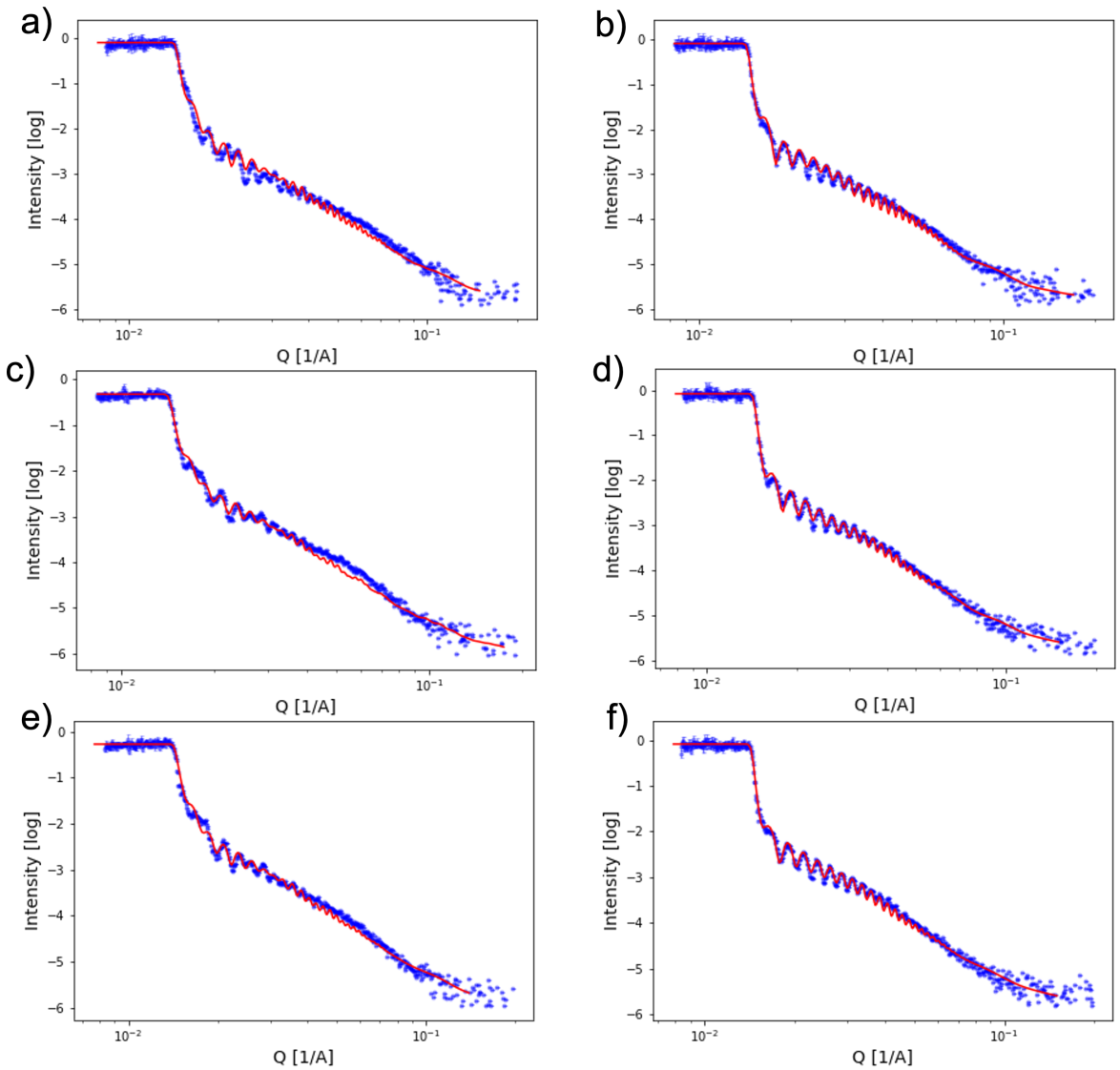

Figure 6.3: Analytical fits to the specular reflected intensities, at different temperature for a) polymer coating at 315 K, b)polymer coating at 300 K, c) DOPC deposited on polymer coating at 315 K, d) DOPC deposited on polymer coating at 300 K, e) DOPC deposited on polymer coating in presence of N-BAR proteins, and f) DOPC deposited on polymer coating in presence of N-BAR proteins.

(see figure 6.4.) To carry out further processing for extracting the Bragg rods from the detector image, we used a similar method described in chapter 5. First, the area near the Bragg rods was selected. Next, the image was binned vertically for background subtraction

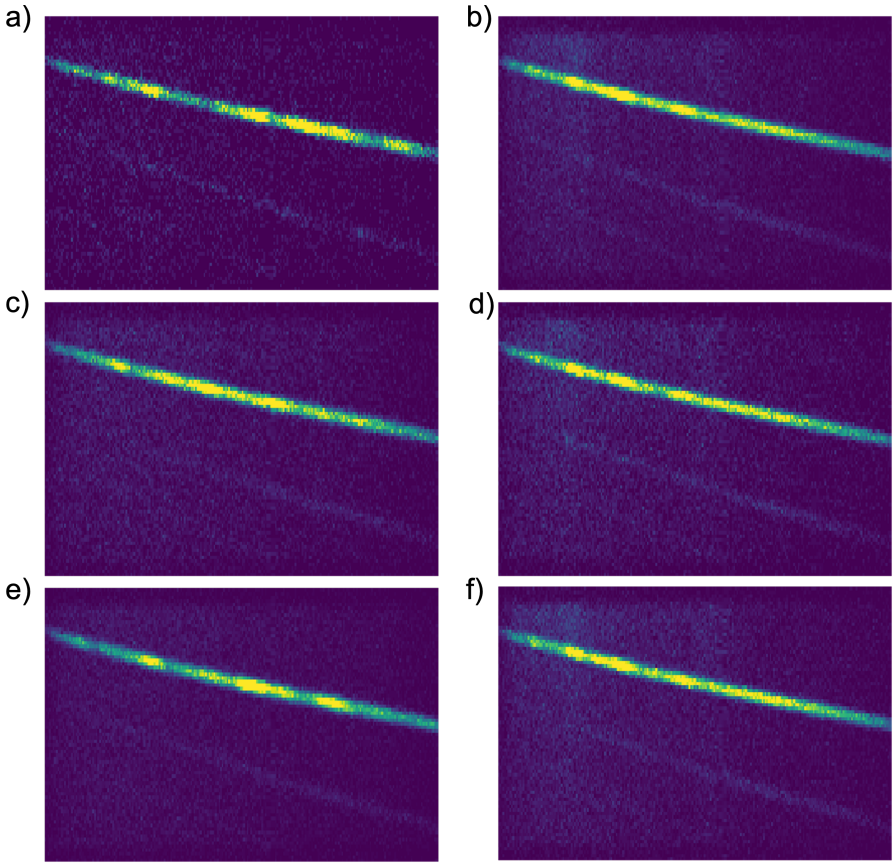

Figure 6.4: Detector images of neutron off-sepcular scattering from a)polymer coatings on substrate at 315 K, b) polymer coatings on substrate at 300 K, c) DOPC deposition on polymer coatings at 315 K, d) DOPC on polymer coatings at 300 K, e) DOPC deposition on polymer coatings with N-bar protein distribution at 315 K, and f)DOPC deposition on polymer coatings with N-BAR protein distribution. The detector images were obtained at the Liquid Reflectometer beamline (BL-4B) at the Spallation Neutron Source at Oak Ridge National Laboratory (unpublished data, courtesy of J. Ankner, M. Doucet, and R. Ashkar).

to represent intensity variation near a peak for each wavelength. Then, the intensity variation was fitted to a normal distribution, and its asymptotic tail was used as the background intensity. We then subtracted the background intensity from the sum of the pixel's intensity larger than a threshold to obtain the reflectivity of each wavelength. A similar procedure was performed for other wavelengths to convey the intensity variation as a function of the

wavelength.

6.3 Results

6.3.1 In-depth characterization

The averaged parameters normal to the surface (in-depth parameters) were predicted by fitting specular reflection, which provide thickness, roughness and the average SLD of the profile. The in-depth model considered for these analyses are illustrated in Figure 6.2. Fits to the pecular signals are demonstrated in figure 6.3.

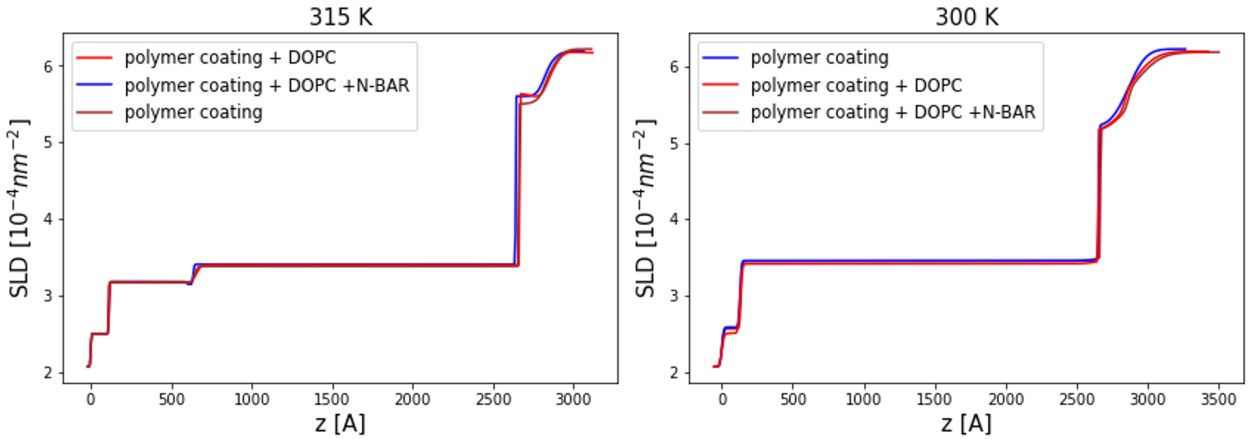

Figure 6.5: The SLD profiles of the system in various temperatures, for cases of polymer coated on the substrate, polymer coated with DOPC bilayer, and polymer coated with DOPC deposition in the presence of N-BAR proteins.

Based on these fits, the SLD profile normal to the samples in various temperatures was obtained (see figure 6.5.) In the expanded case, a similar SLD profile is observed when DOPC is deposited on the polymer, even when N-BAR proteins are distributed on the membrane. A slight difference is observed in comparison with the pNIPAM coating case, especially on top of the structure at around $z = 300\,\mathrm{nm}$, which indicates the lipid deposition

within the roughness of the top layer. Such difference is more significant in a collapsed state, where the in-depth model for specular analysis has layers accounting for the lipid bilayer on top and bottom of the channels.

6.3.2 Off-specular analysis improvement

Figure 6.5 illustrates similar in-depth SLD profiles at each temperature, with trivial differences in the interfacial roughness, especially for the top layers where lipid membrane is deposited on the polymer coatings. Such interfacial roughness represents the lateral inhomogeneities of various layers, which cancel out each other to averagely lead to similar specular signals. On the other hand, interfacial roughness is theoretically expected to influence off-specular signals considerably. This is because off-specular scattering provides depth-resolved in-plane information and contains rich evidence regarding the film's inhomogeneities and fluctuations in interfacial positions, which are commonly found in soft-matter thin films [193].

While the primary source of off-specular signals in the system in this study comes from the laterally periodic surface with a non-zero beam momentum along the period, the impact of roughness is still more noticeable in comparison with specular signals. To show this effect, we applied our model based on dynamical theory by considering interfacial roughness to the off-specular neutron reflectometry data from a very similar system, pNIPAM coated on a patterned silica substrate, previously used to study its application in tissue engineering [31]. We implemented thin sub-layers at the boundary between various layers to gradually change the overall SLD (see chapter 4 for further details.) Finally, we applied the optimization protocol described in chapter 4 as such improvement adds to the number of unknown variables. Figure 6.6 compares fits from off-specular signals with models considering interfacial rough-

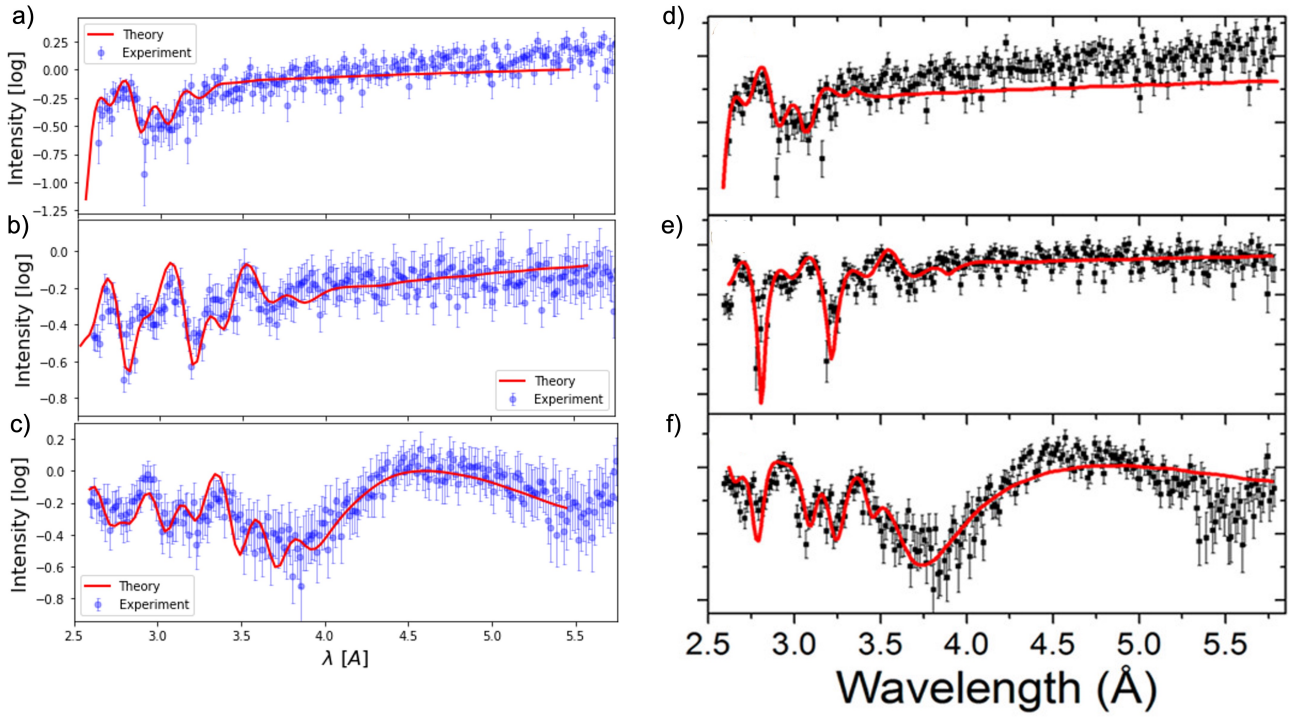

Figure 6.6: Comparison between off-specular analysis a-c) with considering interfacial roughness, d-f) without roughness, for a bare periodic structure, expanded polymer coating, and collapsed polymer coating, respectively. Panels d-f are reproduced by permission from Zhernenkov et al., ACS Appl. Mater. Interfaces 2015, 7, 22, 11857–11862 [31].

ness (panels a-c) and without taking into account the roughness, as previously reported in earlier studies [31] (panels d-f). Overall, adding roughness improves the fits for various systems. Such improvement is more significant for the system with collapsed pNIPAM, where the system undergoes more significant change laterally, as in this case polymer coating constructs a thin layer on the top and bottom of the channels and a thinner coating on the walls of the channels. Such a finding is more important for the discussion in the next section when we observe a considerable change in the scattering signals when N-BAR proteins are added to the membrane for the case of the collapsed polymer coating. Such analysis validates the improved quantitative study based on the dynamical theory model by adding interfacial roughness in polymer coated systems, and shows the potential of optimization

protocol developed for accurately interpreting reflectivity signals from complex soft-matter nanostructures.

6.3.3 Lateral structure

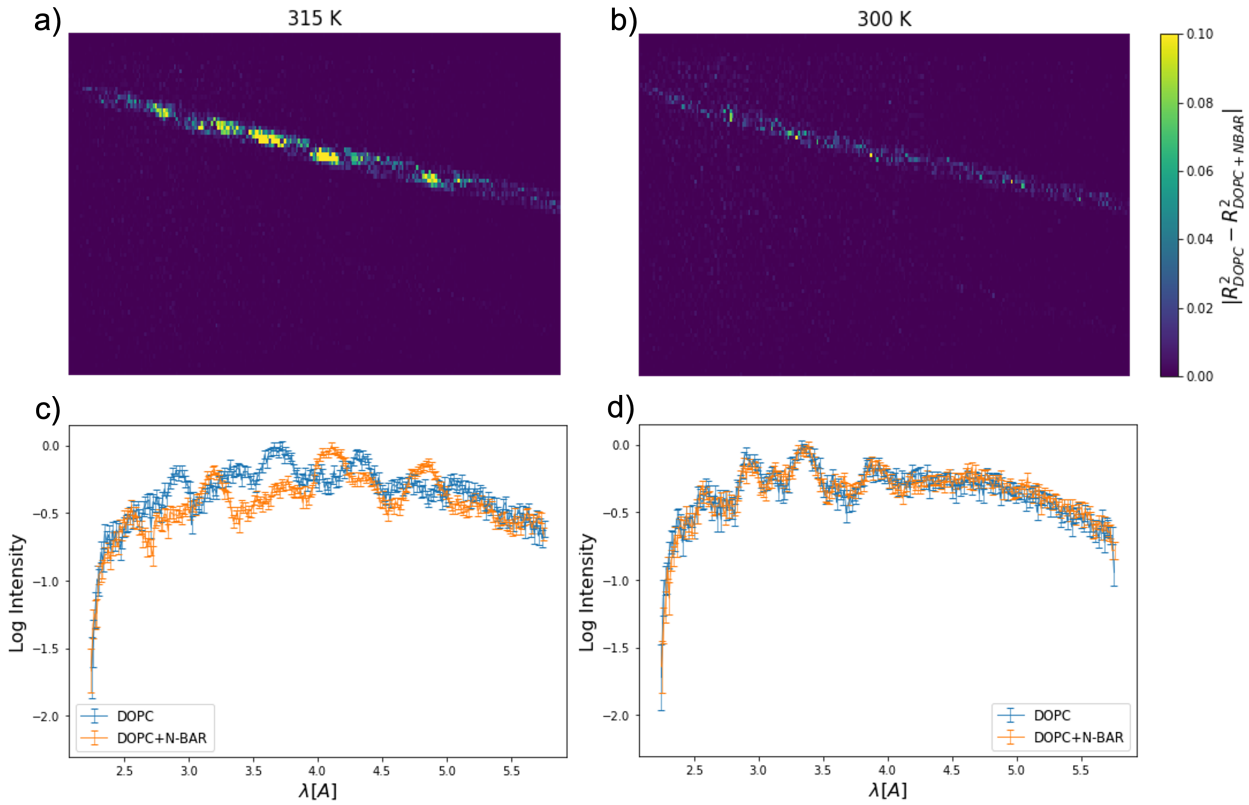

Figure 6.7: Comparison for off-specular reflected intensity for collapsed and expanded cases at 315 K and 300 K, respectively. a) Reflected intensity difference at 315 K between measurements with and without N-BAR proteins. b) Similar quantity as panel a, at 300 K. The label in the color bar, $|R^2_{DOPC} - R^2_{DOPC+NBAR}|$, indicates the normalized magnitude of the difference between reflected intensity for the cases of with, and without N-BAR proteins. c) Reflected intensity for the system with and without N-BAR proteins at 315 K, and d) Same variable indicator as panel c, at 300 K.

The lateral structure of the system can be investigated by off-specular analysis. In chapter 5, we discussed that the complete analysis of in-depth variables by specular reflectometry requires complementary measurement. This is because the specular analysis requires phase

information, and with such information, it is inevitable that various SLD profiles result in the same specular reflection pattern [151]. More importantly, off-specular signals contain significant details of the sample, and a slight change in the lateral conformation of the system can be exponentially amplified and result in a considerable alteration in the off-specular reflected intensity. This is manifested in the analysis shown in figure 6.7. This figure shows the reflected intensity for the first Bragg rod in different temperatures, 315 K and 300 K, where the conformation of pNIPAM coating is expanded and collapsed, respectively, with and without protein distribution on the membrane. Our analyses indicate that while in the highly-curved membrane the reflected intensities are distinguishable, in the expanded case, where the membrane undergoes low curvature, signals are very similar. Hence, the sample profile undergoes a considerable change upon the interaction with N-BAR proteins in the highly-curved membrane, whereas the structure is unaffected in the low-curved case. Such observation strongly implies the effect of membrane curvature on the protein binding. The interplay between lipid membrane curvature and protein sensing has been observed in previous studies [194]. Some studies report that peripheral protein association can be a driver for membrane curvature [195]. Also, some sorting proteins have curvature indicators, which, in combination with the lipid specificity domain, can precisely localize on the membrane [196]. Moreover, it is observed that the BAR domains play an essential role in sensing the curvature [197]. The finding presented in this chapter support such correlation by showing a noticeable change in the membrane behavior while interacting with N-BAR proteins under various induced local curvatures.

Chapter 7

Conclusions and outlook

Periodic nanostructures decorated with soft materials are widely applicable in nanotechnology and recently provided a framework for biological research, particularly cell membrane studies. However, the characterization of such systems requires considerable effort; a non-destructive precise three-dimensional reconstruction of such "layered" substrates is contingent upon the use of scattering methods, which are challenging due to the necessary quantum mechanical modeling. This thesis presents a computational approach based on an exact theoretical model, i.e., a dynamical theory model, for interpreting scattering patterns from soft-matter-based periodic nanostructures. We utilized an optimization protocol based on CMA-ES, which automatically adjusting the profile parameters of the structure to achieved the fit between the experimental results and theoretical calculations, allowing the profile reconstruction of a layered nanostructured surface.

In chapter 3 we reviewed the necessary theoretical bases for neutron and X-ray scattering. We reconsidered the equations and relations for the reflectometry of thin films. We then proved the relations for the dynamical theory, especially how it can be generated to a more complex layered profile by thin slicing the sample according to Parratt's formalism. Importantly, we demonstrated how models based on dynamical theory, which has been successfully applied for neutron scattering, can be generated for the case of X-ray scattering.

In chapter 4 we applied the developed model for characterizing the silicon grating surfaces measured by X-ray scattering, which precisely retrieved the substrate profile. such periodic

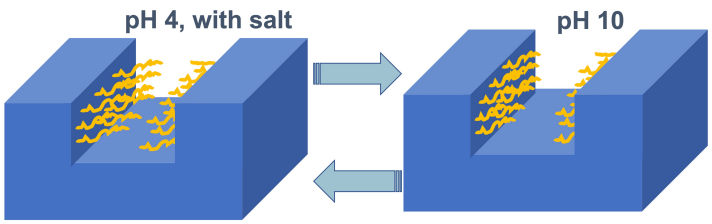

Figure 7.1: Nanofluidic channel with controllable gating property, designed by selective functionalization of channel surfaces by polyelectrolyte bruses.

surfaces are widely applicable across various fields, including optics, electronics, and fluidics. Interestingly, we visualized many physical concepts, mainly the Ewald sphere and Bragg rods, in a scattering experiment representing energy conservation and quantization of momentum. We showed that our approach yields high efficiency and precision in predicting complex profiles by adopting a Parratt thin-slicing formalism. This opens new possibilities in the characterization of nanostructured substrates.

In chapter 5 we applied the model to examine the performance of a series of nanofluidic channels with controllable gating properties. Such nanofluidic channels were designed by selective functionalization of submicron channels etched into a silicon substrate with polyelectrolyte brushes. The development to operate fluid in submicron volume scale requires evaluation by non-destructively probing its function with high resolution in an ultra-small ”close-spaced” system. The suggested characterization method in that chapter provides a non-invasive way to explore the response of the gate to the solution condition with a precision of a few tens of nanometers. Our model yielded simultaneous fit to both specular and off-specular signals and characterized the structural change as a function of pH level and ionic strength, indicating the structural details of chain structures. It mainly shows different regions with different polymer densities, with a denser domain near the wall and a less dense part farther toward the middle of the channels. The fit results indicate collapsed and expanded polymer chain conformations under basic and acidic solution conditions, respectively. These findings show

controlled channel switching between ”open” and ”close” states with pH regulation.

In chapter 6 we applied a qualitative analysis on specular and off-specula neutron reflectometry signals to investigate the effect of membrane curvature on N-BAR protein binding. This experiment used a topographically tunable scaffold by pNIPAM coating on a nanostructured surface. Such a platform induced various shapes on a lipid bilayer deposited on the polymer layer at various temperatures. We also demonstrated that a computational framework utilizing an optimization algorithm could theoretically model reflection patterns based on the DT model and retrieve the profile of the structures that are analogous to the system used in this study.

X-ray and neutron scattering techniques offer a non-invasive method for characterizing nanostructured soft materials. Owing to the rapid advances in scattering capacities such as beam sources, instrumentation, and deuteration facilities, such methods are positioned in a leading role for advanced soft matter-based nanostructures. They can be utilized in a complementary way to access a broader range of the length and time scales. This can benefit the design of advanced polymeric devices such as on-demand drug delivery devices, nano-filters, biosensors, and ionic diodes. Furthermore, considering the fast development in computational resources, the computational models applied for processing scattering signals and interpreting patterns in reciprocal spaces can be efficiently used to characterize detailed profiles.

Bibliography

[1] Takashi Nakanishi. *Supramolecular soft matter: applications in materials and organic electronics*. John Wiley & Sons, 2011.

[2] Quan Li, Albert PHJ Schenning, and Timothy J Bunning. Light-responsive smart soft matter technologies, 2019.

[3] Srikumar Banerjee and A Tyagi. Functional materials: preparation, processing and applications. 2011.

[4] Carmel Majidi. Soft-matter engineering for soft robotics. *Advanced Materials Technologies*, 4(2):1800477, 2019.

[5] Jan Genzer. *Soft matter gradient surfaces: Methods and applications*. John Wiley & Sons, 2012.

[6] Oleg Gang. *Soft Matter And Biomaterials On The Nanoscale: The Wspc Reference On Functional Nanomaterials-Part I (In 4 Volumes)*, volume 20. World Scientific, 2020.

[7] Toshimi Shimizu. *Smart Soft-Matter Nanotubes: Preparation, Functions, and Applications*. Springer Nature, 2021.

[8] Jingjing Ye, Olha Aftenieva, Türkan Bayrak, Archa Jain, Tobias AF König, Artur Erbe, and Ralf Seidel. Complex metal nanostructures with programmable shapes from simple dna building blocks. *Advanced Materials*, 33(29):2100381, 2021.

[9] Dan Li, Qing Zheng, Yanwei Wang, and Hong Chen. Combining surface topography with polymer chemistry: exploring new interfacial biological phenomena. *Polymer chemistry*, 5(1):14–24, 2014.

[10] Adriaan JM Mackus, Marc JM Merkx, and Wilhelmus MM Kessels. From the bottom-up: Toward area-selective atomic layer deposition with high selectivity. *Chemistry of Materials*, 31(1):2–12, 2018.

[11] Ming Fang, Hao Lin, Ho-Yuen Cheung, SenPo Yip, Fei Xiu, Chun-Yuen Wong, and Johnny C Ho. Optical nanoscale patterning through surface-textured polymer films. *Advanced Optical Materials*, 2(9):855–860, 2014.

[12] Andrea R Statz, Robert J Meagher, Annelise E Barron, and Phillip B Messersmith. New peptidomimetic polymers for antifouling surfaces. *Journal of the American Chemical Society*, 127(22):7972–7973, 2005.

[13] Amitabh Bansal, Hoichang Yang, Chunzhao Li, Brian C Benicewicz, Sanat K Kumar, and Linda S Schadler. Controlling the thermomechanical properties of polymer nanocomposites by tailoring the polymer–particle interface. *Journal of Polymer Science Part B: Polymer Physics*, 44(20):2944–2950, 2006.

[14] Ying Li, Timothy M Krentz, Lei Wang, Brian C Benicewicz, and Linda S Schadler. Ligand engineering of polymer nanocomposites: from the simple to the complex. *ACS applied materials & interfaces*, 6(9):6005–6021, 2014.

[15] T. K. Gaylord and M. G. Moharam. Analysis and applications of optical diffraction by gratings. *Proceedings of the IEEE*, 73(5):894–937, 1985.

[16] Sungjun Park, Soo Won Heo, Wonryung Lee, Daishi Inoue, Zhi Jiang, Kilho Yu, Hiroaki Jinno, Daisuke Hashizume, Masaki Sekino, Tomoyuki Yokota, Kenjiro Fukuda, Keisuke Tajima, and Takao Someya. Self-powered ultra-flexible electronics via nano-grating-patterned organic photovoltaics. *Nature*, 561(7724):516—521, September 2018.

[17] Ilaria Rea, Mario Iodice, Giuseppe Coppola, Ivo Rendina, Antigone Marino, and Luca

De Stefano. A porous silicon-based bragg grating waveguide sensor for chemical monitoring. *Sensors and Actuators B: Chemical*, 139(1):39–43, 2009. EUROPT(R)ODE IX Proceedings of the 9th European Conference on Optical Chemical Sensors and Biosensors.

[18] Sergei N Magonov and Darrell H Reneker. Characterization of polymer surfaces with atomic force microscopy. *Annual Review of Materials Science*, 27(1):175–222, 1997.

[19] Greg Haugstad. *Atomic force microscopy: understanding basic modes and advanced applications*. John Wiley & Sons, 2012.

[20] Victor Bellitto. *Atomic force microscopy: imaging, measuring and manipulating surfaces at the atomic scale*. BoD–Books on Demand, 2012.

[21] MK Khan, QY Wang, and Michael E Fitzpatrick. Atomic force microscopy (afm) for materials characterization. In *Materials Characterization Using Nondestructive Evaluation (NDE) Methods*, pages 1–16. Elsevier, 2016.

[22] David C Joy. Scanning electron microscopy for materials characterization. *Current Opinion in Solid State and Materials Science*, 2(4):465–468, 1997.

[23] Rana Ashkar. Selective dynamics in polymeric materials: Insights from quasi-elastic neutron scattering spectroscopy. *Journal of Applied Physics*, 127(15):151101, 2020.

[24] Michael T Hutchings, Philip J Withers, Thomas M Holden, and Torben Lorentzen. *Introduction to the characterization of residual stress by neutron diffraction*. CRC press, 2005.

[25] Gordon Leslie Squires. *Introduction to the theory of thermal neutron scattering*. Courier Corporation, 1996.

[26] Varley F Sears. Neutron scattering lengths and cross sections. *Neutron news*, 3(3):26–37, 1992.

[27] Ingo Hoffmann. Neutrons for the study of dynamics in soft matter systems. *Colloid and Polymer Science*, 292(9):2053–2069, 2014.

[28] Jitendra Bahadur, Leslie F Ruppert, Vitaliy Pipich, Richard Sakurovs, and Yuri B Melnichenko. Porosity of the marcellus shale: A contrast matching small-angle neutron scattering study. *International journal of coal geology*, 188:156–164, 2018.

[29] Rana Ashkar, Hassina Bilheux, Heliosa Bordallo, Robert Briber, David JE Callaway, Xiaolin Cheng, X-Q Chu, Joseph E Curtis, Mark Dadmun, Paul Fenimore, et al. Neutron scattering in the biological sciences: progress and prospects. *Acta Crystallographica Section D: Structural Biology*, 74(12):1129–1168, 2018.

[30] Rana Ashkar, P Stonaha, AL Washington, VR Shah, MR Fitzsimmons, B Maranville, CF Majkrzak, WT Lee, WL Schaich, and Roger Pynn. Dynamical theory calculations of spin-echo resolved grazing-incidence scattering from a diffraction grating. *Journal of Applied Crystallography*, 43(3):455–465, 2010.

[31] Mikhail Zhernenkov, Rana Ashkar, Hao Feng, Olukemi O Akintewe, Nathan D Gallant, Ryan Toomey, John F Ankner, and Roger Pynn. Thermoresponsive pnipam coatings on nanostructured gratings for cell alignment and release. *ACS applied materials & interfaces*, 7(22):11857–11862, 2015.

[32] Nikolaus Hansen, Youhei Akimoto, and Petr Baudis. CMA-ES/pycma on Github. Zenodo, DOI:10.5281/zenodo.2559634, February 2019.

[33] Mitsuhiro Shibayama. Small-angle neutron scattering on polymer gels: phase behavior, inhomogeneities and deformation mechanisms. *Polymer journal*, 43(1):18–34, 2011.

[34] Sow-Hsin Chen. Small angle neutron scattering studies of the structure and interaction in micellar and microemulsion systems. *Annual Review of Physical Chemistry*, 37(1):351–399, 1986.

[35] Colin G Windsor. An introduction to small-angle neutron scattering. *Journal of Applied Crystallography*, 21(6):582–588, 1988.

[36] Xiao-Lin Zhou and Sow-Hsin Chen. Theoretical foundation of x-ray and neutron reflectometry. *Physics Reports*, 257(4-5):223–348, 1995.

[37] Boualem Hammouda. Probing nanoscale structures: the SANS toolbox. *National Institute of Standards and Technology*, pages 1–717, 2008.

[38] M Wolff, A Magerl, and H Zabel. Structure of polymer micelles close to the solid interface. *The European Physical Journal E*, 16(2):141–145, 2005.

[39] L. A. Feigin, D. I. Svergun, and George W. Taylor. Principles of the theory of x-ray and neutron scattering. In *Structure Analysis by Small-Angle X-Ray and Neutron Scattering*, pages 3–24. Springer, 1987.

[40] Abdelhamid Elaissari, Yves Chevalier, Francois Ganachaud, Thierry Delair, and Christian Pichot. Structure of adsorbed and grafted single-stranded dna fragments on aminated latex particles: A small-angle neutron scattering study. *Langmuir*, 16(3):1261–1269, 2000.

[41] C. N. Likos, K. A. Vaynberg, H. Löwen, and N. J. Wagner. Colloidal stabilization by adsorbed gelatin. *Langmuir*, 16(9):4100–4108, 2000.

[42] Irina Estrela-Lopis, Stefano Leporatti, Sergio Moya, Astrid Brandt, Edwin Donath, and Helmut Möhwald. SANS studies of polyelectrolyte multilayers on colloidal templates. *Langmuir*, 18(21):7861–7866, 2002.

[43] Andrea Vaccaro, José Hierrezuelo, Michal Skarba, Paolo Galletto, Jörg Kleimann, and Michal Borkovec. Structure of an adsorbed polyelectrolyte monolayer on oppositely charged colloidal particles. *Langmuir*, 25(9):4864–4867, 2009.

[44] Stephen King, Peter Griffiths, John Hone, and Terence Cosgrove. SANS from adsorbed polymer layers. In *Macromolecular Symposia*, volume 190, pages 33–42. Wiley Online Library, 2002.

[45] Huailiang Li, Kunzhou Wang, Xianguo Tuo, László Almásy, Qiang Tian, Guangai Sun, Mark Julian Henderson, Qintang Li, András Wacha, Jérémie Courtois, et al. Thickness determination of ultrathin poly (acrylic acid) shell on γ-Fe_2O_3 nanocore via small-angle scattering. *Materials Chemistry and Physics*, 204:236–242, 2018.

[46] DL Ho, RM Briber, RL Jones, SK Kumar, and TP Russell. Small-angle neutron scattering studies on thin films of isotopic polystyrene blends. *Macromolecules*, 31(26):9247–9252, 1998.

[47] Ronald L Jones, Sanat K Kumar, Derek L Ho, Robert M Briber, and Thomas P Russell. Chain conformation in ultrathin polymer films. *Nature*, 400(6740):146–149, 1999.

[48] Chloé Chevigny, Didier Gigmes, Denis Bertin, Jacques Jestin, and François Boué. Polystyrene grafting from silica nanoparticles via nitroxide-mediated polymerization (nmp): synthesis and sans analysis with the contrast variation method. *Soft Matter*, 5(19):3741–3753, 2009.

[49] Chloé Chevigny, Jacques Jestin, Didier Gigmes, Ralph Schweins, Emanuela Null Di Cola, Florent Dalmas, Denis Bertin, and François Boué. " Wet-to-Dry" conformational transition of polymer layers grafted to nanoparticles in nanocomposite. *Macromolecules*, 43(11):4833–4837, 2010.

[50] Manfred Stamm. Polymer interfaces on a molecular scale: comparison of techniques and some examples. *Macromolecules: Synthesis, Order and Advanced Properties*, pages 357–400, 1992.

[51] Peter Müller-Buschbaum. Grazing incidence small-angle neutron scattering: Challenges and possibilities. *Polymer journal*, 45(1):34–42, 2013.

[52] A Vorobiev, J Major, H Dosch, P Müller-Buschbaum, P Falus, GP Felcher, and SGE Te Velthuis. Phase and microphase separation of polymer thin films dewetted from silicon a spin–echo resolved grazing incidence neutron scattering study. *The Journal of Physical Chemistry B*, 115(19):5754–5765, 2011.

[53] János Major, Alexei Vorobiev, Adrian Rühm, Ralf Maier, Márton Major, Markus Mezger, Max Nülle, Helmut Dosch, Gian P Felcher, Péter Falus, et al. A spin-echo resolved grazing incidence scattering setup for the neutron interrogation of buried nanostructures. *Review of Scientific Instruments*, 80(12):123903, 2009.

[54] Michael S Jablin, Mikhail Zhernenkov, Boris P Toperverg, Manish Dubey, Hillary L Smith, Ajay Vidyasagar, Ryan Toomey, Alan J Hurd, and Jaroslaw Majewski. In-plane correlations in a polymer-supported lipid membrane measured by off-specular neutron scattering. *Physical review letters*, 106(13):138101, 2011.

[55] R. Ashkar, R. M. Dalgliesh, R. Pynn, A. D. F. Dunbar, R. A. L. Jones, and A. J. Parnell. Profile retrieval of a buried periodic structure using spin echo grazing incidence neutron scattering. *Applied Physics Letters*, 116(10):101602, 2020.

[56] Lyman G Parratt. Surface studies of solids by total reflection of x-rays. *Physical review*, 95(2):359, 1954.

[57] Andrew Nelson. Co-refinement of multiple-contrast neutron/X-ray reflectivity data using *MOTOFIT*. *Journal of Applied Crystallography*, 39(2):273–276, 2006.

[58] J. R. Levine, J. B. Cohen, Y. W. Chung, and P. Georgopoulos. Grazing-incidence small-angle x-ray scattering: new tool for studying thin film growth. *Journal of Applied Crystallography*, 22(6):528–532, 1989.

[59] P Müller-Buschbaum, E Metwalli, J-F Moulin, V Kudryashov, M Haese-Seiller, and R Kampmann. Time of flight grazing incidence small angle neutron scattering. *The European Physical Journal Special Topics*, 167(1):107–112, 2009.

[60] P Müller-Buschbaum, Leander Schulz, E Metwalli, J-F Moulin, and R Cubitt. Lateral structures of buried interfaces in aba-type triblock copolymer films. *Langmuir*, 24(15):7639–7644, 2008.

[61] D Freitas Siqueira, DW Schubert, V Erb, Manfred Stamm, and JP Amato. Interface thickness of the incompatible polymer system PS/PnBMA as measured by neutron reflectometry and ellipsometry. *Colloid and Polymer Science*, 273(11):1041–1048, 1995.

[62] Mathias Lösche, Johannes Schmitt, Gero Decher, Wim G Bouwman, and Kristian Kjaer. Detailed structure of molecularly thin polyelectrolyte multilayer films on solid substrates as revealed by neutron reflectometry. *Macromolecules*, 31(25):8893–8906, 1998.

[63] Mihaela Delcea and Christiane A Helm. X-ray and neutron reflectometry of thin films at liquid interfaces. *Langmuir*, 35(26):8519–8530, 2019.

[64] T Kanaya, T Miyazaki, H Watanabe, K Nishida, H Yamano, S Tasaki, and DB Bucknall. Annealing effects on thickness of polystyrene thin films as studied by neutron reflectivity. *Polymer*, 44(14):3769–3773, 2003.

[65] Hiroyuki Aoki, Hiroki Ogawa, and Mikihito Takenaka. Neutron reflectometry tomography for imaging and depth structure analysis of thin films with in-plane inhomogeneity. *Langmuir*, 37(1):196–203, 2020.

[66] Naoya Torikai, Ichiro Noda, Alamgir Karim, Sushil K Satija, Charles C Han, Yushu Matsushita, and Toshihiro Kawakatsu. Neutron reflection studies on segment distribution of block chains in lamellar microphase-separated structures. *Macromolecules*, 30(10):2907–2914, 1997.

[67] WE Wallace, NC Beck Tan, WL Wu, and S Satija. Mass density of polystyrene thin films measured by twin neutron reflectivity. *The Journal of Chemical Physics*, 108(9):3798–3804, 1998.

[68] MK Sanyal, JK Basu, A Datta, and S Banerjee. Determination of small fluctuations in electron density profiles of thin films: Layer formation in a polystyrene film. *EPL (Europhysics Letters)*, 36(4):265, 1996.

[69] A Beena Unni, G Vignaud, JP Chapel, J Giermanska, JK Bal, N Delorme, T Beuvier, S Thomas, Y Grohens, and A Gibaud. Probing the density variation of confined polymer thin films via simple model-independent nanoparticle adsorption. *Macromolecules*, 50(3):1027–1036, 2017.

[70] Stuart B Kirschner, Nathaniel P Smith, Kevin A Wepasnick, Howard E Katz, Brian J Kirby, Julie A Borchers, and Daniel H Reich. X-ray and neutron reflectivity and electronic properties of pcbm-poly (bromo) styrene blends and bilayers with poly (3-hexylthiophene). *Journal of Materials Chemistry*, 22(10):4364–4370, 2012.

[71] Rita J El-Khouri, Daniel A Bricarello, Erik B Watkins, Caroline Y Kim, Chad E Miller, Timothy E Patten, Atul N Parikh, and Tonya L Kuhl. ph responsive polymer cushions for probing membrane environment interactions. *Nano letters*, 11(5):2169–2172, 2011.

[72] Bruno Dorner. *Coherent inelastic neutron scattering in lattice dynamics*, volume 93. Springer, 2006.

[73] Marc Bée. Quasielastic neutron scattering. 1988.

[74] Juan Colmenero and Arantxa Arbe. Recent progress on polymer dynamics by neutron scattering: From simple polymers to complex materials. *Journal of Polymer Science Part B: Polymer Physics*, 51(2):87–113, 2013.

[75] Barbara J Gabrys and Toshiji Kanaya. Basic modes of motion in polymers. In *Dynamics of Soft Matter*, pages 59–101. Springer, 2012.

[76] Mark R Johnson, Miguel A González, Mohamed Zbiri, and Eric Pellegrini. Computational tools to understand inelastic and quasielastic neutron scattering data. In *Dynamics of Soft Matter*, pages 25–56. Springer, 2012.

[77] Arantxa Arbe, Fernando Alvarez, and Juan Colmenero. Neutron scattering and molecular dynamics simulations: Synergetic tools to unravel structure and dynamics in polymers. *Soft Matter*, 8(32):8257–8270, 2012.

[78] Alexei P Sokolov and Victoria García Sakai. Experimental techniques for studies of dynamics in soft materials. In *Dynamics of Soft Matter*, pages 1–23. Springer, 2012.

[79] T Miyazaki, K Nishida, and T Kanaya. Contraction and reexpansion of polymer thin films. *Physical Review E*, 69(2):022801, 2004.

[80] Christopher L Soles, Jack F Douglas, and Wen-Li Wu. Dynamics of thin polymer films: Recent insights from incoherent neutron scattering. *Journal of Polymer Science Part B: Polymer Physics*, 42(17):3218–3234, 2004.

[81] Joseph L Keddie, Richard AL Jones, and Rachel A Cory. Size-dependent depression of the glass transition temperature in polymer films. *EPL (Europhysics Letters)*, 27(1):59, 1994.

[82] Rintaro Inoue, Toshiji Kanaya, Koji Nishida, Itaru Tsukushi, and Kaoru Shibata. Inelastic neutron scattering study of low energy excitations in polymer thin films. *Physical review letters*, 95(5):056102, 2005.

[83] Andreas Schönhals, Reiner Zorn, and Bernhard Frick. Inelastic neutron spectroscopy as a tool to investigate nanoconfined polymer systems. *Polymer*, 105:393–406, 2016.

[84] Ryan Poling-Skutvik, Katy N Olafson, Suresh Narayanan, Laura Stingaciu, Antonio Faraone, Jacinta C Conrad, and Ramanan Krishnamoorti. Confined dynamics of grafted polymer chains in solutions of linear polymer. *Macromolecules*, 50(18):7372–7379, 2017.

[85] John M Carpenter and C-K Loong. *Elements of slow-neutron scattering*. Cambridge University Press, 2015.

[86] Charles J Glinka. Methods of X-ray and neutron scattering in polymer science, by Ryong-Joon Roe. *Physics Today*, 54(3):60–61, 2001.

[87] Roger Pynn. Neutron scattering: a primer. *Los Alamos Science*, 19:1–31, 1990.

[88] Roger Pynn. Neutron scattering by rough surfaces at grazing incidence. *Physical Review B*, 45(2):602, 1992.

[89] L Nevot and P Croce. Caractérisation des surfaces par réflexion rasante de rayons X. application à l'étude du polissage de quelques verres silicates. *Revue de Physique appliquée*, 15(3):761–779, 1980.

[90] SK Sinha, EB Sirota, Garoff, S, and HB Stanley. X-ray and neutron scattering from rough surfaces. *Physical Review B*, 38(4):2297, 1988.

[91] Rana Ashkar, V. O. de Haan, A. A. van Well, R. Dalgliesh, J. Plomp, M. R. Fitzsimmons, W. L. Schaich, and Roger Pynn. Comparison of dynamical theory and phase-object approximation for neutron scattering from periodic structures. *Journal of Applied Crystallography*, 44(5):958–965, Oct 2011.

[92] John Brian Pendry. *Low energy electron diffraction: the theory and its application to determination of surface structure*. Number 2. Academic Press, 1974.

[93] Mary ONeill and Stephen M. Kelly. Ordered materials for organic electronics and photonics. *Advanced Materials*, 23(5):566–584, 2011.

[94] J Vörös, JJ Ramsden, G Csucs, I Szendrő, SM De Paul, M Textor, and ND Spencer. Optical grating coupler biosensors. *Biomaterials*, 23(17):3699–3710, 2002.

[95] Yong-Qiang Liu, Ling-Bao Kong, Chao-Hai Du, and Pu-Kun Liu. A terahertz electronic source based on the spoof surface plasmon with subwavelength metallic grating. *IEEE Transactions on Plasma Science*, 44(6):930–937, 2016.

[96] Joseph R Lakowicz. Radiative decay engineering 3. surface plasmon-coupled directional emission. *Analytical Biochemistry*, 324(2):153–169, 2004.

[97] Matthew P. DeLisa, Zheng Zhang, Mira Shiloach, Saeed Pilevar, Christopher C. Davis, James S. Sirkis, and William E. Bentley. Evanescent wave long-period fiber bragg grating as an immobilized antibody biosensor. *Analytical Chemistry*, 72(13):2895–2900, 2000. PMID: 10905324.

[98] Claus Heine and Rudolf H. Morf. Submicrometer gratings for solar energy applications. *Appl. Opt.*, 34(14):2476–2482, May 1995.

[99] Johannes Eisenlohr, Nico Tucher, Hubert Hauser, Martin Graf, Jan Benick, Benedikt Bläsi, Jan Christoph Goldschmidt, and Martin Hermle. Efficiency increase of crystalline silicon solar cells with nanoimprinted rear side gratings for enhanced light trapping. *Solar Energy Materials and Solar Cells*, 155:288–293, 2016.

[100] T. Søndergaard and Sergey I. Bozhevolnyi. Surface-plasmon polariton resonances in triangular-groove metal gratings. *Physical Review B*, 80:195407, 2009.

[101] Takashi Sukegawa, Shigeru Sugiyama, Tsuyoshi Kitamura, Yukinobu Okura, and Masatsugu Koyama. High-performance astronomical gratings by Canon. In Ramón Navarro, Colin R. Cunningham, and Eric Prieto, editors, *Modern Technologies in Space- and Ground-based Telescopes and Instrumentation II*, volume 8450, pages 952 – 963. International Society for Optics and Photonics, SPIE, 2012.

[102] J Vörös, J.J Ramsden, G Csúcs, I Szendrő, S.M De Paul, M Textor, and N.D Spencer. Optical grating coupler biosensors. *Biomaterials*, 23(17):3699–3710, 2002.

[103] Burak Turker, Hasan Guner, Sencer Ayas, Okan O Ekiz, Handan Acar, Mustafa O Guler, and Aykutlu Dâna. Grating coupler integrated photodiodes for plasmon resonance based sensing. *Lab on a chip*, 11(2):282—287, 2011.

[104] Minhao Yan and Alain Gibaud. On the intersection of grating truncation rods with the Ewald sphere studied by grazing-incidence small-angle X-ray scattering. *Journal of Applied Crystallography*, 40(6):1050–1055, 2007.

[105] T. Hofmann, E. Dobisz, and B. M. Ocko. Grazing incident small angle x-ray scattering: A metrology to probe nanopatterned surfaces. *Journal of Vacuum Science & Technology B: Microelectronics and Nanometer Structures Processing, Measurement, and Phenomena*, 27(6):3238–3243, 2009.

[106] Jan Wernecke, Frank Scholze, and Michael Krumrey. Direct structural characterisation of line gratings with grazing incidence small-angle x-ray scattering. *Review of Scientific Instruments*, 83(10):103906, 2012.

[107] Hao Feng, Rana Ashkar, Nina Steinke, Robert Dalgliesh, Nickolay V Lavrik, Ivan I Kravchenko, and Roger Pynn. Grating-based holographic diffraction methods for x-rays and neutrons: phase object approximation and dynamical theory. *Journal of Applied Crystallography*, 51(1):68–75, 2018.

[108] Hyo Seon Suh, Xuanxuan Chen, Paulina A. Rincon-Delgadillo, Zhang Jiang, Joseph Strzalka, Jin Wang, Wei Chen, Roel Gronheid, Juan J. de Pablo, Nicola Ferrier, Manolis Doxastakis, and Paul F. Nealey. Characterization of the shape and line-edge roughness of polymer gratings with grazing incidence small-angle X-ray scattering and atomic force microscopy. *Journal of Applied Crystallography*, 49(3):823–834, Jun 2016.

[109] DECTRIS ALBULA: Software for X-ray and electron detectors. https://www.dectris.com/detectors/albula-software/.

[110] M. Napoli, J. C. T. Eijkel, and S. Pennathur. Nanofluidic technology for biomolecule applications: a critical review. *Lab on a Chip*, 10:957–985, 2010.

[111] Piyush M Sinha, George Valco, Sadhana Sharma, Xuewu Liu, and Mauro Ferrari. Nanoengineered device for drug delivery application. *Nanotechnology*, 15(10):S585–S589, 2004.

[112] Annamaria Mocciaro, Theodore L. Roth, Hayley M. Bennett, Magali Soumillon, Abhik Shah, Joseph Hiatt, Kevin Chapman, Alexander Marson, and Gregory Lavieu. Light-activated cell identification and sorting (lacis) for selection of edited clones on a nanofluidic device. *Communications Biology*, 1(1):41, May 2018.

[113] Jonas O. Tegenfeldt, Christelle Prinz, Han Cao, Richard L. Huang, Robert H. Austin, Stephen Y. Chou, Edward C. Cox, and James C. Sturm. Micro- and nanofluidics for dna analysis. *Analytical and Bioanalytical Chemistry*, 378(7):1678–1692, Apr 2004.

[114] Yanxiao Feng, Yuechuan Zhang, Cuifeng Ying, Deqiang Wang, and Chunlei Du. Nanopore-based fourth-generation dna sequencing technology. *Genomics, Proteomics Bioinformatics*, 13(1):4–16, 2015.

[115] Andrew H. Laszlo, Ian M. Derrington, Brian C. Ross, Henry Brinkerhoff, Andrew Adey, Ian C. Nova, Jonathan M. Craig, Kyle W. Langford, Jenny Mae Samson, Riza Daza, Kenji Doering, Jay Shendure, and Jens H. Gundlach. Decoding long nanopore sequencing reads of natural dna. *Nature Biotechnology*, 32(8):829–833, Aug 2014.

[116] Rodolphe Marie, Jonas N. Pedersen, David L. V. Bauer, Kristian H. Rasmussen, Mohammed Yusuf, Emanuela Volpi, Henrik Flyvbjerg, Anders Kristensen, and Kalim U. Mir. Integrated view of genome structure and sequence of a single dna molecule in a nanofluidic device. *Proceedings of the National Academy of Sciences*, 110(13):4893–4898, 2013.

[117] Shaurya Prakash, Aigars Piruska, Enid N. Gatimu, Paul W. Bohn, Jonathan V. Sweedler, and Mark A. Shannon. Nanofluidics: Systems and applications. *IEEE Sensors Journal*, 8(5):441–450, 2008.

[118] P. Abgrall and N.T. Nguyen. *Nanofluidics*. Artech House, 2009.

[119] Rohit Karnik, Rong Fan, Min Yue, Deyu Li, Peidong Yang, and Arun Majumdar. Electrostatic control of ions and molecules in nanofluidic transistors. *Nano Letters*, 5(5):943–948, 2005. PMID: 15884899.

[120] Ning Hu, Ye Ai, and Shizhi Qian. Field effect control of electrokinetic transport in micro/nanofluidics. *Sensors and Actuators B: Chemical*, 161(1):1150–1167, 2012.

[121] Shaurya Prakash and A. T. Conlisk. Field effect nanofluidics. *Lab on a Chip*, 16:3855–3865, 2016.

[122] Hui Ouyang, Zhenhai Xia, and Jiang Zhe. Voltage-controlled flow regulating in nanofluidic channels with charged polymer brushes. *Microfluidics and Nanofluidics*, 9(4):915–922, Oct 2010.

[123] Jianhua Huang, Yongmei Wang, and Mohamed Laradji. Flow control by smart nanofluidic channels: a dissipative particle dynamics simulation. *Macromolecules*, 39(16):5546–5554, 2006.

[124] Shashishekar P. Adiga and Donald W. Brenner. Stimuli-responsive polymer brushes for flow control through nanopores. *Journal of Functional Biomaterials*, 3(2):239–256, 2012.

[125] Tong Shu, Liang Hu, Qiming Shen, Li Jiang, Qiang Zhang, and Michael J. Serpe. Stimuli-responsive polymer-based systems for diagnostic applications. *Journal of Materials Chemistry B*, 8:7042–7061, 2020.

[126] Mustafa S Yavuz, Yiyun Cheng, Jingyi Chen, Claire M Cobley, Qiang Zhang, Matthew Rycenga, Jingwei Xie, Chulhong Kim, Kwang H Song, Andrea G Schwartz, et al. Gold nanocages covered by smart polymers for controlled release with near-infrared light. *Nature materials*, 8(12):935–939, 2009.

[127] O. Azzaroni, S. E. Moya, A. A. Brown, Z. Zheng, E. Donath, and W. T. S. Huck. Polyelectrolyte brushes as ink nanoreservoirs for microcontact printing of ionic species

with poly(dimethyl siloxane) stamps. *Advanced Functional Materials*, 16(8):1037–1042, 2006.

[128] Basit Yameen, Mubarak Ali, Reinhard Neumann, Wolfgang Ensinger, Wolfgang Knoll, and Omar Azzaroni. Proton -regulated rectified ionic transport through solid-state conical nanopores modified with phosphate-bearing polymer brushes. *Chemical Communications Journal*, 46:1908–1910, 2010.

[129] Nehal I. Abu-Lail, Marian Kaholek, Bruce LaMattina, Robert L. Clark, and Stefan Zauscher. Micro-cantilevers with end-grafted stimulus-responsive polymer brushes for actuation and sensing. *Sensors and Actuators B: Chemical*, 114(1):371–378, 2006.

[130] Johanna Bünsow, Tim S. Kelby, and Wilhelm T. S. Huck. Polymer brushes: Routes toward mechanosensitive surfaces. *Accounts of Chemical Research*, 43(3):466–474, 2010.

[131] Menglian Wei, Yongfeng Gao, Xue Li, and Michael J. Serpe. Stimuli-responsive polymers and their applications. *Polym. Chem.*, 8:127–143, 2017.

[132] Hugo Almeida, Maria Amaral, and Paulo Lobão. Temperature and ph stimuli-responsive polymers and their applications in controlled and selfregulated drug delivery. *Journal of Applied Pharmaceutical Science*, 2:1–10, 07 2012.

[133] Dirk Schmaljohann. Thermo- and ph-responsive polymers in drug delivery. *Advanced Drug Delivery Reviews*, 58(15):1655–1670, 2006. 2006 Supplementary Non-Thematic Collection.

[134] J. F. Mano. Stimuli-responsive polymeric systems for biomedical applications. *Advanced Engineering Materials*, 10(6):515–527, 2008.

[135] Mónica Cristina García. Ionic strength responsive polymers for drug delivery applications. pages 393–409, 2019.

[136] Takashi Miyata, Noriko Asami, and Tadashi Uragami. A reversibly antigen-responsive hydrogel. *Nature*, 399(6738):766–769, 1999.

[137] Nikhil Sood, Ankur Bhardwaj, Shuchi Mehta, and Abhinav Mehta. Stimuli-responsive hydrogels in drug delivery and tissue engineering. *Drug Delivery*, 23(3):748–770, 2016.

[138] Sebastian Rauch, Petra Uhlmann, and Klaus-Jochen Eichhorn. In situ spectroscopic ellipsometry of ph-responsive polymer brushes on gold substrates. *Analytical and Bioanalytical Chemistry*, 405(28):9061–9069, 2013.

[139] Petra van de Wetering, Ed E. Moret, Nancy M. E. Schuurmans-Nieuwenbroek, Mies J. van Steenbergen, and Wim E. Hennink. Structure—activity relationships of water-soluble cationic methacrylate/methacrylamide polymers for nonviral gene delivery. *Bioconjugate Chemistry*, 10(4):589–597, 1999.

[140] Arjen M. Funhoff, Cornelus F. van Nostrum, Gerben A. Koning, Nancy M. E. Schuurmans-Nieuwenbroek, Daan J. A. Crommelin, and Wim E. Hennink. Endosomal escape of polymeric gene delivery complexes is not always enhanced by polymers buffering at low ph. *Biomacromolecules*, 5(1):32–39, 2004.

[141] Caleb E. Gallops, Chang Yu, Jesse D. Ziebarth, and Yongmei Wang. Effect of the protonation level and ionic strength on the structure of linear polyethyleneimine. *ACS Omega*, 4(4):7255–7264, 2019.

[142] S. Sanjuan, P. Perrin, N. Pantoustier, and Y. Tran. Synthesis and swelling behavior of ph-responsive polybase brushes. *Langmuir*, 23(10):5769–5778, 2007.

[143] Ihor Tokarev, Iryna Tokareva, and Sergiy Minko. Optical nanosensor platform operating in near-physiological ph range via polymer-brush-mediated plasmon coupling. *ACS Applied Materials & Interfaces*, 3(2):143–146, 2011.

[144] Rana Ashkar. *Dynamical theory applications to neutron scattering from periodic nanostructures*. PhD thesis, Indiana University, 2012.

[145] Haidong Jia, Andrew Wildes, and Simon Titmuss. Structure of ph-responsive polymer brushes grown at the gold–water interface: Dependence on grafting density and temperature. *Macromolecules*, 45(1):305–312, 2012.

[146] Mark Geoghegan, Lorena Ruiz-Pérez, Cheen C. Dang, Andrew J. Parnell, Simon J. Martin, Jonathan R. Howse, Richard A. L. Jones, Ramin Golestanian, Paul D. Topham, Colin J. Crook, Anthony J. Ryan, Devinderjit S. Sivia, John R. P. Webster, and Alain Menelle. The ph-induced swelling and collapse of a polybase brush synthesized by atom transfer radical polymerization. *Soft Matter*, 2:1076–1080, 2006.

[147] Y. Tran, P. Auroy, and L-T. Lee. Determination of the structure of polyelectrolyte brushes. *Macromolecules*, 32(26):8952–8964, 1999.

[148] Mauro Moglianetti, John R. P. Webster, Steve Edmondson, Steven P. Armes, and Simon Titmuss. Neutron reflectivity study of the structure of ph-responsive polymer brushes grown from a macroinitiator at the sapphire−water interface. *Langmuir*, 26(15):12684–12689, 2010. PMID: 20583764.

[149] Rana Ashkar, W. L. Schaich, V. O. de Haan, A. A. van Well, R. Dalgliesh, J. Plomp, and Roger Pynn. Dynamical theory: Application to spin-echo resolved grazing incidence scattering from periodic structures. *Journal of Applied Physics*, 110(10):102201, 2011.

[150] Rana Ashkar, V. O. de Haan, A. A. van Well, R. Dalgliesh, J. Plomp, M. R. Fitzsimmons, W. L. Schaich, and Roger Pynn. Comparison of dynamical theory and phase-object approximation for neutron scattering from periodic structures. *Journal of Applied Crystallography*, 44(5):958–965, Oct 2011.

[151] D. S. Sivia, W. A. Hamilton, G. S. Smith, T. P. Rieker, and R. Pynn. A novel experimental procedure for removing ambiguity from the interpretation of neutron and x-ray reflectivity measurements: ‘‘speckle holography’’. *Journal of Applied Physics*, 70(2):732–738, 1991.

[152] E. Zhulina, O. Borisov, and T. Birshtein. Structure of grafted polyelectrolyte layer. *Journal de Physique II*, 2(1):63–74, 1992.

[153] Andrey V. Dobrynin, Michael Rubinstein, and Sergei P. Obukhov. Cascade of transitions of polyelectrolytes in poor solvents. *Macromolecules*, 29(8):2974–2979, 1996.

[154] S. T. Milner. Polymer brushes. *Science*, 251(4996):905–914, 1991.

[155] Alexander, S. Adsorption of chain molecules with a polar head a scaling description. *J. Phys. France*, 38(8):983–987, 1977.

[156] P. G. de Gennes. Conformations of polymers attached to an interface. *Macromolecules*, 13(5):1069–1075, 1980.

[157] M. Biesalski, D. Johannsmann, and J. Rühe. Synthesis and swelling behavior of a weak polyacid brush. *The Journal of Chemical Physics*, 117(10):4988–4994, 2002.

[158] Jian Zhang, Ran Kou, and Guangming Liu. Effect of salt concentration on the ph responses of strong and weak polyelectrolyte brushes. *Langmuir*, 33(27):6838–6845, 2017. PMID: 28628336.

[159] Jürgen Rühe, Matthias Ballauff, Markus Biesalski, Peter Dziezok, Franziska Gröhn, Diethelm Johannsmann, Nikolay Houbenov, Norbert Hugenberg, Rupert Konradi, Sergiy Minko, Michail Motornov, Roland R. Netz, Manfred Schmidt, Christian Seidel, Manfred Stamm, Tim Stephan, Denys Usov, and Haining Zhang. *Polyelectrolyte Brushes*, pages 79–150. Springer Berlin Heidelberg, Berlin, Heidelberg, 2004.

[160] Xiaolong Wang, Hong Hu, Youde Shen, Xuechang Zhou, and Zijian Zheng. Stretchable conductors with ultrahigh tensile strain and stable metallic conductance enabled by prestrained polyelectrolyte nanoplatforms. *Advanced Materials*, 23(27):3090–3094, 2011.

[161] Joshua D. Willott, Timothy J. Murdoch, Ben A. Humphreys, Steve Edmondson, Grant B. Webber, and Erica J. Wanless. Critical salt effects in the swelling behavior of a weak polybasic brush. *Langmuir*, 30(7):1827–1836, 2014.

[162] Kevin N. Witte, Sangtae Kim, and You-Yeon Won. Self-consistent field theory study of the effect of grafting density on the height of a weak polyelectrolyte brush. *The Journal of Physical Chemistry B*, 113(32):11076–11084, 2009.

[163] R. Israels, F. A. M. Leermakers, and G. J. Fleer. On the theory of grafted weak polyacids. *Macromolecules*, 27(11):3087–3093, 1994.

[164] Markus Biesalski, Jürgen Rühe, and Diethelm Johannsmann. Segment density profiles of polyelectrolyte brushes determined by fourier transform ellipsometry. *The Journal of Chemical Physics*, 111(15):7029–7037, 1999.

[165] Peng Gong, Jan Genzer, and I. Szleifer. Phase behavior and charge regulation of weak polyelectrolyte grafted layers. *Phys. Rev. Lett.*, 98:018302, 2007.

[166] Yu. V. Lyatskaya, F. A. M. Leermakers, G. J. Fleer, E. B. Zhulina, and T. M. Birshtein. Analytical self-consistent-field model of weak polyacid brushes. *Macromolecules*, 28(10):3562–3569, 1995.

[167] E. B. Zhulina, T. M. Birshtein, and O. V. Borisov. Theory of ionizable polymer brushes. *Macromolecules*, 28(5):1491–1499, 1995.

[168] G. J. Fleer. Polyelectrolyte brushes and polyelectrolyte adsorption layers. *Berichte der Bunsengesellschaft für physikalische Chemie*, 100(6):936–942, 1996.

[169] Tao Wu, Peng Gong, Igal Szleifer, Petr Vlček, Vladimír Šubr, and Jan Genzer. Behavior of surface-anchored poly(acrylic acid) brushes with grafting density gradients on solid substrates: 1. experiment. *Macromolecules*, 40(24):8756–8764, 2007.

[170] E. P. K. Currie, A. B. Sieval, G. J. Fleer, and M. A. Cohen Stuart. Polyacrylic acid brushes: surface pressure and salt-induced swelling. *Langmuir*, 16(22):8324–8333, 2000.

[171] Haining Zhang and Jürgen Rühe. Swelling of poly(methacrylic acid) brushes: influence of monovalent salts in the environment. *Macromolecules*, 38(11):4855–4860, 2005.

[172] Klaus D. Sattler. 21st century nanoscience – a handbook. exotic nanostructures and quantum systems. (volume five), 2020.

[173] Wonhwa Cho and Robert V Stahelin. Membrane-protein interactions in cell signaling and membrane trafficking. *Annual Review of Biophysics and Biomolecular Structure*, 34:119–151, 2005.

[174] Sandra Tan, Hwee Tong Tan, and Maxey CM Chung. Membrane proteins and membrane proteomics. *Proteomics*, 8(19):3924–3932, 2008.

[175] Hadi Rahmaninejad, Tom Pace, Byeong Jae Chun, and Peter M. Kekenes-Huskey. Crowding within synaptic junctions influences the degradation of nucleotides by cd39 and cd73 ectonucleotidases. *Biophysical Journal*, 121(2):309–318, 2022.

[176] Eric J Bernhard, W Gillies McKenna, Andrew D Hamilton, Said M Sebti, Yimin Qian, Junmin Wu, and Ruth J Muschel. Inhibiting ras prenylation increases the

radiosensitivity of human tumor cell lines with activating mutations of ras oncogenes. *Cancer research*, 58(8):1754–1761, 1998.

[177] Paul Carter, Leia Smith, and Maureen Ryan. Identification and validation of cell surface antigens for antibody targeting in oncology. *Endocrine-related cancer*, 11(4):659–687, 2004.

[178] Bruce Alberts. *Molecular biology of the cell*. WW Norton & Company, 2017.

[179] Margaret C Frame. Src in cancer: deregulation and consequences for cell behaviour. *Biochimica et Biophysica Acta (BBA)-Reviews on Cancer*, 1602(2):114–130, 2002.

[180] Stefano Vanni, Hisaaki Hirose, Hélène Barelli, Bruno Antonny, and Romain Gautier. A sub-nanometre view of how membrane curvature and composition modulate lipid packing and protein recruitment. *Nature communications*, 5(1):1–10, 2014.

[181] Joost Holthuis and Tim P Levine. Lipid traffic: floppy drives and a superhighway. *Nature Reviews Molecular Cell Biology*, 6(3):209–220, 2005.

[182] Joëlle Bigay and Bruno Antonny. Curvature, lipid packing, and electrostatics of membrane organelles: defining cellular territories in determining specificity. *Developmental cell*, 23(5):886–895, 2012.

[183] Reinhard Lipowsky. The conformation of membranes. *Nature*, 349(6309):475–481, 1991.

[184] Iris K Jarsch, Frederic Daste, and Jennifer L Gallop. Membrane curvature in cell biology: An integration of molecular mechanisms. *Journal of Cell Biology*, 214(4):375–387, 2016.

[185] Kerwyn Casey Huang, Ranjan Mukhopadhyay, and Ned S Wingreen. A curvature-mediated mechanism for localization of lipids to bacterial poles. *PLoS Computational Biology*, 2(11):e151, 2006.

[186] Jiajia Bi, Ruifei Wang, and Xianlu Zeng. Lipid rafts regulate the lamellipodia formation of melanoma a375 cells via actin cytoskeleton-mediated recruitment of $\beta 1$ and $\beta 3$ integrin. *Oncology Letters*, 16(5):6540–6546, 2018.

[187] Lorenzo Migliorini, Tommaso Santaniello, Yunsong Yan, Cristina Lenardi, and Paolo Milani. Low-voltage electrically driven homeostatic hydrogel-based actuators for underwater soft robotics. *Sensors and Actuators B: Chemical*, 228:758–766, 2016.

[188] NN Ferreira, LMB Ferreira, VMO Cardoso, FI Boni, ALR Souza, and MPD Gremião. Recent advances in smart hydrogels for biomedical applications: From self-assembly to functional approaches. *European Polymer Journal*, 99:117–133, 2018.

[189] Sakineh Hajebi, Navid Rabiee, Mojtaba Bagherzadeh, Sepideh Ahmadi, Mohammad Rabiee, Hossein Roghani-Mamaqani, Mohammadreza Tahriri, Lobat Tayebi, and Michael R Hamblin. Stimulus-responsive polymeric nanogels as smart drug delivery systems. *Acta biomaterialia*, 92:1–18, 2019.

[190] Virginia Capella, Rebeca E Rivero, Ana C Liaudat, Luis E Ibarra, Dardo A Roma, Fabrisio Alustiza, Fernando Manas, Cesar A Barbero, Pablo Bosch, Claudia R Rivarola, et al. Cytotoxicity and bioadhesive properties of poly-n-isopropylacrylamide hydrogel. *Heliyon*, 5(4):e01474, 2019.

[191] Mijo Simunovic, Gregory A Voth, Andrew Callan-Jones, and Patricia Bassereau. When physics takes over: Bar proteins and membrane curvature. *Trends in Cell Biology*, 25(12):780–792, 2015.

[192] Chi Chen. Topographically and mechanically tunable pnipam scaffolds. Master's thesis, Virginia Tech, 2022.

[193] Aljoša Hafner, Philipp Gutfreund, Boris P Toperverg, Andrew OF Jones, Johann P de Silva, Andrew Wildes, Henry E Fischer, Mark Geoghegan, and Michele Sferrazza. Combined specular and off-specular reflectometry: elucidating the complex structure of soft buried interfaces. *Journal of Applied Crystallography*, 54(3):924–948, 2021.

[194] Harvey T McMahon and Jennifer L Gallop. Membrane curvature and mechanisms of dynamic cell membrane remodelling. *Nature*, 438(7068):590–596, 2005.

[195] Ottavio Cremona, Gilbert Di Paolo, Markus R Wenk, Anita Lüthi, Warren T Kim, Kohji Takei, Laurie Daniell, Yasuo Nemoto, Stephen B Shears, Richard A Flavell, et al. Essential role of phosphoinositide metabolism in synaptic vesicle recycling. *Cell*, 99(2):179–188, 1999.

[196] Jez Carlton, Miriam Bujny, Brian J Peter, Viola MJ Oorschot, Anna Rutherford, Harry Mellor, Judith Klumperman, Harvey T McMahon, and Peter J Cullen. Sorting nexin-1 mediates tubular endosome-to-tgn transport through coincidence sensing of high-curvature membranes and 3-phosphoinositides. *Current Biology*, 14(20):1791–1800, 2004.

[197] Brian J Peter, Helen M Kent, Ian G Mills, Yvonne Vallis, P Jonathan G Butler, Philip R Evans, and Harvey T McMahon. Bar domains as sensors of membrane curvature: the amphiphysin bar structure. *Science*, 303(5657):495–499, 2004.